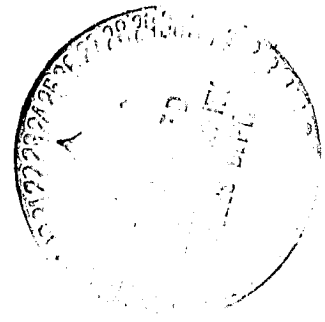

LOCKHEED

MISSILES & SPACE COMPANY, INC. • SUNNYVALE, CALIFORNIA

Final Report

Contract NAS8-33195

Analysis of X-Ray and EUV Spectra of Solar Active Regions

Keith T. Strong
Loren W. Acton

Lockheed Palo Alto Research Laboratory
3251 Hanover Street
Palo Alto, California 94304

Contents

Introduction

This final report summarises the results of the analysis of data acquired by two flights of an array of six Bragg crystal spectrometers. The objective of the experiments were to obtain high spatial and spectral resolution observations of various coronal features at soft X-ray wavelengths (9-23Å).

The first rocket, NASA-Aerobee 26.002, was launched on 11 June, 1973, at 18:30 U.T. It observed two active regions and an area of quiet corona. Both active regions, McMath 12379 and McMath 12387, were quiescent at the time of observation. The region of quiet corona was near the center of the visible disk. The second flight, NASA-Aerobee 26.003, was launched on 19 December, 1973, at 22:07 U.T. This observed a single active region, McMath 12664. This region was fairly active prior to the flight.

Each spectrometer system consisted of a two-dimensional collimator with a field of view of approximately 35 arc seconds full width half maximum (FWHM). Two of the instruments had larger fields of view of 150 arc seconds. The diffraction crystals were KAP, and were mounted on platforms that were rocked through the desired angular ranges by a motor driven cam. The position of the platform was monitored by a shaft encoder that divided the scan into 512 angular bins. The detectors were gas filled proportional counters. The X-ray events were summed in a register, and along with the various other instrument functions were recorded in the ground receiving station via the PCM telemetry. This was repeated at a rate of 256 Hz. An H-alpha camera relayed pictures to the experimenters who were able to control the aspect of the rocket. The images were also recorded on a 16mm film camera for post flight analysis. For further details see Final Report, Contract NAS2-6723 dated 15 February 1976.

In the report we describe the various aspects of the analysis of the X-ray data obtained by the two flights. These observations were coordinated with observations from the experiments on the Apollo Telescope Mount (ATM). Part of the work done during the course of this investigation was to relate the various data sets to one another. We participated in the Skylab Solar Workshop Series on Active Regions in Boulder, Colorado, which was sponsored by NASA and NSF. The Apendices attached to this report contain the published results, abstracts of papers, computer code descriptions and preprints of papers, all produced as a result of this research project.

Scientific Results

(a) Background

The basic goal of this research project was to obtain a holistic model of a solar active region using data from a wide range of instruments. The opportunity arose to tackle this problem with the coincidence of the flights of the two LPARL crystal spectrometer payloads with active observation periods on Skylab's ATM.

The project naturally divided itself into three distinct phases. The first consisted of the analysis and interpretation of the soft X-ray emission line data from the rocket borne experiments. The reduction of these data was essentially complete prior to the start of the contract. However, the interpretation and analysis of these data brought to light some interesting results. The second phase was to correlate the rocket observations with the cotemporal observations from other instruments, primarily those on the ATM. This was the most difficult part of the project to complete as it involved codifying the observations from other investigating groups, defining and calculating a common aspect solution as well as determining a relative calibration. This stage still remains the single largest possible source of uncertainty in the analysis. The last phase of the project involved modelling the regions using the assembled data and comparing the results. These stages are described in the following three subsections. The concluding subsection discusses briefly some of the interesting ideas that have resulted from this project, and especially during the Skylab Workshop on active regions, and the primary lessons learned from the analysis.

Fig. 1 - Sample Spectra

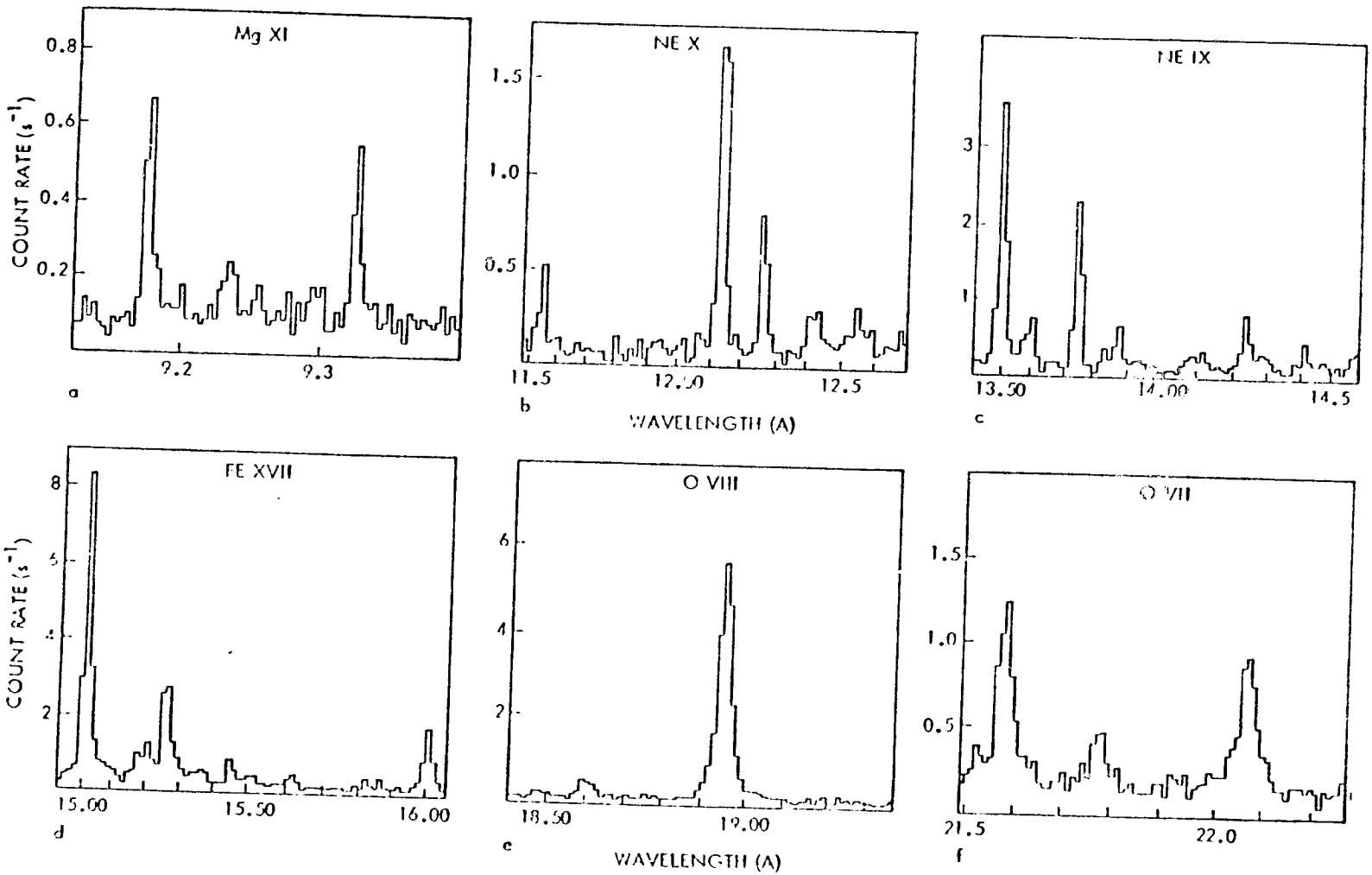

(b) Analysis of the X-Ray Emission Line Data from the Rocket Borne Experiments.

A vast quantity of data was accumulated during the two flights of this experimental package. Spectra were recorded from 31 stable pointing positions by all six spectrometers. At each pointing position every spectrometer produced two spectra of its dedicated wavelength band, one scanned in the wavelength increasing direction and the other scanned in the reverse direction. A total of 58 X-ray emission lines were definitely resolved with a possible 20 or more marginal features. Figure 1 shows typical spectra from the wavelength bands monitored during the flights.

The reduction and analysis of these data are summarized along with the results and will be submitted for publication in Solar Physics by Strong and Acton (Appendix 1). In Appendix 2 a full set of the results of the analysis are listed. As a result of the analysis we are able to summarize the primary results and conclusions under the following subheadings:

(i) Spectral Line Fitting Techniques.

We have developed a technique that fits an entire spectrum with a series of line profiles superimposed on a constant background using an iterative least squares technique. A Lorentzian line profile was assumed to represent our data. In the fitting procedure the position, width and peak count rate of each line as well as the background were left as free parameters where possible. Figure 2 shows the fit of our Fe XVII spectral interval with such a function.

Figure 2

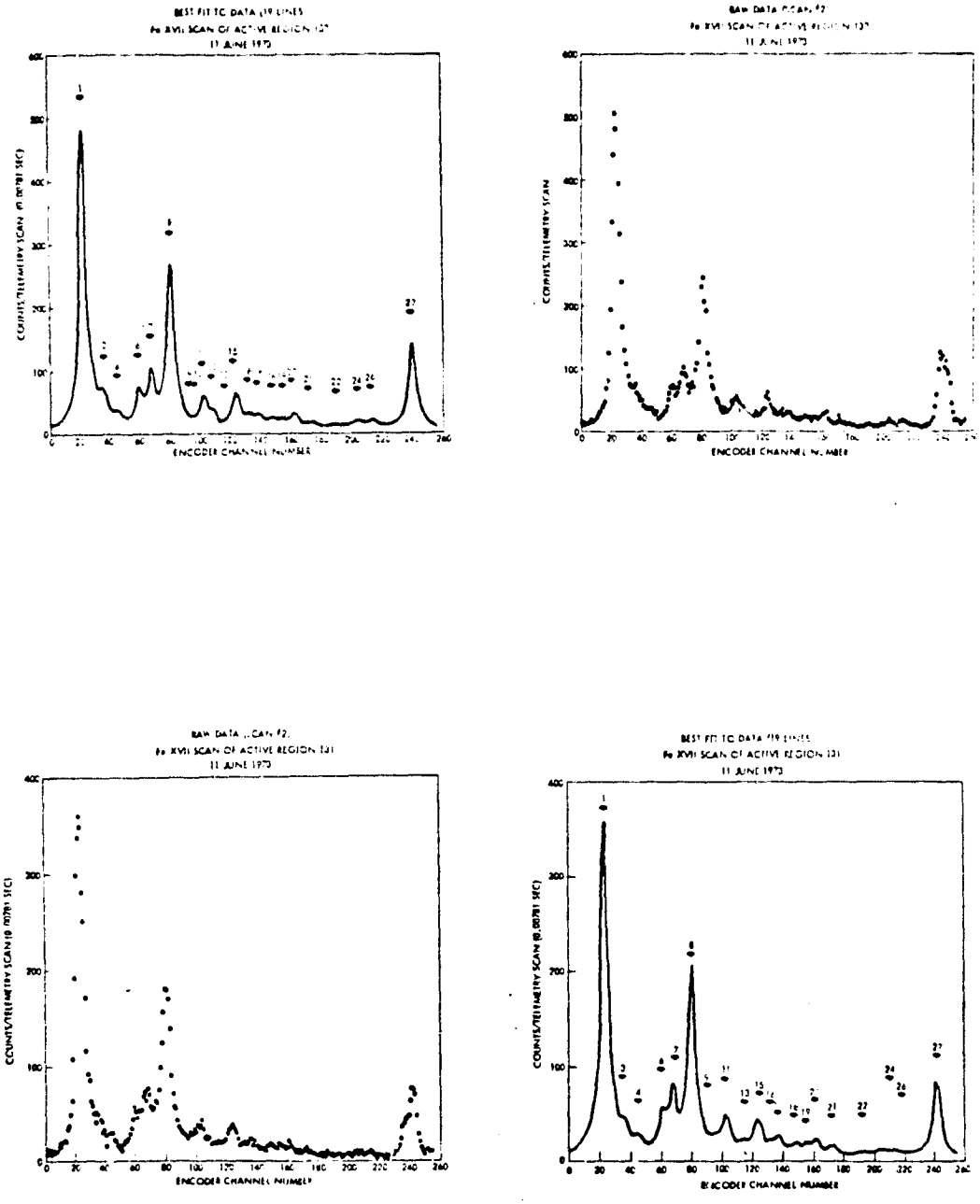

This technique made it possible to derive the integrated line intensity for each line from the fitted function. This has several advantages over summing the data and subtracting the average background which is an often-used method. Firstly, it eliminates confusion between any contribution to the background from the continuum and the wings of the lines in the spectrum. Secondly, by using the widths and positions of the more prominent lines it is possible to derive relatively accurate integrated line count rates for faint or blended lines. The uncertainties on the characteristic parameters of a given line derived from the least squares fitting procedure makes it possible to estimate quantitatively the uncertainties in the line count rates.

(ii) Preflight Calibrations.

We had available a comprehensive set of preflight calibrations which included the transmissions of the collimators, window support grids and detector windows. The integrated reflectivity of the crystals were kindly measured for us by A. Bureck. By combining these efficiencies, it was possible to derive the integrated line intensity for each line with the associated uncertainty.

(iii) Line Ratioing

Understanding the sources of the uncertainties on the line intensity made it possible to minimize their effect on any given result. The errors will be of two basic types. There are random errors introduced by statistical effects on measured quantities as well as systematic errors resulting from instrumental effects (geometry, wavelength, etc.). Also, there are problems associated with atomic data which are not always reliable. The best way of minimizing the selective effects is to take ratios of carefully chosen lines where some of these factors may be eliminated. The ratio of two emission lines for which emission can be represented by an effective temperature and emission measure is:-

$$\frac{I_1}{I_2} = \frac{f_1}{f_2} \cdot \frac{A_1}{A_2} \cdot \frac{\lambda_1}{\lambda_2} \cdot \frac{N_1}{N_2} \cdot 10^{-\left(\frac{5040(W_1-W_2)}{T_{eff}}\right)} \qquad (1)$$

adopting the usual nomenclature. Chosing lines from the same spectral scan can eliminate relative instrumental calibration error and reduce wavelength dependent effects. Other factors can be eliminated by choosing the correct combination of lines, for example:-

Two lines of the same ion yield a ratio dependent on their relative oscillator strength

$$\frac{I_1}{I_2} = \frac{f_1}{f_2} \cdot \frac{\lambda_1}{\lambda_2} \cdot 10^{-\left(\frac{5040(W_1-W_2)}{T_{eff}}\right)} \qquad (2)$$

Ratioing two lines of adjacent ionization stages of the same element will give information on the equilibrium state of the emitting plasma and its temperature.

$$\frac{I_1}{I_2} = \frac{f_1}{f_2} \cdot \frac{\lambda_1}{\lambda_2} \cdot 10^{-\left(\frac{5040(W_1-W_2)}{T_{eff}}\right)} \cdot \frac{N_i}{N_{i+1}} \qquad (3)$$

If we choose two lines with similar temperature functions then

$$C(T) = \frac{N_1}{N_2} \cdot 10^{-\left(\frac{5040(W_1-W_2)}{T_{eff}}\right)} \approx \text{constant}, \qquad (4)$$

then we obtain a ratio that is sensitive to the relative elemental abundances:-

$$\frac{I_1}{I_2} = \frac{f_1}{f_2} \cdot \frac{\lambda_1}{\lambda_2} \cdot C(T) \cdot \frac{A_1}{A_2} \qquad (5)$$

Three typical examples are calculated in Tables I - III.

These methods were applied to our data with some useful results. Especially interesting were the results of the abundance ratio of $O:N_e$. We had sufficient results to do a statistical study of the problem. The data basically gave a result of 6.0(0.5) however, there were some interesitng departures from the value. Some regions from the flight of Aerobee 26.002 indicated a value of 12(2) assuming active region temperatures ($\sim 3.10^6$ ^oK). These results can be explained in terms of a higher temperature component in the emitting plasma with some justification from the Hα observations from Big Bear Observatory. However, the strongest region observed in McMath 12387 gave a value of 4.0(1.0) which can be explained in terms of a real difference in the abundance ratio if the observations are correct. Figure 3 shows the results of this particular study. See Appendix 1 for a more detailed discussion of this analysis.

(iv) Resonance Scattering

Probably one of the most important results of this analysis has been the discovery of significant variations in the ratios of the sum of the forbidden and intersystem line intensities to that of the resonance line (the G ratio) for the O VII ion (see Figure 4). We have been able to interpret these data in terms of resonance scattering. This has triggered a study of the problem comparing a simple model of the scattering of X-rays in the corona with observations of the equivalent case. The resulting paper has been submitted to the Astrophysical Journal, a copy is contained in Appendix 3. We have also put a proposal to NASA for an expanded study of the problem and its implications.

(v) Modelling of the Active Regions.

The relative brightnesses of the most prominent lines from each stable pointing position in and around each active region made it possible to

Figure 3

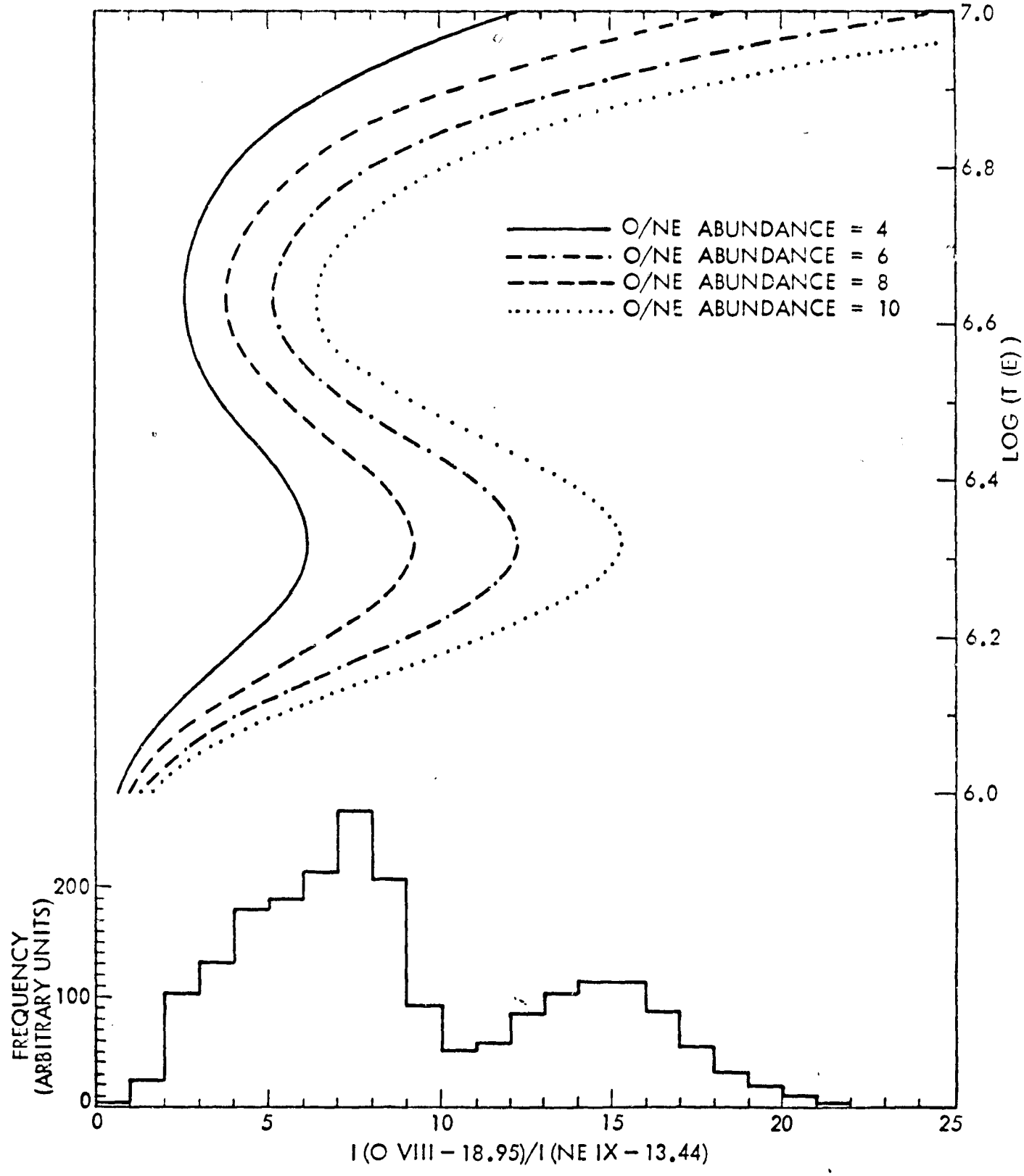
O/NE ABUNDANCE = 4
O/NE ABUNDANCE = 6
O/NE ABUNDANCE = 8
O/NE ABUNDANCE = 10
7.0
6.8
6.6
6.4
6.2
6.0
LOG (T (E))
FREQUENCY (ARBITRARY UNITS)
200
100
0
0
5
10
15
20
25
I (O VIII – 18.95)/I (NE IX – 13.44)

TABLE I

Temperature Dependence of the O VIII (18.95A) to Ne IX (13.44A)

Intensity Ratio (Jordan)

T_6	Log T	$\frac{1.352}{T_6}$	$\text{Log}(\frac{F_1 \lambda_1}{F_2 \lambda_2})$	$\text{Log}(A_{\text{Ne IX}})$	$\text{Log}(A_{\text{O VIII}})$	Ratio
1.00	6.00	1.352	-0.085	-0.03	-2.09	0.161
1.26	6.1	1.073	-0.085	-0.01	-1.28	0.522
1.58	6.2	0.856	-0.085	0	-0.72	1.124
2.00	6.3	0.676	-0.085	-0.01	-0.42	1.517
2.51	6.4	0.539	-0.085	-0.04	-0.36	1.361
3.16	6.5	0.428	-0.085	-0.15	-0.53	0.918
3.98	6.6	0.340	-0.085	-0.38	-0.82	0.653
5.01	6.7	0.270	-0.085	-0.80	-1.14	0.700
6.31	6.8	0.214	-0.085	-1.33	-1.46	0.999
7.94	6.9	0.170	-0.085	-1.90	-1.75	1.719
10.00	7.0	0.135	-0.085	-2.44	-2.00	3.093

TABLE II

Temperature Dependence of the Ne X (12.13Å) to Mg XI (9.17)

Intensity Ratio

T	Log(T)	$\frac{1.667}{T}$	$\text{Log}(\frac{F_1}{F_2} \cdot \frac{\lambda_1}{\lambda_2})$	$\text{Log}(A_{\text{Ne X}})$	$\text{Log}(A_{\text{Mg XI}})$	Ratio
1.00	6.0	1.67	-0.130	-5.16	-1.09	0.003
1.26	6.1	1.32	-0.130	-3.75	-0.30	0.005
1.58	6.2	1.05	-0.130	-2.63	-0.07	0.023
2.00	6.3	0.84	-0.130	-1.71	-0.02	0.105
2.51	6.4	0.66	-0.130	-1.02	-0.01	0.331
3.16	6.5	0.53	-0.130	-0.58	-0.01	0.676
3.98	6.6	0.42	-0.130	-0.36	-0.04	0.933
5.01	6.7	0.33	-0.130	-0.40	-0.11	0.813
6.31	6.8	0.26	-0.130	-0.62	-0.24	631
7.94	6.9	0.21	-0.130	-0.92	-0.60	0.575
10.00	7.0	0.17	-0.130	-1.20	-1.06	0.794
12.59	7.1	0.13	-0.130	-1.49	-1.58	1.230
15.84	7.2	0.11	-0.130	-1.74	-2.19	2.692

TABLE III

Temperature Dependence of the Mg XI (9.17) to Fe XVII (15.01)

Intensity Ratio

T_6	Log(T)	$\frac{-2.651}{T_6}$	$\text{Log}(\frac{F_1}{F_2} \cdot \frac{\lambda_1}{\lambda_2})$	$\text{Log}(A_{\text{Ne XI}})$	$\text{Log}(A_{\text{FeXVII}})$	Ratio
1.0	6.0	-2.651	-0.681	-1.09	-	-
1.26	6.1	-2.104	-0.681	-0.30	-4.77	48.32
1.58	6.2	-1.678	-0.681	-0.02	-2.00	0.418
2.00	6.3	-1.326	-0.681	-0.01	-0.44	0.026
2.51	6.4	-1.056	-0.681	0.01	-0.10	0.023
3.16	6.5	-0.839	-0.681	-0.04	-0.04	0.034
3.98	6.6	-0.666	-0.681	-0.11	-0.17	0.052
5.01	6.7	-0.529	-0.681	-0.29	-0.37	0.074
6.31	6.8	-0.420	-0.681	-0.60	-0.76	0.114
7.14	6.9	-0.334	-0.681	-1.06	-1.41	0.216
10.00	7.0	-0.265	-0.681	-1.58	-2.36	0.682

create simple maps of the emission using the higher spatial resolution data ($\sim$ 35"), see Figure 5. Generally we found a close correspondance between the resulting maps for various lines with a tendancy for the lower temperature lines (O VII and O VIII) to have a more extensive area of emission.

Using a modelling technique first described by Withbroe (1975) we derived a series of models of the differential emission measure for each stable pointing position. Generally the X-ray emission line intensities could be reproduced by an isothermal peak ($2.0 - 4.0.10^6$ ^oK) with a width of $0.3 - 0.4.10^6$ ^oK. This result could be expected as the thermal conductivity of the coronal plasma is high at these temperatures, and the temperature resolution of the X-ray line is low.

The X-ray lines available to us from these spectra are only really sensitive to temperature in the range $1.5.10^6$ ^oK (O VII) to $8.0\ 10^6$ ^oK. (Ne X). Hence, we have little or no information on the cooler plasma associated with the transition region or particularly hot material from flaring regions. Hence, there was a need to call on other sources of data to fill these gaps in our models.

We did carry out an investigation of the stability and applicability of the Withbroe technique in the light of some criticism of Craig and Brown (1976, and subsequent papers). We found the results to be generally reliable and not to reflect the condition numbers of about 50 indicated by Craig and Brown.

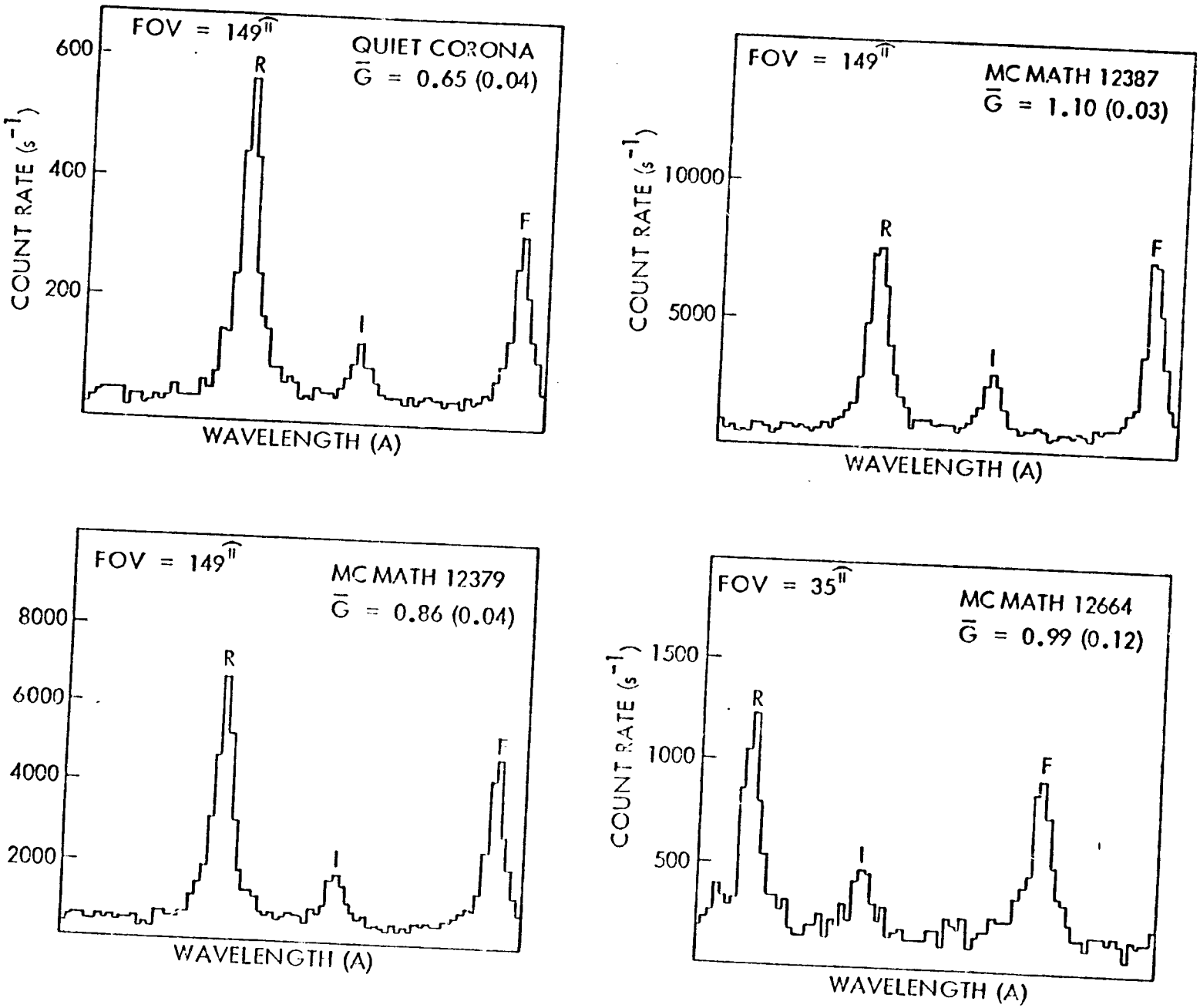

Figure 4

Figure 5

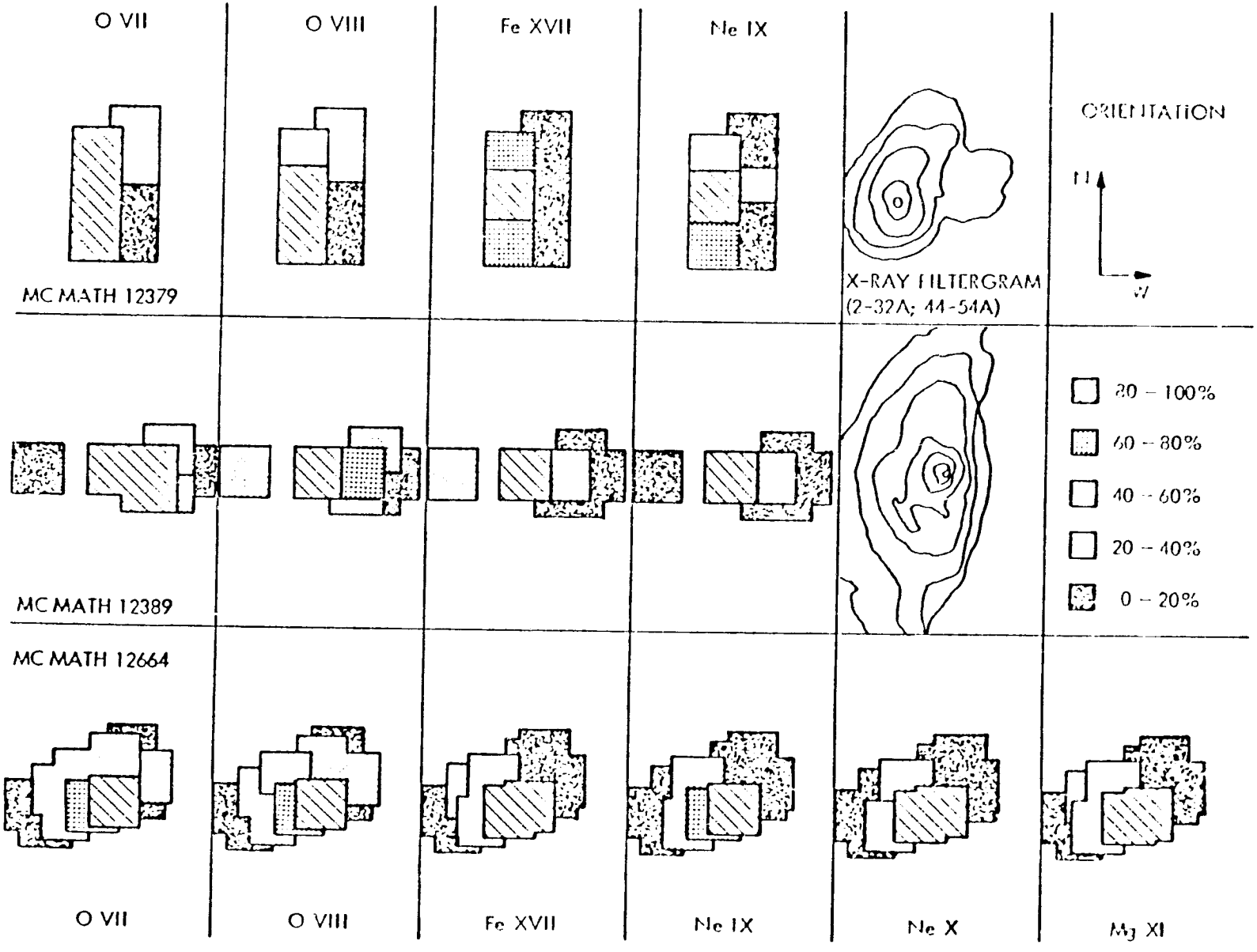
O VII
O VIII
Fe XVII
Ne IX
ORIENTATION
N
W
MC MATH 12379
X-RAY FILTERGRAM
(2-32A; 44-54A)
80 – 100%
60 – 80%
40 – 60%
20 – 40%
0 – 20%
MC MATH 12389
MC MATH 12664
O VII
O VIII
Fe XVII
Ne IX
Ne X
Mg XI

(c) Modelling of McMath 12379 and 12387

Simultaneous observations of McMath 12379 and McMath 12387 were available from the instruments on the Apollo Telescope Mount (ATM). Hence there were available to us a wide range of X-ray and EUV data on these regions. These instruments offered an expanded temperature range for the models into the lower corona ($\gtrsim 3.10^5$ ^{o}K) as well as an improvement in the temperature resolution of the model due to the more narrow temperature functions of the EUV lines.

There were four ATM experiments used in this investigation. SO-54 (AS&E) took high spatial resolution ($\sim 2''$) filtergrams in the soft X-ray (2-50Å) part of the solar spectrum. SO-56 (MSFC) was a similar instrument. These were used to reconsile the aspect solution of the X-ray data from the rocket borne spectrometers as well as be a check on the final models derived from the X-ray and EUV emission line data. SO-55 (HCO) produced raster images ($5' \times 5'$) at a spatial resolution of $5''$ in several prominent EUV lines. SO-82A (NRL) produced overlapping images of the solar disk at a $1''$ resolution in the 180 - 650Å wavelength band. Data from these experiments were used in conjunction with the X-ray line intensities from the rocket flights to produce the differential emission measure models.

It is evident from the descriptions of these instruments (for greater details on them see "Applied Optics" special edition on Skylab) that there is a considerable variation in the type of data obtained from the ATM instruments. Consequently, each had to be reduced, analyzed and correlated with our data in different ways. The basic problems can be summarized as follows:

(i) Timing of Observations; not all of the experiments took data at the same moment as the rocket data was recorded. Also the observations took different times to be accumulated. Consequently, we had to study the preceding and subsequent data on these regions to establish whether they were stable over the observation periods. However, where possible, data not taken during the time frame of the rocket flights were not used. This is especially important for McMath 12664 which was particularly active.

(ii) Spatial Resolution; each data set had its own definable spatial resolution. This varied from about 1 arc second (NRL-S082A) to the rocket data ($\sim$35 arc seconds FWHM). Hence, the data sets had to be made compatible with one another. As we can do very little to improve the resolution of the X-ray data taken through the collimators on the Bragg crystal sepctrometers, then it was necessary to degrade the spatial resolution of the ATM data to match it. This was done by multiplying the collimator efficiency with the intensity of radiation from each resolution element of the image as a function of position from the calculated point location.

(iii) Aspect Solutions; we had to relate the calculated locations of each stable rocket pointing position to a position on the image raster of each experiment. The absolute pointing parameters for ATM were not well established, nor were their relative pointing at least to the accuracy required in this investigation.

(iv) Calibration; we had to establish the relative calibrations of the various ATM instruments and the X-ray crystal spectrometers.

The ATM instruments were not designed with this type of analysis in mind. There have been attempts to combine X-ray emission line data with X-ray filtergrams (Davis et al., 1975; Pye et al., 1977). While the temperatures of the

regions studied have been in good agreement the total emission measure has shown some discrepancies. These investigations involved the use of data from a wide field of view spectrometer (3 - 4 arc min. FWHM). The finer resolution available to us made the resolution of the aspect problem vitally important to this investigation. The analysis is summarized under the following subheadings:

(i) The Available Data.

Table IV lists all the sources of data available to this investigation for both flights.

(ii) Solving the Aspect Problem.

As mentioned above, this problem was the most important (and time consuming) in being able to compare these data sets. The rocket aspect solutions were derived by Acton using the outputs of the Fine Sun Sensor (FSS) and correlating them with the photographic data recorded by the on-board H-alpha camera. We believe these to have an uncertainty of $\leq$ 20 arc seconds in absolute terms. However, the relative pointing positions (i.e. the pattern of the stable pointing positions) over each region is more accurate. Figures 6(a) and (b) show the final rocket aspect solutions with respect to the solar disk and active regions.

We used the SO-54 images to establish pointing locations of the rocket data in conjunction with the relative intensities of the Fe XVII emission line at 15.01A to improve or, at least, confirm our pointing with respect to the ATM instruments. We noted that the Fe XV and Fe XVI images from the SO-82A data were similar to those images of the "softest" filter available to SO-54 (Filter 2 - patrol normal). Using the IDAPS system at MSFC a pointing position pattern of collimator functions were moved over the regions observed until a best fit was found

TABLE IV

Summary of Coordinated Observations Associated with LPARL Rocket.

Observations	26.002	26.003
ATM Rocket launch Time	18:30 UT, 11th June 1973	22:05 UT, 19th December 1973
1. ATM Instruments		
AS&E spectrographic Telescope SO-54 (4-60A)	Good coverage of both AR's	Thick filter only.
EUV spectrometer-spectroheliometer SO-55 (280-1350A)	12387 only, grating in wrong position	Good coverage
X-Ray Telescope SO-56 (3-53A)	Good coverage of both AR's	Good coverage
XUV spectroheliograph SO-82A (171-630A)	Good coverage of both AR's	Prior coverage may be useful
UV Spectrograph SO-82B (970-1970A)	Good coverage of 12387	?
White light Coronagraph SO-52	?	?
Hα Telescope (6563A)	Good coverage	Good coverage
2. Ground Based		
Big Bear (Hα Full Disk)	18:16 - 02:15 UT	16:27 - 23:28
Sac Peak (Full disk spectroheliograms)		
D_3, Hα-4.31A & Ca k	18.09	21.07
Hα, B + Ca k + 0.38A	18.12	20.55
Hα + 0.5A	18.18	21.02
Big Bear (McMath 12387)		
Hα-0.5A, 4.2x5.6 arc min	18.12 - 02.05	X
Hα-0.5A, 4.2x5.6 arc min	18.12 - 02.15	16.27 - 23.28
CaK-0.5A, 4.2x5.6 arc min	18.12 - 02.05	X
CaK-0.5, 1/6 Disk	X	17.50 - 22.40
Lockheed Filter grams - large scale		
He I D_3(5876A)-8x6 arc min	18.26 - 18.41	X
Hα Doppler (Hα±0.6A) 10x7.5	17.38 - 22.01	X
Hλ Multislit spectrograph 10x7.5	17.38 - 22.01	X

Observations	26.002	26.003
Magnetograms		
Crimea	McMath 12379	X
Coronographs & Prominences		
Maung Lou (6200A)	17.00 - 03.00	17.00 - 03.00
Sac Peak	18.43 - 20.22	X
Radio Observations		
Clark lake 20-120 MHz 15-2.5m	15.18 - 02.18	X
John Hopkins Applied Physics Lab 565 1000 MHz	12.19 - 19.56	X
Harvard 10-4000 MHz	X	sunrise - sunset

between the normalized relative intensities of the two data sets. An empiricle parameter (ϕ) was defined to express the comparability of the results, such that:-

$$\phi = \Sigma\left(\frac{I'_n}{I'_{max}} - \frac{I''_n}{I''_{max}}\right)^2 \qquad (6)$$

where n is the pointing location identifier. I' and I" are the intensities recorded by the rocket and ATM instruments in their own respective units. I'_{max} and I''_{max} are the values of the intensities of the brightest point in the pattern. We found that there was a neglibable translational motion and a small rotation ($\sim 2^{o}$) required to find the minimum of ϕ within the uncertainty of the rocket pointing locations. The rotation is of little consequence to McMath 12379 as it is near to the disk center but could have been important to McMath 12387 which was on the eastern limb of the sun. The coordinates of the sun center and the active regions could be derived by overlapping a Stoney-Hurst disk, Figure 6.

(iii) Analysis of the SO-82A Data.

Two exposures were available of these regions (1A233 - a short wavelength plate -9.5s; and 1A235 - a long wavelength plate -79.5s). A total of 10 scans of the entire active regions were made of the images at various wavelengths using the microdensitometer at NRL. Due to calibration problems some of the low temperature lines of oxygen were not available to us. However, scans were made of both regions in Ne VII (465Å), Si XII (499Å); Mg IX (368Å). Fe XV (284Å) and Fe XVI (335Å or 361Å).

Solving the coalignment problem was achieved by measuring the position of the disk center of the He II (304Å) and Ne VII images from the

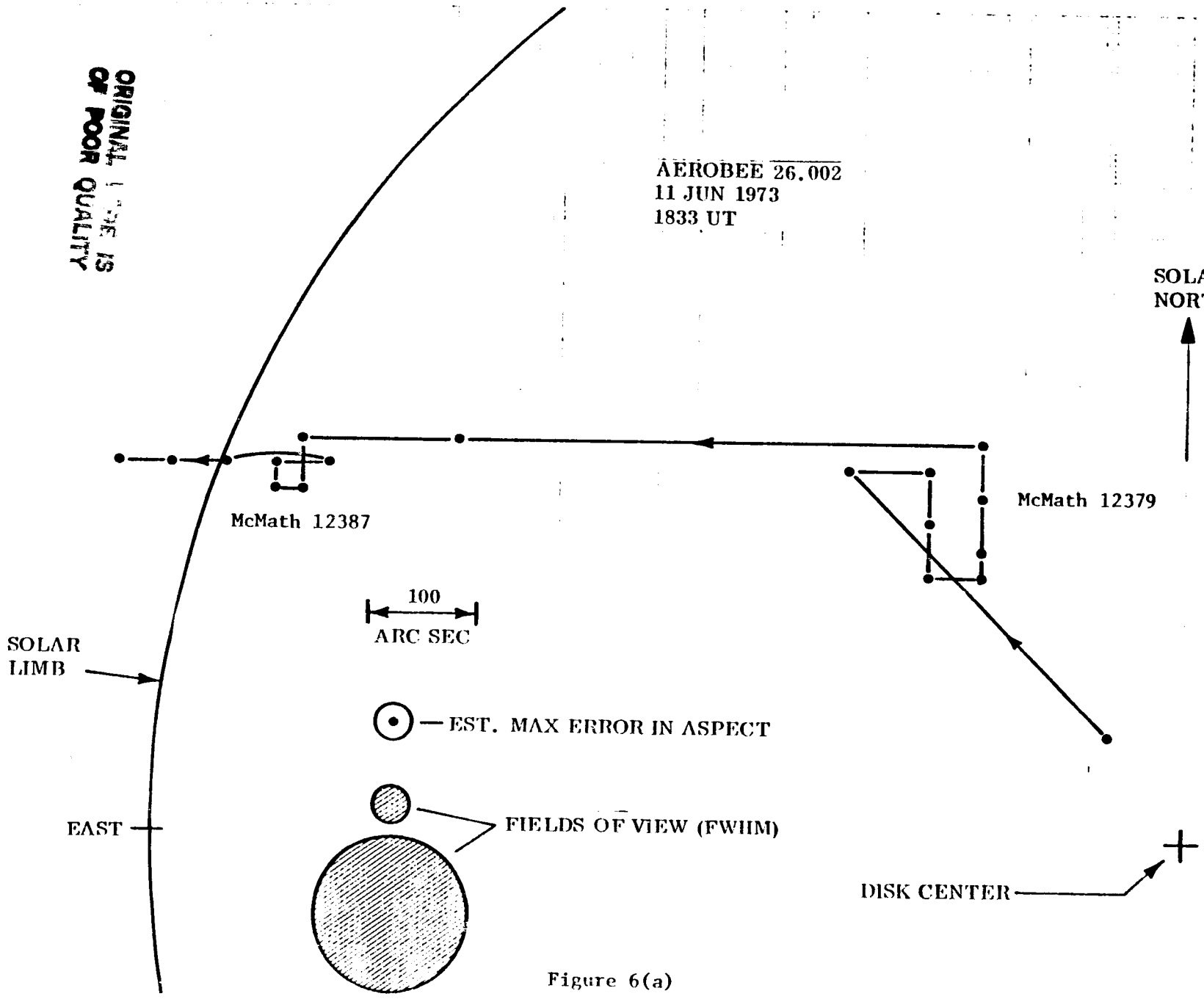

Figure 6(a)

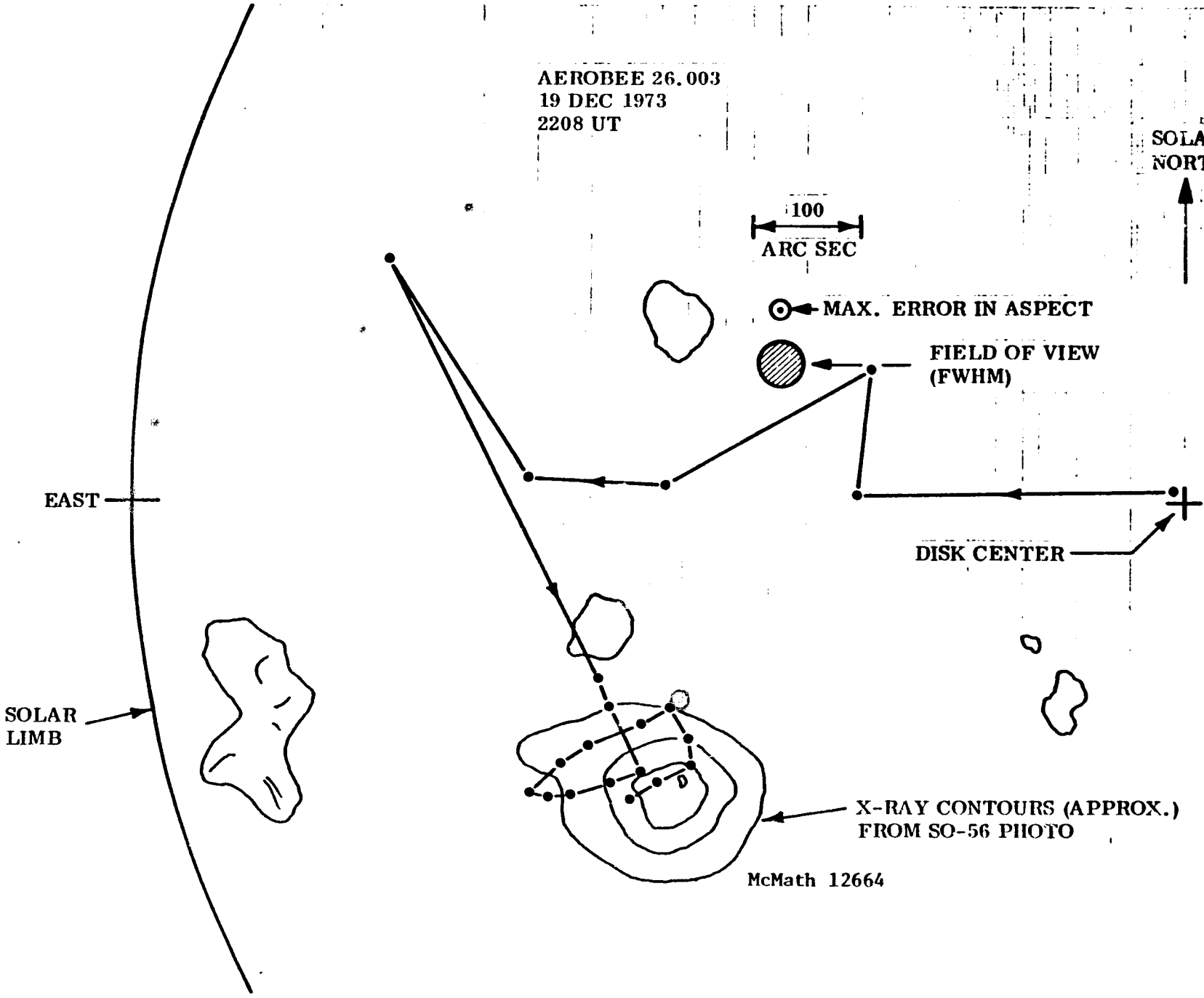
AEROBEE 26.003
19 DEC 1973
2208 UT
SOLAR
NORTH
100
ARC SEC
MAX. ERROR IN ASPECT
FIELD OF VIEW
(FWHM)
EAST
DISK CENTER
SOLAR
LIMB
X-RAY CONTOURS (APPROX.)
FROM SO-56 PHOTO
McMath 12664

Figure 6(b)

Figure 6 (c)

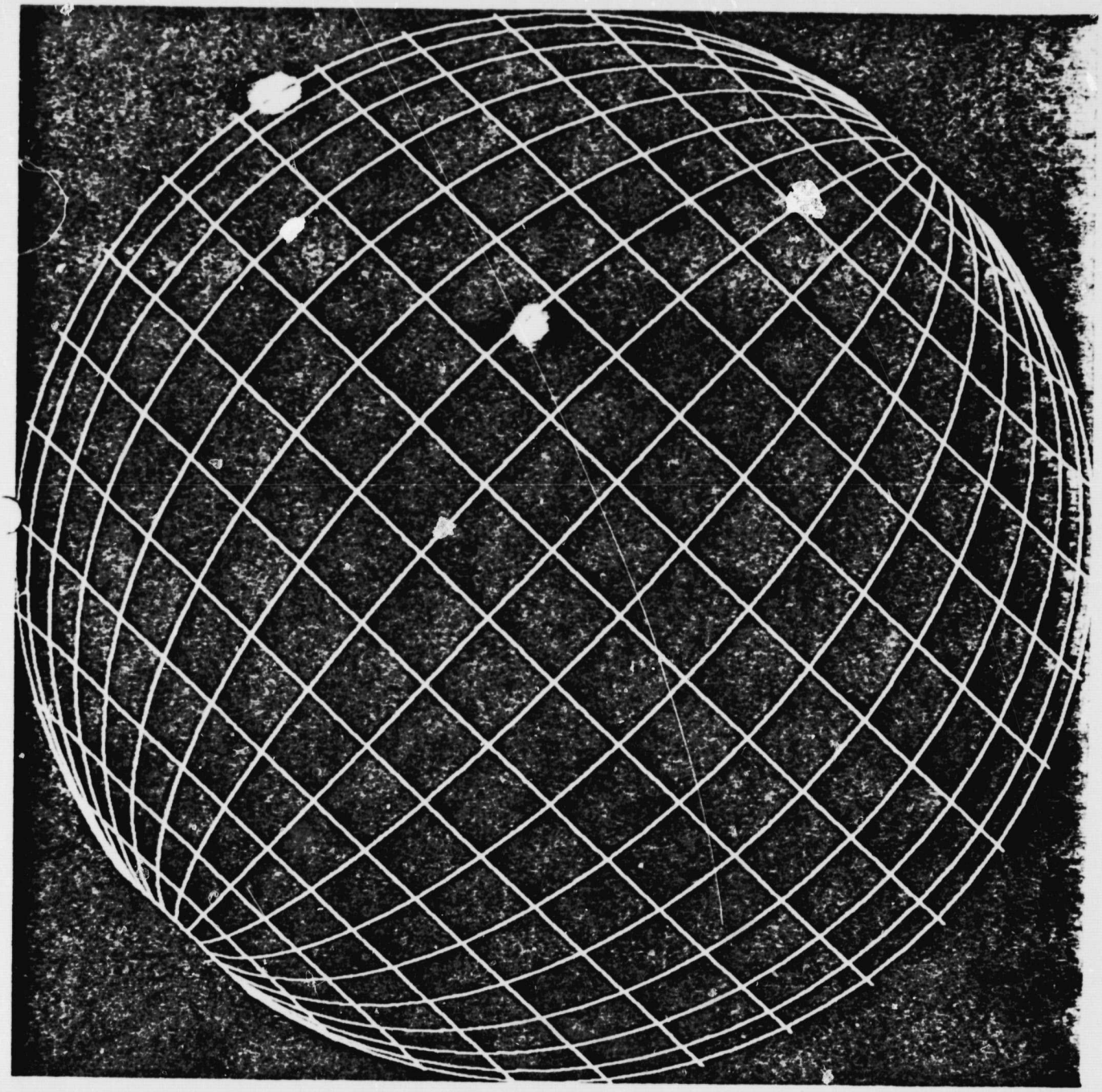

coordinates (in the microdensitometer's system) of 4 orthogonal limbs. Knowing the dispersion of the plates the position of the disk center could be derived for every other image. The orientation of the image is also known, hence the positions of the rocket experiment's fields of view can be calculated. See Figures 7(a) and 7(b).

We derived the equivalent EUV line intensity for each of the above lines at every stable pointing position by convolving the intensity of each resolution element (1 arc sec) with the collimator efficiency at that position and summing the results. The SO-82A calibration curves were supplied by K. Dere.

(iv) Combining the X-ray and EUV data to produce differential Emission Measure Models.

Again we used Withbroe's (1975) technique to model the differential emission measure as a function of temperature. The data is presented in Table V. The quantity in parenthesis is the "fitting ratio" and is defined as the ratio of the observed to predicted (from the model) line intensities. Generally, the data seemed internally consistent with the lines conforming to the models well. Three lines were chosen in each model to have the heaviest weight in the fitting procedure. These were the brightest lines that defined the full temperature range (Ne VII, O VII, Fe XVII). The models are shown in Figures 8(a) and (b). The integral emission measure is also listed on the figures. The models were stable, with the exceptions of McMath 12379-7, Move to 12387, McMath 12387-10 and 13, which are not shown in the figures.

The models have several interesting characteristics. The low temperature end is defined by Ne VII which gives rise to a plateau, generally there is a small peak in the distribution at about $2\text{-}3.10^6$ ^oK followed by a

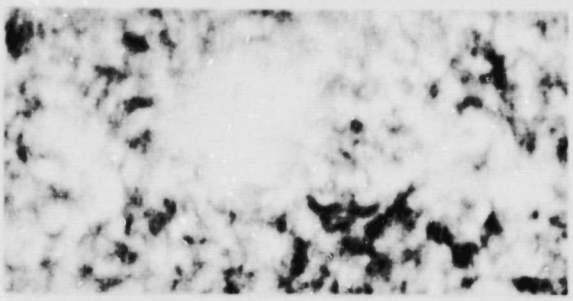

(a) He II 304A (NRL)

(b) O V 630A (NRL)

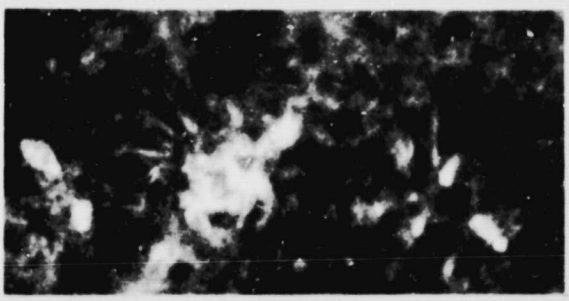

(c) Ne VII 465A (NRL)

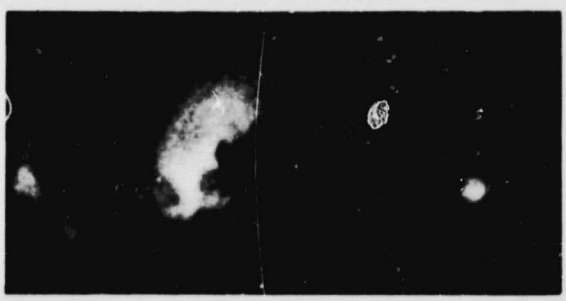

(d) Si XII 499A (NRL)

(e) Mg IX 368A (NRL)

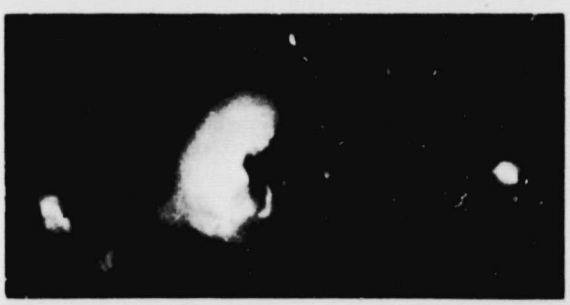

(f) Fe XV 284A (NRL)

(g) SOFT X-RAY FILTER (MSFC)

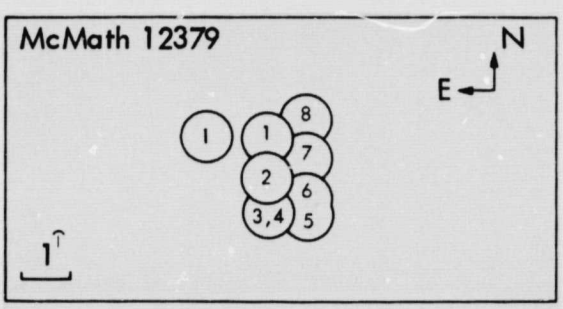

(h) Aerobee 26.002 POINTING POSITIONS

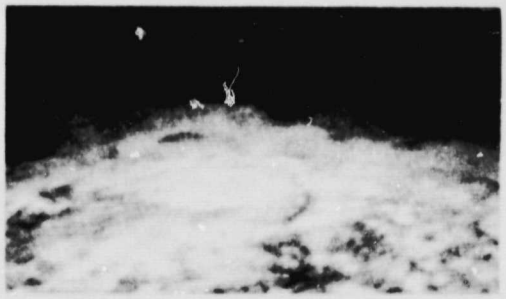

(a) He II 304A (NRL)

(b) O V 630 A (NRL)

(c) Ne VII 465A (NRL)

(d) Si XII 499A (NRL)

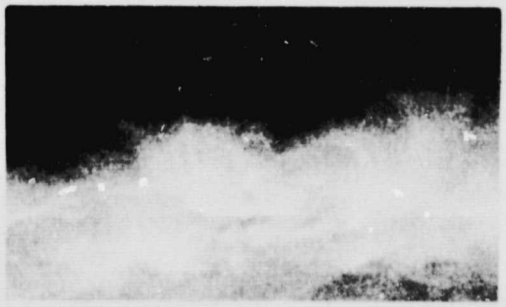

(e) Mg IX 368A (NRL)

(f) Fe XV 284A (NRL)

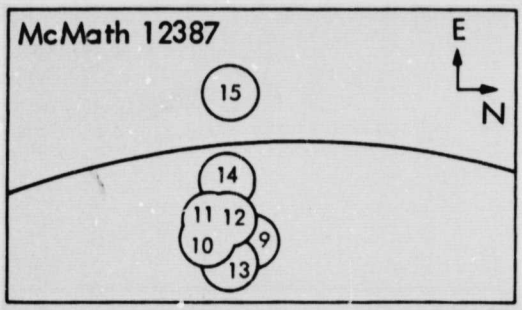

(g) Aerobee 26.002 POINTING POSITIONS

b) HARD X-RAY FILTER (MSFC)

FIGURE 8(A)

AEROBEE 26.002 DIFFERENTIAL EMISSION

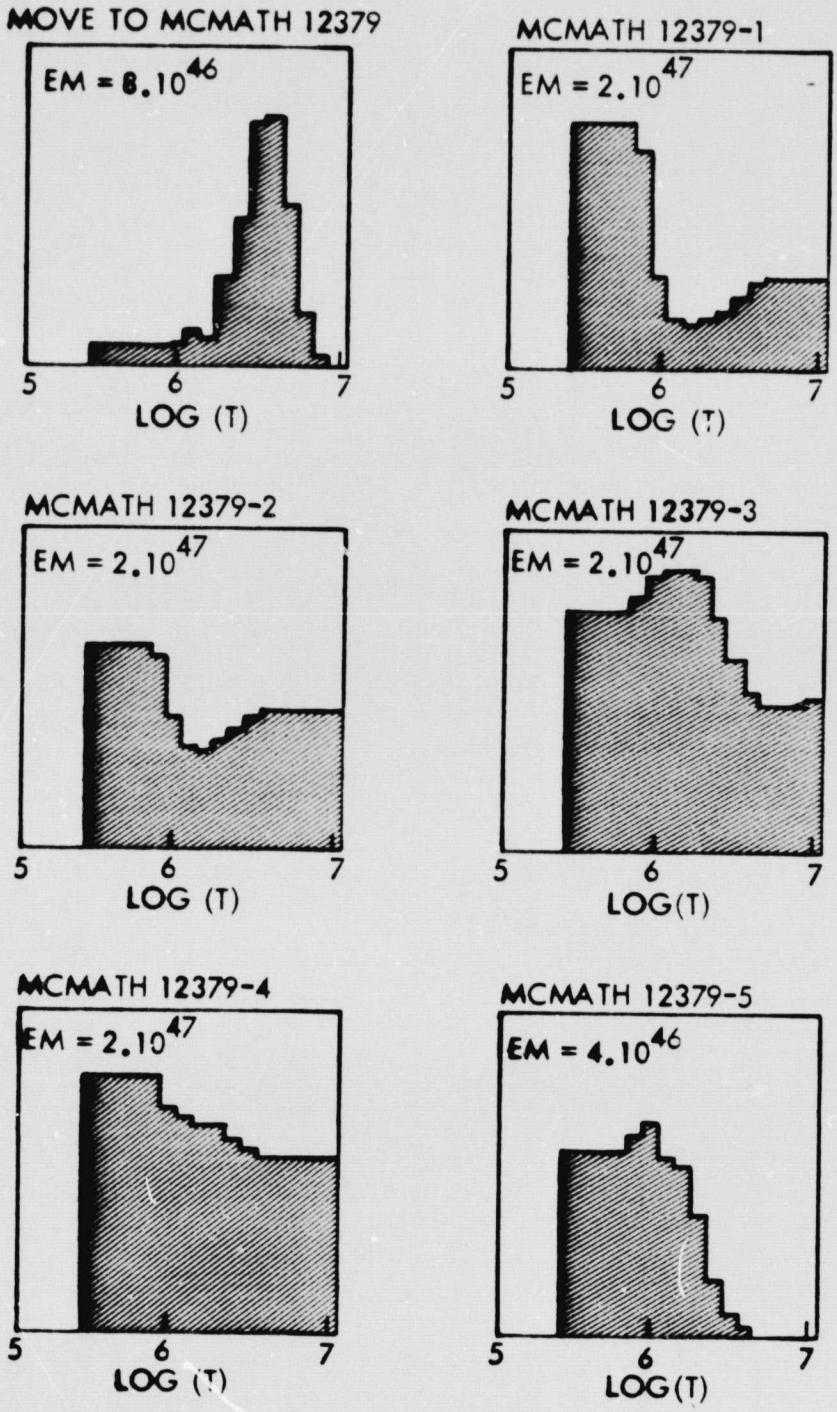

FIGURE 8(B)

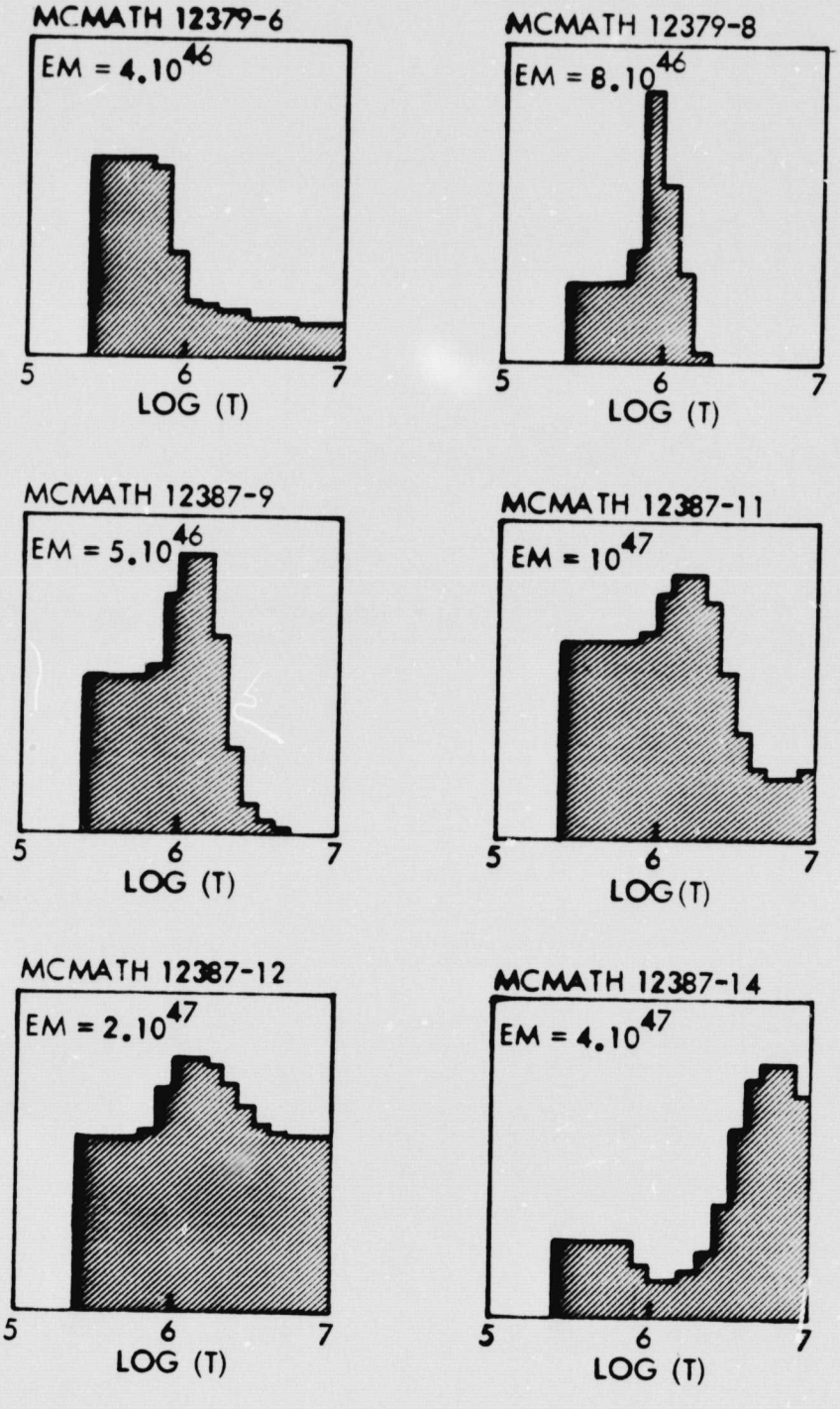
MCMATH 12379-6
EM = 4.10^46
5
6
7
LOG (T)
MCMATH 12379-8
EM = 8.10^46
5
6
7
LOG (T)
MCMATH 12387-9
EM = 5.10^46
5
6
7
LOG (T)
MCMATH 12387-11
EM = 10^47
5
6
7
LOG(T)
MCMATH 12387-12
EM = 2.10^47
5
6
7
LOG (T)
MCMATH 12387-14
EM = 4.10^47
5
6
7
LOG (T)

sharp downward slope at higher temperatures. However, some distributions have no peak and the emission measure drops away from the Ne VII defined plateau. The significance of the gradients and maxima are reduced by the absolute intensity uncertainties of the lines (40%) and the pointing errors. However, the emission measure peaks bear a close similarity to those published by Withbroe (1975) and Levine and Pye (1979).

The major anomaly in the data is the large discrepancy between the models and the intensity of Fe XV and Fe XVI. Inclusion of these data in the analysis never led to a stable model, hence they were excluded. The source of this anomaly has not been determined as yet but could be due to blending in these images with other features.

(v) Comparison of the Emission Measures derived from different sources.

SO-54 also had good coverage of McMath 12379. These data were analyzed to deduce the intensity and emission measure contours for this region. See Figures 9 and 10. Using the pointing positions established from the ATM orientation and measurements of the white light disk center, we derived the approximate emission measure from these contours. The results are listed in Table 6.

The results indicate that the emission, as seen by the X-ray spectrometer and EUV spectroheliograph, are consistent within measurement uncertainties where as the SO-54 data consistently gave a low value in the emission measure by a factor of between 2 and 7. The source of this discrepancy is as yet undermined. We estimate that the total emission measure for McMath 12379 is 5.10^{47}, compared to 8.10^{47} for McMath 12387.

TABLE V

Modelling Parameters (ergs/cm^2/sec/st)

Region ID	Ne VII[1]	Fe XV*	Si XII	O VII[1]	Fe XVI*	O VII[1]	Ne IX	Fe XVII[1]	FIT
McMath 12379	182(1.0)	1500(10)	953(.97)	-	1350(1.0)	-	-	-	Good
#1	371(1.0)	2500(19)	-	635(1.0)	1630(16)	1110(1.2)	-	1270(1.0)	Poor
#2	315(1.0)	3220(12)	465(2.8)	1170(1.0)	1960(11)	1840(1.2)	504(2.3)	1950(1.0)	Poor
#3	204(1.0)	3250(10)	-	1190(1.0)	2040(12)	2080(1.9)	422(2.9)	1190(1.0)	Good
#4	204(1.0)	3250(13)	296(2.1)	999(1.0)	2040(14)	2080(1.9)	291(1.9)	1300(1.0)	Good
#5	150(1.0)	3230(26)	261(5.2)	416(1.0)	2570(61)	237(1.5)	-	140(1.0)	Good
#6	156(1.0)	3140(51)	277(8.3)	247(1.0)	2530(72)	337(1.0)	-	289(1.0)	Good
#8	296(1.0)	2550(22)	317(6.4)	618(1.0)	1910(63)	539(1.0)	460(6.5)	296(0.2)	Good
McMath 12387									
#9	133(1.0)	-	186(2.3)	673(1.0)	1650(50)	519(0.4)	68(2.5)	152(1.0)	Good
#10	146(1.0)	-	-	312(1.0)	-	-	-	-	Poor
#11	164(1.0)	-	195(1.6)	934(1.0)	2490(43)	1080(1.8)	103(1.3)	593(1.0)	Good
#12	146(1.0)	-	206(1.3)	1190(1.0)	2170(26)	1590(1.3)	260(1.6)	1420(1.0)	Poor
#13	134(1.0)	-	163(1.3)	182(0.8)	-	-	-	-	Bad
#14	166(1.0)	-	263(14)	1150(1.0)	2490(23)	2610(1.0)	1160(3.0)	3840(1.0)	Poor

* Not used in modelling procedure as fluxes anominously high.

[1] Fit forced on these lines.

FIGURE 9

INTENSITY MAP OF MCMATH 12379

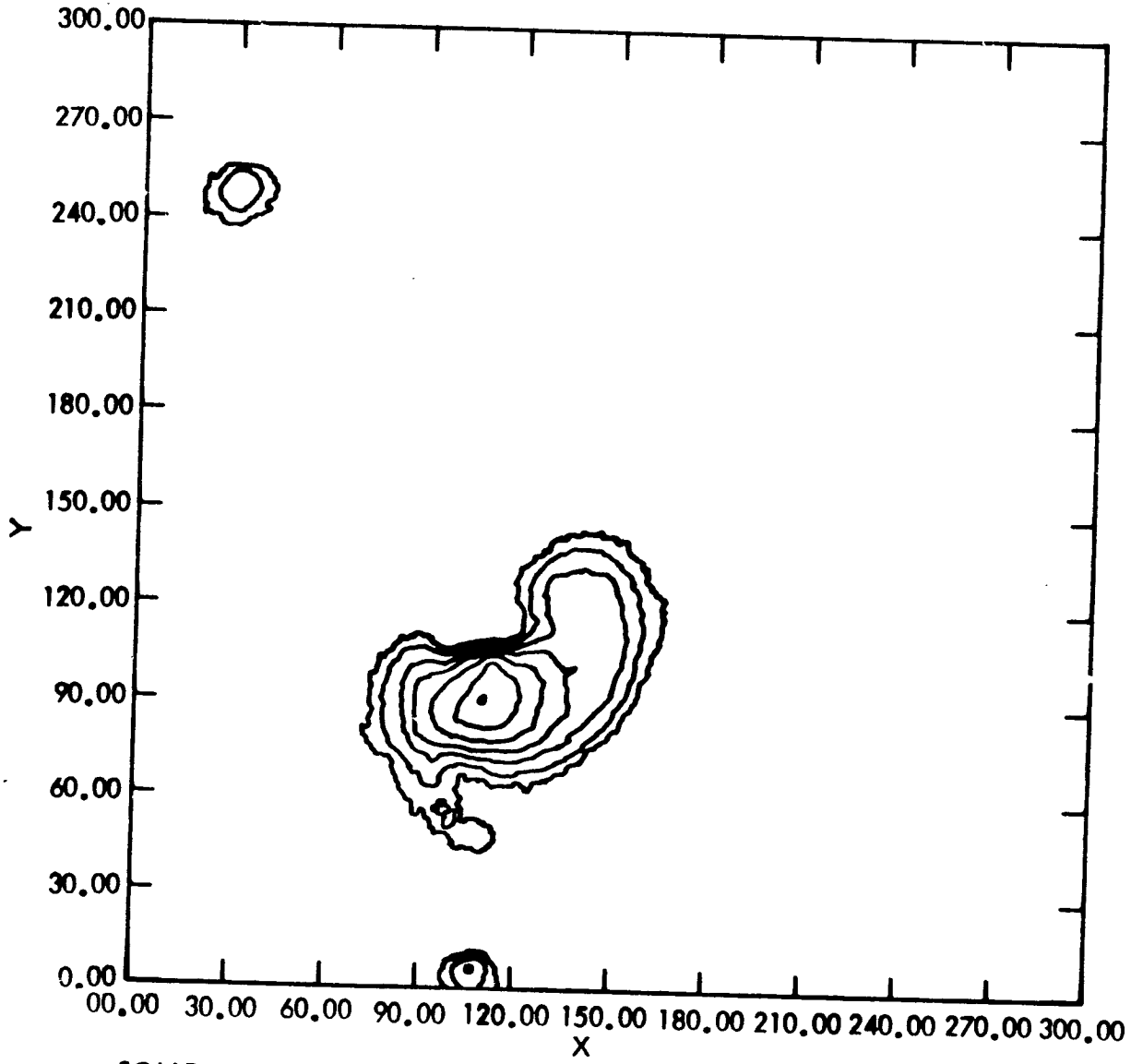

SCALE : 1 INCH 3 00000E+01 PICELMS

A4577 PRF26L.S512BEF SCALE = 60"/INCH

FIGURE 10

EMISSION MEASURE MAP OF MCMATH 12379

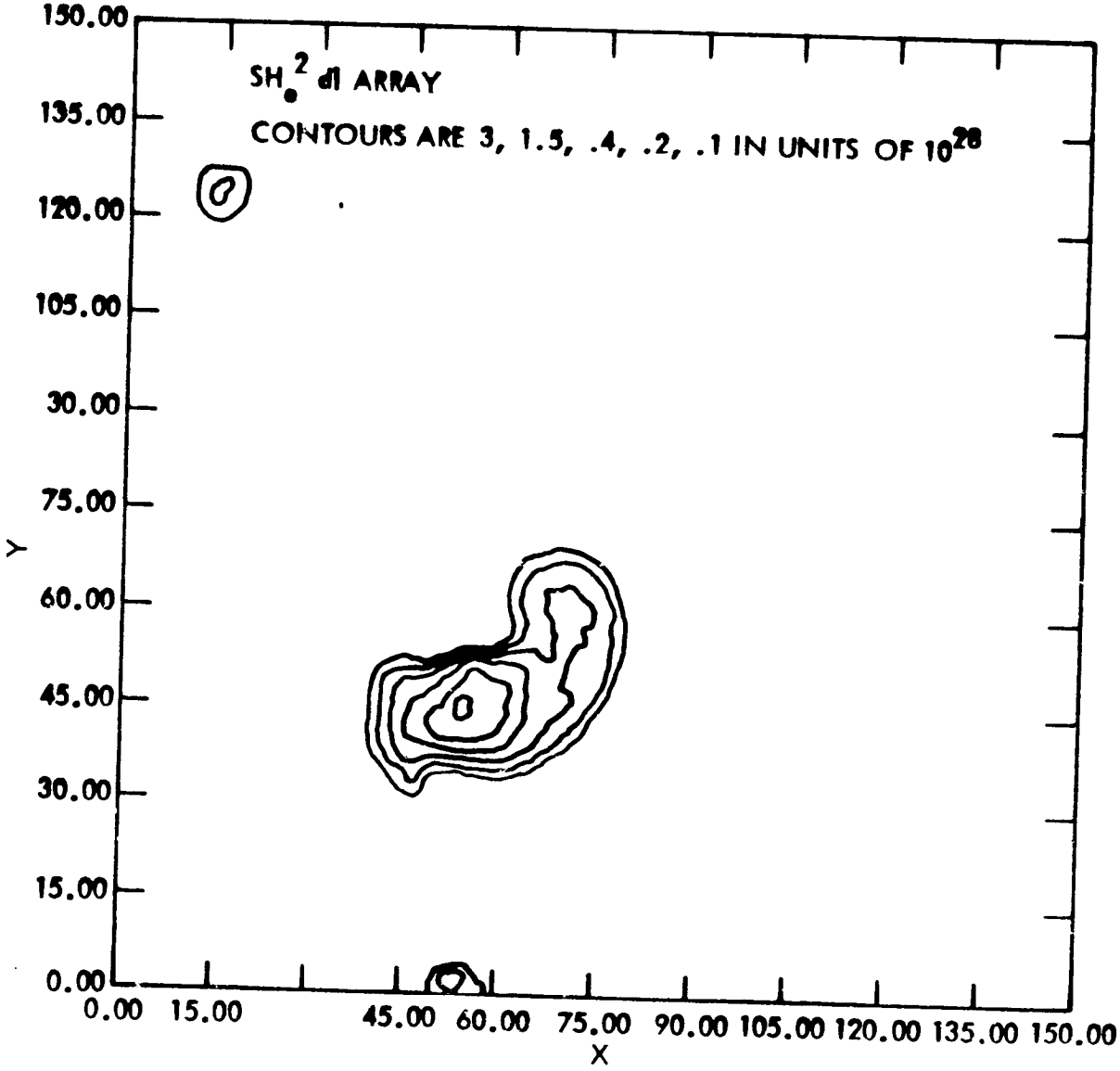

TABLE III

Pointing Position	Observed Emission Measures*		
	X-Ray Spectrometer	EUV X-Ray	S054
McMath 12379-1	1(47)	2(47)	5(46)
McMath 12379-2	2(47)	2(47)	8(46)
McMath 12379-3&4	2(47)	2(47)	3(46)
McMath 12379-5	5(46)	4(46)	6(45)
McMath 12379-6	5(46)	4(46)	6(45)
McMath 12379-7	7(46)	No Fit	8(45)
McMath 12379-8	7(46)	8(46)	3(46)

* NB 1(46) ≡ 1.10^{46}

(d) Analysis of McMath 12664

The philosophy behind this analysis is basically similar to that applied to the 11th June 1973 data. Table IV lists the available data. Again resolving the aspect was the major problem in the analysis.

(i) Aspect Problem.

We used two methods to try to establish the relationship between the rocket's aspect solutions and the images from SO-54 and SO-55.

The pointing positions' coordinates of Aerobee 26.003 were derived as for 26.002. The problem reduced to relating the X-ray filtergram and EUV rasters to these positions.

The first method (Figure 11) we tried utilized the position of the major sunspot in McMath 12664 as a reference point. The SO-54 filtergram had a corresponding white light image that could be pin registered, so that the X-ray data can be directly aligned to the sunspot. SO-55 then could be registered to this using EUV images taken in lines where this feature could be identified (C III) and its known rotational offset.

The second method (Figure 12) involved using the coordinates of the two sunspots as measured by R. Levine from a magnetogram and marking these to scale with the rocket pointing positions on drawing of the solar disk. A fit between the limb and the sunspots were then performed using the SO-54 white light image. Thus, we established the coalignment of the X-ray image and the spectrometer data. The SO-55 raster was aligned as before.

This second method proved to be much more successful. The first method gave an unacceptable discrepancy between the white light limb and the drawing (solid and broken lines) as well as a poor correspondence between the X-ray line intensities as observed by 26.003 and the position of the

TABLE 6

X-Ray Lines from 26.003 (ergs/cm^2/sec/sterad)

Ion Wavelength Factor	O VII (18.63A) $1.410.10^{-2}$	O VIII (16.001A) $1.00.10^{-2}$	Fe XVIII (15.819A) $1.011.10^{-2}$	Fe XVIII (15.608A) $1.025.10^{-2}$	Fe XVII (15.450A) $1.036.10^{-2}$	Fe XVII (15.260A) $1.049.10^{-2}$
Pointing Position						
1	857.2 (156.5)	713.0 (18.0)	61.7 (16.2)	100.5 (9.2)	232.0 (29.0)	1778.5 (122.2)
2	476.5 (101.5)	533.0 (46.0)	41.5 (22.3)	90.2 (20.5)	325.2 (50.8)	1643.8 (59.0)
3	142.4 (39.5)	282.0 (24.0)	32.4 (23.3)	41.0 (11.3)	125.3 (20.7)	726.1 (36.3)
4	90.2 (33.8)	92.0 (23.0)	4.0 (4.0)	24.6 (12.3)	19.7 (4.1)	217.5 (23.8)
5	- (-)	88.0 (33.0)	12.1 (8.0)	17.4 (12.3)	16.6 (16.6)	165.7 (22.8)
6	287.6 (63.4)	181.0 (18.0)	17.2 (16.2)	27.7 (4.1)	63.2 (18.6)	433.0 (15.5)
7	406.1 (111.4)	265.0 (30.0)	24.3 (8.0)	29.7 (24.6)	121.2 (19.7)	195.8 (38.3)
8	267.8 (84.6)	143.0 (11.0)	7.1 (4.0)	20.5 (4.1)	64.2 (12.4)	296.2 (26.9)
9	270.7 (149.4)	94.0 (44-0)	16.2 (4.0)	45.1 (11.3)	11.4 (4.1)	61.1 (8.3)
10	132.5 (29.6)	96.0 (14.0)	22.3 (12.1)	9.2 (4.1)	- (-)	141.9 (12.4)
11	-	93.0 (38.0)	37.4 (12.1)	9.2 (4.1)	54.9 (20.7)	253.8 (25.9)

X-ray emission in the SO-54 filtergrams. We estimate the additional uncertainty introduced by this procedure to be about ± 20 arc seconds.

(ii) EUV and X-ray line intensities.

The collimator functions were then convolved with the EUV pixel intensities at the resulting pointing positions, thus deriving the equivalent EUV line intensities.

Table 6 lists the X-ray line intensities from Aerobee 26.003 which observed McMath 12664. These were to be modelled at HCO by Levine, however, he has found an anomaly between the data sets. Apparently there is a factor of 3-5 excess flux in the X-ray line intensities over the level to be compatible with their EUV lines measurements. This problem could be due to a cross calibration error or a mismatch of the pointing positions. This is not resolvable but the most likely explanation lies in the 30 arc second uncertainty in the relative pointing solutions. Modelling such mismatched data would not be useful. It is interesting to note that the X-ray line intensities from 26.002 seemed low with respect to NRL's data but seem high for the second flight of the same instrument. This implies that either that there is a significant change in the X-ray flux for a relatively small change in the EUV flux or there is a cross calibration problem between SO-82A and SO-55.

GRAPH 1: SUNSPOT ALIGNMENT PROCEDURE (METHOD I)

23 JANUARY 1979

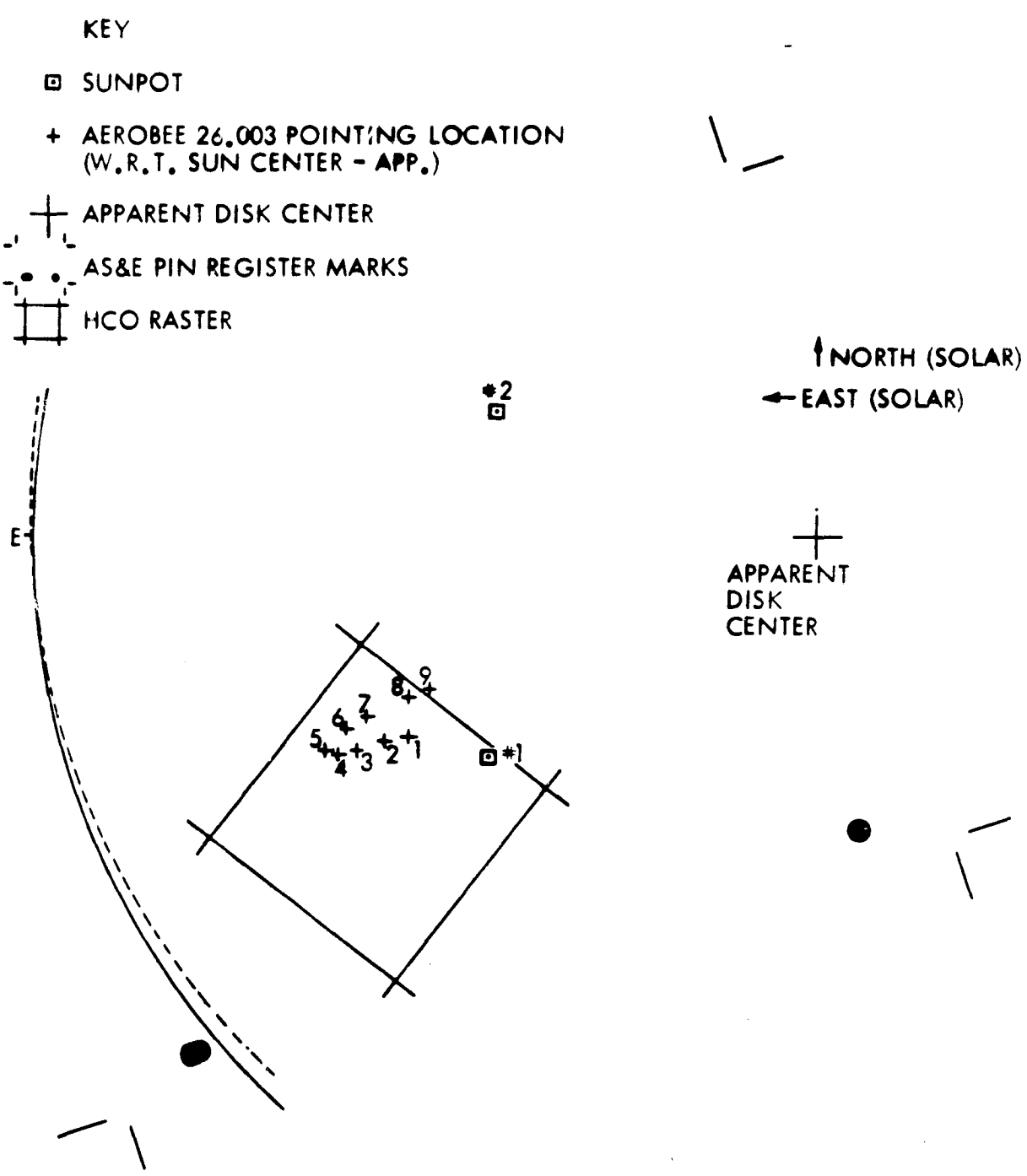

GRAPH 2: AEROBEE 26.003 ASPECT SOLUTIONS (METHOD 2)

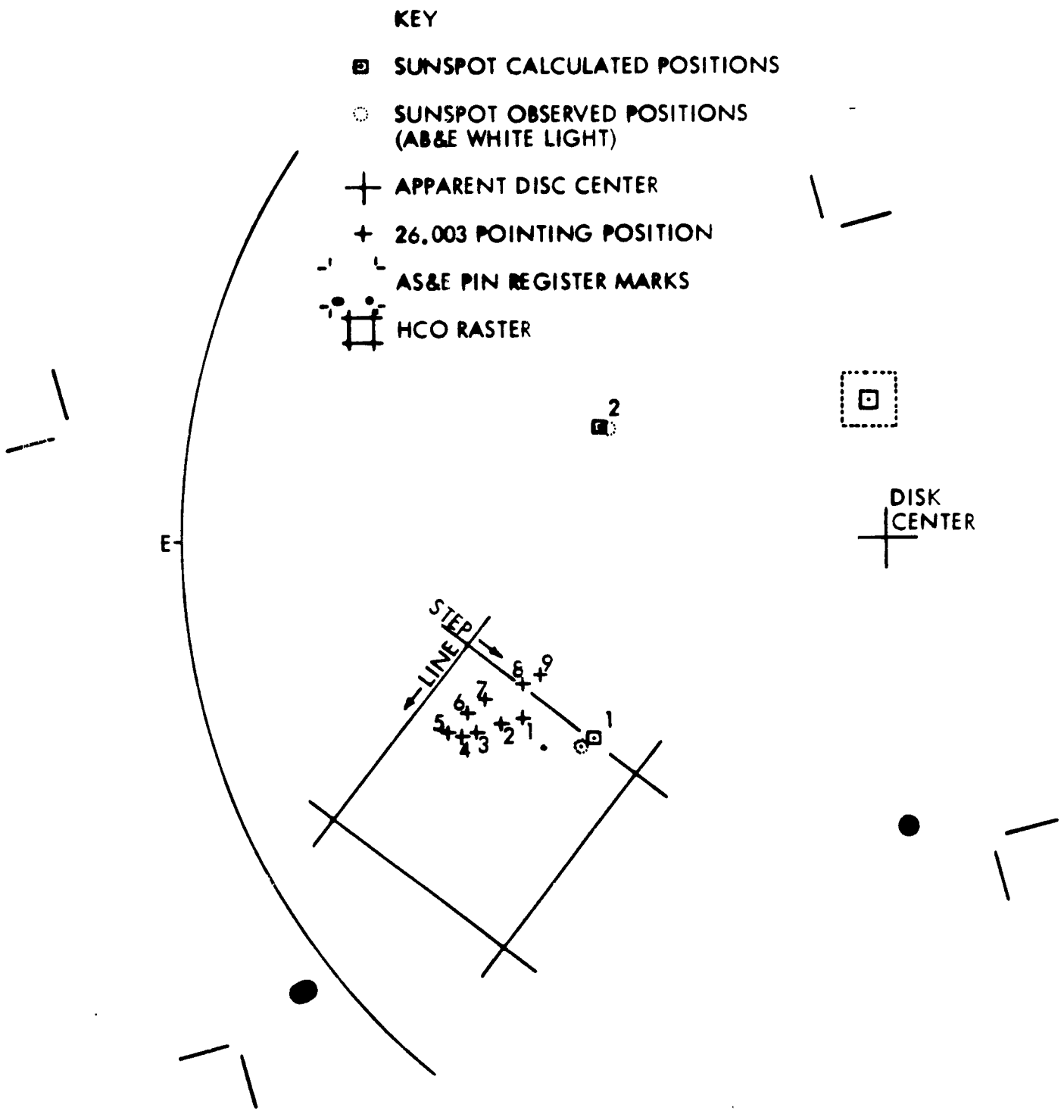

Concluding Remarks

During the course of this research project we have attempted to codify several different data sets to produce models of the emission measure distribution in three active regions. In conducting this investigation we have had to develope methods of equivalencing data from X-ray spectrometers, X-ray filtergrams and EUV images. The primary advantage of adopting this technique is that it extends the temperature coverage of a model beyond that achievable by any single source of data. Where the temperature regimes are duplicated the secondary data may be used to confirm the model, as with the filtergram data (S054 and S056). If there were an anomally then these data could indicate the presence of higher temperature material or a cross calibration error between the experiments.

The models that were produced using SO-82A data with the X-ray line intensities from the sounding rockets demonstrated the feasability of this technique. However, we identified some areas that require further consideration if this type of work is to be attempted in the future, as will inevitably be the case with SMM. They are:-

(i) Instrumental Calibration.

In order to put weight on any intensity measurements from a given experiment, a thorough knowledge of the instrumental sensitivity must be established prior to launch. Uncertainties of 40% generally render the results of differential emission measure modelling to be unusable for accurate physical interpretation. It is possible to establish the interrelation of the ATM instrument calibrations with a complete set of observations on a single stable region by all four instruments (S054, S055, S056, S082A). This has not been

done to our knowledge. Unfortunately the data available at the time of our flights is not complete otherwise this would have been an ideal opportunity to attempt this.

(ii) Coalignment.

As the spatial resolution of Bragg Crystal Spectrometers improves, the ability to reconstruct the alignment of one instrument to another becomes a more important factor in a successful analysis. Hence, a reliable system to reproduce the relative position of a given resolution element (pixel) in one image to that in any other is vital. This was not available to use in this investigation. With our field of view ($\sim$ 35" FWHM) we were able to begin to derive the intensity variations within the regions that were observed. This required accurate knowledge of the relation between the rocket pointing positions and the aspect information for each experiment.

(iii) Atomic Parameters.

This investigation also hilighted the need for a uniform set of atomic parameters such as ionization equilibrium. Often we had to use several different sources of the ionization equilibrium to accomodate all the lines used in the analyses. We generally used Jordan's calculations (1979) but used Davis et al (1977) for Fe. Elemental abundances also are a problem area. In our X-ray data we found the relative abundance of O:Ne to be about 6.0 which is significantly lower than the value adopted usually (Withbroe, 1975). As these observations agree with other recent X-ray investigations (Parkinson 1978; Davis et al., 1975; Acton et al., 1976), yet are very different from the EUV results, this may indicate a real variation in the abundances of one or both of these elements in these two temperature regions of the solar atmosphere or a problem in the interpretation of the data. These aspects of the abundance problem merit a more detailed study, such as will be afforded by SMM.

(iv) Spatially Resolved Data.

It was very useful to have available to us in the data analysis and interpretation phases simultaneous X-ray and EUV imaging information. This is particularly the case in the analysis of the resonance scattering problem where the geometry of the region was important.

As a result of this man-year of research effort, we have produced draft copies of two papers to be submitted, as well as a proposal to study the resonance scattering problem and its implications in detail. We have developed programs to implement the analysis and interpretation of several different data types, which are summarized in Appendix IV.

Acknowledgements

The authors would like to thank all those that aided us on this investigation. Our work with the SO-54 data at the Marshall Space Flight Center in Huntsville, Alabama was assisted by Ed Reichmann and Bill Henze, who helped us correlate the data and did the analysis on IDAPS. At the Naval Research Laboratory in Washington D.C. we were helped by G. Brueckner and Ken Dere. At Harvard College Observatory the data was processed by Randy Levine and George Withbroe who also advised on the differential emission measure modelling techniques. We worked with M. Gerrasimenko on the SO-54 data for McMath 12379, who processed the images and did the reduction of the data to derive intensity, temperature and emission measure contours for this region. Dave Webb and Al Krieger worked on McMath 12664 at American Science and Engineering with us.

We would also like to thank the Lockheed personnel who helped with this project. John Kulander was involved closely with the development and execution of the resonance scattering study, and responsible for developing the theory. Tim Roethig has assisted us with advice on computing and made the HP1000 computer system available to us. Various members of the scientific staff at LPARL have been given useful comments during the course of this project.

Figure Captions

Figure 1: Six typical spectra from the collimated Bragg crystal spectrometers flown on Aerobee 26.002 and 26.003.

Figure 2: Two typical fits of the Lorentzian profiles compared to our data for Fe XVII scans. The raw data are designated by a series of points and the fitted spectra by a solid curve. The numbers indicate the positions of stable fitted lines in each spectrum. In each case 30 prospective lines were chosen arbitrarily to represent the spectra.

Figure 3: Analysis of the O:Ne abundance ratio. The histogram represents the frequency of occurrence of a given line ratio. The family of curves represent the variation of this ratio as a function of electron temperature for various abundance ratios of O:Ne. O:Ne ratio = $6(\pm 0.5)$ most closely reproduces the first peak in the distribution at the measured coronal temperatures. The second peak in the distribution can be explained in terms of a higher relative abundance ratio or a considerably higher temperature.

Figure 4: Representative O VII spectra from each of the four types of regions observed by the two rockets. The Forbidden and Intersystem lines are all drawn the same size thus demonstrating the change in the resonance line flux.

Figure 5: X-ray line intensity maps for the Regions: McMath 12379, 12387 and 12664. The lower temperature lines show less contrast but more extensive emission than the higher temperature lines. They are compared to two intensity maps from SO-56 drawn to the same scale.

Figure 6(a)&(b): Rocket pointing locations with respect to solar disk for both flights.

Figure 6(c): Shows a Stoneyhurst overlay of an SO-54 image used in co-alignment procedure for Aerobee 26.002 (courtesy of MSFC).

Figure 7: Sequence of photographs of (a) McMath 12379 and (b) McMath 12387 in different temperature lines compared to an X-ray filtergram and the pointing locations of the rocket fields of view (courtesy of NRL and MSFC).

Figure 8(a)&(b) Differential emission measure models derived for each field of view where a stable model was found (a) McMath 12379, (b) McMath 12387. The models are calculated by combining the X-ray emission line data from the rocket flight and the EUV image data from SO-82.

Figure 9: Intensity map of McMath 12379 derived from SO-54 filtergram (courtesy of AS&E).

Figure 10: Emission measure map of McMath 12387 derived froma ratioing of two filtergrams from SO-54 (courtesy of AS&E).

Figures 11 & 12: Relative pointing positions of SO-54, SO-55 and the rocket fields of view as derived by two different coalignment techniques.

Appendix 1

Contents

Preprint of a paper on:-

"The Derivation of the Characteristics of Three Solar Active Regions from Observations of Coronal X-Ray Emission Lines".

by: Keith T. Strong
Loren W. Acton

To be submitted to "Solar Physics".

The Derivation of the Characteristics of Three Solar Active Regions from Observations of Coronal X-Ray Emission Lines

by

Keith T. Strong
Loren W. Acton

Lockheed Palo Alto Research Laboratory
3251 Hanover Street
Palo Alto, California 94304

Abstract

Observations of three solar active regions, obtained by rocket borne soft X-ray Bragg crystal spectrometers, are presented. The analytical methods used in the analysis of these data are discussed and the results presented. We determine various parameters which describe the state of coronal plasma at the time of the observations in these active regions. The anomalous behavior of certain line ratios of helium-like ions give strong evidence for resonance scattering (flourescence) of X-radiation in the corona. During this work we have derived the relative abundances of some elements, we describe in some detail the results for the O:Ne abundance ratio.

I. Introduction

The soft X-ray spectral band (1-30Å) of the solar spectrum has a predominance of emission lines that mainly originate from coronal ions in the hydrogen, helium and neon isoelectronic sequences. These emission lines are characteristic of a low density plasma (10^8 - 10^{10} cm^{-3}) maintained at a high temperature (10^6 - 10^7 ^oK). The line intensities originating from these ions contain information on the prevailing physical conditions of the plasma and quantity of emitting material in the observed region.

The work presented here describes a series of observations of various coronal features obtained during two flights of an array of six Bragg Crystal Spectrometers. These instruments monitored most of the prominent emission lines between 9Å and 22.5Å. Data were gathered on three active regions and a region of quiet corona. The field of view of the spectrometers were restricted in order to isolate the emission from a descrete region. The spatial resolution varied from about 35 arc secs to 150 arc sec. full width half maximum (FWHM). The experiment package included an interactive pointing control system which enabled the experimenters to perform raster scans over any regions of interest.

The following sections contain a description of the payloads, the data and the techniques used in the analysis. We have derived the line intensities of all the X-ray emission lines observed in the spectral ranges covered by the spectrometers for each stable pointing position. For reasons of brevity we will only give the mean value of any derived quantity for each distinct coronal region where tabulating the full set of results would not add to the information presented by this work. However, individual results that are especially interesting or anomalous will be discussed as they arise. Where possible, we

have estimated the uncertainties on any derived quantity. We have assumed pesamistic values for effects of possible sources of error during these calculations. Some indication of the conservative values put on these uncertainties is given when we have several measurements of the same quantity, generally the values fall well within the calculated uncertainty. In Section IV we discuss the results of the analysis and their interpretation. In the last section the limitations of our data and its possible uses are discussed.

II. Instrumentation and Observations

The experiment consisted of an array of six scanning Bragg crystal spectrometers and a bent crystal spectrometer (Acton et al.,1976). Each spectrometer monitored a limited wavelength range centered on a selected prominent emission line in the soft X-ray spectrum. The field of view of each spectrometer system was restricted by a two dimensional multigrid mechanical collimator. The ability to limit the field of view, coupled with a SPARCS inflight command link, made it possible to execute raster maps of regions of interest under real-time control of the experimenters.

Table 1 lists the primary characteristics of the payloads for the two flights. On the first flight (Aerobee 26.002) of this payload four of the Bragg Crystal spectrometers had 35 arc second (FWHM) fields of view whereas the other two instruments had 150 arc second fields of view. These instruments with their poorer spatial resolution duplicated two of the higher resolution instruments, and were designed to monitor the active region as a whole. They had better counting statistics, owing to the increased signal levels, than the 35 arc second systems. They were replaced on the second flight (Aerobee 25.003) by instruments that monitored other spectral regions at the higher spatial resolution.

The collimators' fields of view were circular and had a radial sensitivity dependence represented by the function, P(r), given by:

$$P(r) = 2(\phi - r \sin \phi)/\pi, \qquad (1)$$

where r is the fraction of the total radius of the field of view (r_{max} = 1 ≡ 5/4 FWHM). ϕ is the angle who's cosine is r. The collimator transmissions were measured before each flight. The offset of the first side lobes were set to be greater than 32 arc mins from the optical axis to prevent contamination of the data from other active region emission.

The diffraction crystals were KAP for all the spectromters, except the Mg XI system flown on Aerobee 25.003, which used ADP. The crystals were mounted on platforms that were scanned smoothly and continuously through an angular range of about 3° on a motor-driven cam. The crsytals were offset with respect to one another to access the appropriate angular (wavelength) ranges. They were grouped in two sets of three, each set with an independent drive system and shaft encoder. The encoder divided each scan cycle into 512 angular bins. A scan over the total spectral range was completed for both the increasing and decreasing wavelength directions in about 14 seconds. The integrated reflectivity of the crystals were determined from measurements made by R.L. Blake and A.R. Burek.

The proportional counter detectors were filled with an argon-methane mixture at a pressure of 1 atm. The polypropylene windows were carbon coated and were 1 μm thick. The number of events registered by the proportional counters were accumulated in registers before being transmitted to the ground system on the P.C.M. telemetry. The registers were scanned at a rate of 256 Hz.

The SPARCS inflight-command link was used by the experimenters to set and maintain the rockets' pointing with respect to the solar regions of interest. A diffraction pattern, produced by special grids in the collimator stack, was superimposed on a hydrogen-alpha solar image produced by a telescope/filter system. One of the spots of the pattern was designed to correspond to the optical axis of the collimation system. The image was fed into a television camera and transmitted to the control center to aid the real-time control of the pointing position. The image was also recorded by a 16 mm film camera in the experiment package for post flight analysis.

A brief description of the experiment has also beein given by Acton and Catura (1976). Table II details the observations made by the instruments. Most of the observations were coordinated with the ATM experiments. Figures 1(a) - (f) show typical examples of the spectra obtained by these experiments.

III. Analysis

At every stable pointing position the data accumulated by each of the six spectrometers consisted of a pair of spectra, scanned in the forward (decreasing wavelength) and reverse directions. A spectrum consisted the number of events recorded at each crystal encoder position. Due to non linearities in the crystal drive cams the count rates had to be normalized over the observation time of that position. In order to interpret these spectra, the X-ray lines recorded in the data have to be identified and their intensities derived for each field of view. These results then have to be coordinated with the aspect information and any data gathered simultaneously on the same regions by other instruments.

The spectral regions, observed by these instruments, have been extensively monitored by previous experiments (Parkinson, 1975; Acton et al., 1976). Hence, the wavelength of the prominent lines are familiar to us. The data were of sufficient quality to be able to resolve many of these lines. All the spectra were analyzed by fitting the following expression for the number of events (N) in an encoder bin (i) over the complete spectrum.

$$N_i = B + \sum_{n=1}^{n=L} \frac{An}{1 + A_n^2} \quad \text{cts/sec/encoder bins,} \tag{2}$$

where B is the background count rate in each data bin, which is assumed to be constant over the whole spectrum. L is the total number of lines present in the spectrum. A_n is the peak amplitude of the nth line and S_n is given by:

$$w_n S_n = (X_n - X_i) . \tag{3}$$

where w_n is the full width at half maximum of the nth line and X_n is its position. X_i is the position of the ith encoder bin. X_i, X_n and w_n are expressed in the same units (λ, i). The line profile expressed in Equation 2 takes the form of a Lorentzian, which we found to be an acceptable approximation to the observed line profile, which in reality is a convolution of the natural doppler profile, the collimator function (Equation 1) and the crystal rocking curve. The amplitude, position and half width of each line, as well as the background, were free parameters in the least squares fitting calculation. There were consequently a maximum of 3n + 1 parameters in the fit.

As mentioned above, the positions of the brighter lines are well established in these spectral regions, also the characteristics of the flight crystals were well knonw. Hence, the derived positions of the lines and their half widths could be compared with these established results. The agreement was, generally, very good, giving us some confidence as to the integrity of the analysis procedure. Where fainter lines were blended but their positions are known from other observations made at higher spectral resolution, we could just fit for the line amplitudes using a half width derived from the surrounding lines for the blends.

The total number of counts observed in each X-ray emission line in unit time was derived by integrating over the fitted profile. This can be done analytically, resulting in:-

$$c_n = \pi A_n w_n \tag{4}$$

where c_n is the integrated count rate. We averaged the results from the forward and reverse scans of a given spectral scan for each pointing position at this stage. Where there was a large descrepancy in peak counting rate, line width or wavelength between the forward and reverse scans the data were considered to be invalid. These are elliminated lines that were miss matched or merely noise spikes. The uncertainties derived from the standard deviations on the fitted parameters were added quadratically. The total photon flux (Φ) could then be derived from the efficiencies of the instruments components:

$$\Phi = \frac{c_n}{A_{eff} R_c \varepsilon_\eta} \quad \text{photons/cm}^2\text{/sec} \tag{5}$$

where ω is the average crystal scan rate (rads/sec) and R_c is the integrated reflectivity of the crystal (rads/sec). η is the collimator transmission, and ε is the quantum efficiency of the proportional counters. The effective area of the instrument (A_{eff}) is derived from the geometrical characteristics of the individual instruments. These were determined by measurement and expressed by the empiricle relation:

$$A_{eff} = \left\{ C_1 + C_2 (\lambda_n - C_3) \right\} \sin (2\theta_n) \text{ cm}^2, \qquad (6)$$

where the C's are constants, deduced from the preflight calibrations, θ_n is the Bragg angle of the line and λ_n is the wavelength of the line.

Initially, the fitting was applied to spectra that were summed over each active region. Thus, we were able to establish the mean positions, widths and intensity of the lines to use as first approximations for fits to the brighter lines in the individual spectra. The intensity of all lines identifiable in the spectra from each stable pointing position were analyzed as described above. This technique makes it possible to analyze a spectrum as a whole, taking into account contributions to the background of the wings of all lines in the spectrum. Failure to do this will lead to an over-estimation of the background signal, and consequently an underestimation of the line intensity. For example, by fitting a triangular profile to a line giving it the same FWHM can lead to a possible 30% under estimation of the integrated line intensity, from neglecting the wings of the line, assuming the background is perfectly determined.

IV. Results

(a) Emission Line Intensities

There were a total of 31 stable pointing locations from the two flights. Each location yielded a total of 12 spectra. Using the above techniques we positively identified 58 emission features in the 9 - 23Å band of these spectra. Table III lists the wavelength and possible identification of these features. The wavelengths derived from each flight are listed separately,with the estimated uncertainty in parenthises, and a weight mean from these values calculated. These are compared to the results from other observational and theoretical investigations. Generally the agreement is very good.

The volume of results from the spectral fitting of the data from the two flights preclude their inclusion in this work. However, the mean intensities of the lines are listed in Table IV for each of the three active regions and the quiet coronal region for the high and low spatial resolution data. The values in parentheses are the factors between the brightest and faintest lines recorded for that region. Upper limits on the intensities are put on lines where no fit was obtained.

These data show the contrast between the quiet corona and active region spectra. In the "cooler" lines, such as O VII, the quiet corona registers a significant signal, although it is a factor of 6 to 10 weaker than the corresponding active region spectra. However, all other lines formed at higher temperatures show little evidence of emission from the quiet corona, within the sensitivity range of this experiment. Also the contrast between the various active regions is evident from these data. In all lines,McMath 12664 is the brightest region by a factor of about 3 to 5 over McMath 12379 and McMath 12387 which were of comparable brightness.

The brightness factor results demonstrate the advantages of having higher spatial resolution available in such an experimental package. The 150' arc second FWHM field of view instruments all gave brightness factors of between 1 to 4, indicating that the instruments were incapable of giving any useful information about the structure within an active region. However, the higher resolution data gave brightness factors of between 5 and 30. Thus it is possible to use these data to produce intensity maps of X-ray regions observed. The results of the mapping procedure can be seen in Figure 2 for the three active regions observed. Each stable pointing position is assigned a square with a side of twice FWHM. These are shaded in accordance with the relative brightness of the primary lines observed by the flights (O VII - 21.6; O VIII - 18.95; Fe XVII - 15.01; Ne IX - 13.44; Ne X - 12.13; Mg XI - 9.17). The position with brightest intensity of any given line was assigned 10[illegible] all other brightnesses were blocked into 5 groups in relation to the brightest position. The resulting maps are compared to an intensity contour plot from the S054 instrument on ATM (Gerassimanko, 1978) for two of the regions. The results correspond very well. One interesting feature of these plots is that the contrast between the "cooler" lines (O VII and O VIII) is less than those of the other lines, the emission from which seems to be more localized.

(b) Resonance Line Ratios

The intensity of an X-ray emission line can be expressed in the form (Pottash, 1964):

$$E = D\, g\, f\, A\, \lambda \int G(T)\, N_e^2\, dV, \qquad (7)$$

where E is the line intensity (photo. .'cm^2/sec/st) at the Earth. D is a constant, g is the Gaunt factor and f is the oscillator strength. A is the elemental abundance and λ is the wavelength (Å). N_e is the electron density and the temperature function, G(T), is given by:

$$G(T) = T^{1/2}\ 10^{-(\frac{5040\ W}{T})}\ N_i, \qquad (8)$$

where N_i is the number density of the ion stage responsible for the transition at the temperature, T. W is the excitation energy of the transition.

For any given transition equation (7) may be rewritten, assuming that the emission can be characterised by an isothermal plasma (T_{eff}) and a suitable emission measure $N_e{}^2V$,

$$E_1 = D\ f_1\ g\ A_1\ \lambda_1\ G_1\ (T_{eff})\ [N_e{}^2\ V]\ \text{photon/cm}^2\text{/sec/st} \qquad (9)$$

Although using this expression directly with a measured line intensity can yield information on the coronal plasma, such as its effective temperature or emission measure, the results are subject to uncertainties in the data. By ratioing line intensities such uncertainties can be minimized if care is taken in the choice of the lines. Hense the ratio of any two lines can be given by:

$$\frac{E_1}{E_2} = \frac{f_1}{f_2} \cdot \frac{A_1}{A_2} \cdot \frac{\lambda_1}{\lambda_2} \cdot \frac{N_1}{N_2} \cdot 10^{-(\frac{5040(W_1-W_2)}{T_{eff}})} \qquad (10)$$

It is evident that by choosing lines carefully some of these factors will be eliminated. Further, if the lines are observed by the same instrument

then the ratio will be free from calibration and instrumental uncertainties. For example, choosing lines produced by the same ion will give a ratio that is mainly dependent on the relative oscillator strengths. Table I lists oscillator strengths derived in this fashion. Similarly, it is possible to derive reliable relative abundances by choosing lines with similar temperature functions, and assuming their oscillator strengths (Acton and Catura, 1975; Parkinson, 1977). We investigated the relative abundances of Mg to Fe and Ne to Mg in this manner.

The Mg:Fe ratio utilized the Mg XI line at 9.17A and Fe XVII line at 15.009Å. The relative abundance ratio was found to be 0.71($\pm$ 0.15) from the observations of McMath 12664. This compares with values of 0.6 (Potash, 1967), 0.97 (Parkinson, 1977) and 1.2 (Withbroe, 1971). The relative abundance of Ne to Mg was determined using the Mg XI line at 9.17Å and the Ne X line at 12.134Å. It was found to be 1.6 ($\pm$ 0.8) also from the observations of McMath 12664. This value compares with 1.2 (Pottash, 1967), and 0.07 (Parkinson, 1977) and 0.85 (Withbroe, 1971).

The relative abundance of O to Ne has been the subject of several previous investigations. Its value seems to differ depending on the origin of the data. EUV data tend to give a high value for the O:Ne ratio, for example, Withbroe (1971) gives the ratio to be 15.8. However, soft X-ray emission line data generally give lower values. Acton et al. (1975) have calculated a value of 4.7, Parkinson (1977) gave a value of 6.6. We use the same technique as Acton et al. (1975), which utilizes the intensity ratio of the O VIII line (18.95Å) to the Ne IX line (13.445). Figure 3 shows the frequency distribution of the O VIII:Ne IX line intensity ratio from the three active regions observed by the rocket experiments. The ratio was calculated

with its uncertainty for each stable pointing position. Each value was then considered to be a normal distribution with a width equal to the calculated uncertainty and an integral value of unity. These were then summed to produce the frequency distribution. This ensured that any ratios with a large uncertainty had a minimal effect on the results. Plotted above the resulting histogram are a series of curves that represent the temperature dependence of the O:Ne ratio calculated for several values of this ratio.

The observed frequency distribution has a distinctly dual population. The first with a maximum at a ratio of about 7.5 and the second at about 15. The second peak is mainly due to results from the brightest fields of view of McMath 12664.

The effective temperatures of the regions were determined using line ratios of adjacent ionization stages of several elements. The results are shown in Table V. The particular O VII:O VIII ratio used was chosen as the data were derived from the same instrument, as was the Fe XVII:Fe XVIII ratio. Although the O VII resonance line at 21.602A is brighter and would give a statistically more reliable result, there is some evidence for a change of the resonance line intensity due to scattering so it was not used in this calculation. The evidence for resonance scattering discussed in a subsequent section. The effective temperatures determined from the line ratioing technique all lie in the $2.9 - 3.9.10^6$ ^oK range. Using these temperatures and the main peak of the frequency distribution, we derive an O:Ne abundance ratio of $6.0(\pm 0.5)$. This is consistent with Parkinson's determination (1977).

The second peak in the ratio frequency distribution would indicate a relative abundance of $12(\pm 2)$, which is more in agreement with the EUV

results, assuming the same temperature ranges. However, it is possible that we observed some of the flare associated plasma, hence an abundance ratio of 6.0 would be obtained by a temperature of approximately 9.10^6 ^oK. Non uniform abunadnaces throughout the solar atmosphere would be a difficult problem to explain and model. A further point of interest in this regard arises from the McMath 12387 data, where the brightest field of view gave a value of 2.5 for the O:Ne line ratio, being responsible for most of the power in the frequency distribution below 4. This result cannot be lightly discounted, as it is not explainable with an abundance ratio of greater than 4 at any temperature, and statistically significant.

(c) He-like Ion Line Ratios

There are two line ratios that are of particular interest in the data from the He-like ionizatien stages. Adopting the nomenclature of Gabriel and Jordon (1969), R is defined as the ratio of the Forbidden line ($1s^2\ ^1S$ - $1s2s\ ^3S$) to the Intersystem line ($1s^2\ ^1S$ - $1s2p\ ^3P$). This ratio is sensitive to electron density above a threshold of 6.10^9 cm^{-3} (Freeman et al., 1971) due to the possibility of a transition between the ^3P and ^3S levels. The possible temperature dependence of R has been investigated by several groups (Acton et al., 1972; Blumenthal et al., 1972; Gabriel and Jordon, 1973). We are unable to determine the nature of any temperature dependence from these data within the experimental uncertainties.Hence, the ratio is not strongly temperature dependent which favours the views of Gabriel and Jordon (1973). The density for all our regions lies near or below the threshold value of 6.10^9 cm^{-3}.

The second ratio is designated as G and defined as the sum of the intensities of the Forbidden and Intersystem lines divided by the intensity of the resonance line ($1s^2\ ^1S$ - $1s2p\ ^1P$). This ratio is independent of electron density as it contains the sum of the forbidden triplet transitions. The temperature dependence of the ratio has been studied by Acton and Brown (1978), and Mewe et al. (1977a,b).

The results for all the observed Helium-like ions are listed in Table VI for each region and spatial resolution. The G ratio shows an interesting variation over different regions for O VII. These variations are significant with respect to the experimental uncertainties. The quiet corona gives the lowest value of G. From the theoretical calculations of Acton et al (1978) and Mewe et al. (1977) this trend is contrary to that anticipated from a low temperature region ($\leq 2.10^6\ ^oK$) such as the quiet corona. Further, the active region results show significant variations that cannot be due to temperature differences alone. There is no evidence in the data for a significant departure from equalibrium conditions in the plasma that could explain the discrepancies between the calculated value of G (~ 0.8) and the observed values. There is also an indication of a systematic difference between the results from the two different spatial resolutions from any given region. None of the other He-like ions show similar variations.

We believe these effects are caused by resonance scattering of O VII in the corona. Recent work by Acton (1978) show that resonance scattering is a viable mechanism in the corona. The most susceptable ion is to this effect at normal coronal temperatures ($\leq 3.10^6$) is O VII. The variations observed in the G ratio listed in this work could be accounted for by an enhancement or a reduction in the resonance line intensity due to scattering

(Strong, 1978; Strong and Kulander, 1979). The forbidden triplet transition will remain unaffected by scattering effects. Hence, G will be increased by a net absorption of resonance line radiation along the line of sight, such as was observed in the three active regions, or will be decreased by an enhancement due to scattering into the line of sight as observed in the quiet coronal observations.

(d) Modelling of the Active Region Plasma

The X-ray line intensities may be used to derive differential emission measure models of the plasma in the observed regions. The resonance lines of fine ions were used in the modelling from the 35 arc sec FWHM fields of view, the parameters are listed in Table VII. The modelling of the differential emission measure involves the use of absolute line intensities. These are subject to statistical fluctuations in the observed count rates, which can be quantified, and also to errors in the relative instrumental calibrations. Any atomic parameters used in such a calculation are also subject to errors. Every effort was made to minimize the relative preflight calibration errors in the spectrometers, however, some residual differences will remain when comparing the fluxes observed by different detection systems. The most important factor is the uncertainties introduced by the atomic data, such as the elemental abundances, oscillator strengths and ionization balance. While we used the best atomic data available, there still remains the possibility of introducing errors into the calculation from this source.

The modelling techniques used in this investigation was first described by Withbroe (1975). This method compares the intensity of a number of emission lines as calculated from a differential emission measure model

with the observed intensities. The discrepancy between them is used to, suitably weighted by its emission function, to adjust the model. The procedure is repeated until the model has converged to give the observed line intensities. The ability of this method to resolve structure in the differential emission measure model is dependent on the widths of the temperature functions and their relative positions in the temperature domain. Figure 4 shows the temperature functions of the five lines used in the investigation. The temperature functions of X-ray emission lines are generally quite broad, and are consequently, incapable of defining small or narrow features in the derived differential emission measure function.

The speed of convergence is dependent on the number of lines used in the modelling procedure, the amount of overlap between their emission functions and the internal consistency of the data. Although many lines were available to us in the analysis, many of them would be redundant and slow the convergence. Convergence was achieved, on average, in about 50 iterations. The convergence was stable, and could be taken to several hundred iterations without significant change. As mentioned above the O VII line, which was the most sensitive to lower temperature material, was corrected for resonance scattering effects. Failure to do this led to an unstable result. The O VIII line may also be subject to this effect, to a lesser extent, but was not corrected.

Table VIII lists the results of the modelling. Generally, the models could be characterized by a single peaked function. The table gives the temperature of the peak of the modelled distribution and the i/e width. The integral of the differential emission measure is calculated. The iteration procedure was terminated when all the line intensities lay within their

calculated uncertainty and no significant (< 1%) change occurred in the model over successive iterations. The ratio of the predicted to observed intensity was also calculated (the fitting ratio).

The models indicate a mean value for the temperature of the regions similar to those derived from the line ratio technique described above. The brightness of the active regions does not seem to depend heavily on the effective temperature but more on the total emission measure. Hence, it would seem that the density and extent of the active regions determines the X-ray emission rather than their temperature. The O VII predicted line intensity seems to be consistently low compared to O VIII line intensity. This could be due to resonance scattering effects in O VIII that were not taken into account of the calculations or a further discrepency in the O:Ne abundance ratio.

Generally, the data fitted to within 10-40% of the absolute line intensity. This is quite good considering the inherent problems in assigning an absolute line intensity as mentioned above.

V. Concluding Remarks

In this presentation we have described the reduction and analysis of the data accumulated during two flights of an instrument consisting of an array of six Bragg crystal spectrometers. This payload gathered spectra in the soft X-ray wavelength band (9-22Å) from three active regions and an area of quiet corona. We have described a technique to reduce these data to line intensities that give a reliable result. We then demonstrate the variety of information that can be derived from such results while indicating their limitations and uncertainties.

We find that the spectra should be fitted as a single entity, and not treated as a series of individual line profiles. For our instruments, with their relatively small solid angle fields of view and RAP crystals, we determine that a Lorentzian profile adequately fits the data. By fitting all the lines in a single spectrum simultaneously using a representative profile with an itterative least squares technique, we find that we get a more accurate determination of the background level (comprised of instrumental noise, X-ray continuum,and cosmic ray events). Thus, avoiding an overestimate of the background due to contributions from the wings of surrounding line profiles, and a consequent under estimate of the integrated line intensity. Errors can arise of over 10% by considering the background level to be determined by a portion of a spectrum "sufficiently far from the line" - < 7 FWHM's from the line center. Often there are no parts of the X-ray spectrum sufficiently devoid of lines, resolved or unresolved.

An important result is the variation in the G ratio of O VII. We are able to show that these variations are significant with respect to the uncertainties in the data. We can not interpret the observed ratios in terms of temperture

variations from one region to another as the trend is contrary to that predicted by recent theoretical studies (Acton & Brown, 1978; Mewe and Shrivjer, 1977a, b). Nor is non-equalibrium conditions in these regions a likely explanation as it firstly requires that the quiet corona is in a continual ionising state over a large area to account for its low G ratio, and that at all 26 stable pointing locations in the three active regions there was a predominence of recombining plasma in the field of view. This would be an unlikely occurence. Also, none of the other He-like ions show similar variations, within the limitations of experimental uncertainties. We find that the data is interpreted most convincingly in terms of resonance scattering (flourescence) in the coronal plasma. These data have been investigated in detail as a result of this work (Strong, 1978; Acton, 1978; Strong and Kulander, 1979). This phenomenon could be utilized to study the plasma in more detail than has been possible previously as scattering effects can give us information on the density, and distribution of the coronal material. It should also be possible to detect the polarization of X-radiation if these conclusions are correct.

We have determined the wavelengths of the prominent lines observed by these instruments, and proposed possible identification for them. In taking the line intensity ratio of several lines we have determined several relative oscilator strengths and abundances. One particularly interesing result of this work is the relative abundance of O:Ne. This statistical study gives a relative abundance ratio of 6.0($\pm$0.5) for active region temperatures. However, there are indications of both significantly higher and lower values of the ratio from different regions. The value of 12($\pm$2) obtained from the brighter regions of McMath 12664 can be interpreted alternatively in terms of a higher temperature plasma being observed whilst maintaining the lower abundance

ratio. There is some support for this view as some flaring activity was observed in this region just prior to the observations. However, it is difficult to explain the lower value obtained from the brightest field of view of McMath 12387. The possibility of an anomalous distribution of O and Ne can be resolved by a further study of this problem by the XRP instrument on SMM.

We derive differential emission measure models of the coronal plasma in these active regions using a technique pioneered by Withbroe (1975). We find that, for the most part, the emission measure distributions as indicated by the analysis can be represented by a single isothermal peak. This is indicative of the poor temperature range and resolution of the lines available to us in these data. The X-ray data is capable of representing the emission from the hot active region plasma, and indicates a uniformity of temperature throughout a region. This would be an expected result due to the high conduction of the coronal plasma. However, these data can give us little information on the lower temperature material at the base of these active region loops. This indicates the need of coordinating this type of data with EUV observations of the lower corona and transition region. This will be the subject of a future study.

The type of data derived from soft X-ray emission line spectra are subject to many types of uncertainty, it is important to understand these in order to be able to know how to interpret these data reliably. The derived line intensity is subject to statistical limitations on the observed count rates. Also the preflight calibration of all the instrumental efficiencies is very important. An accurate knowledge of these makes it possible to calculate absolute line intensities of between 25% and 40% uncertainty with these data. Assigning identifications to the spectral emission features is only a problem

for faint or blended lines, as most of the positions of the prominent lines are well known and it is possible to derive the wavelength of the lines to an accuracy of $\leq 0.005\text{Å}$ in general.

The interpretation of these data requires the use of parameters such as abundances, ionization equalibrium calculations and various atomic parameters, all of which can introduce uncertainties into the calculations. We show that by using the technique of line ratioing it is possible to minimize the effect of instrumental calibration errors, and uncertainties in the atomic parameters, while still being able to derive useful characteristics of the particular ionization stage or the plasma that produced the emission. Consequently, in spite of the above difficulties, it is possible to derive new and interesting results from this type of X-ray data.

Acknowledgements

We would like to express our thanks to R.C. Catura, C.J. Wolfson, D.T. Roethig, and J.L. Culhane for some constructive suggestions during the course of this project. We also wish to thank M. Gerassimenko, K. Dere and E. Reichmann for supplying the supporting data from the A.T.M. instruments. This work was supported in part by the National Aeronautics and Space Administration through contract NAS8-33195. This work was completed during the Skylab Solar Workshop Series on Active Regions sponsored by NASA and NSF. The workshops were managed by the High Altitude Observatory, Boulder, Colorado. Strong also acknowledges the support of the Mullard Space Science Laboratory during the initial phases of this study.

References

Acton, L.W. 1978, Ap.J., 225, 1069.

Acton, L.W., Catura, R.C., Meyerott, A.J., Wolfson, C.J. and Culhane, J.L., 1972, Solar Phys., 26, 183.

Acton, L.W., Catura, R.C., and Joki, E.G., 1975, Ap.J., 195, L93.

Acton, L.W. and Catura, R.C. 1976, Sp.Sc. Inst., 2, 445.

Acton, L.W. and Brown, W.A. 1978, Ap.J., 225, 1065.

Allen, C.W., "Astrophysical Quantities", Third Edition, 1973.

Beigman, I.L., and Vainshtein, L.A. 1971, Soviet Astr. -AJ, 14, 825.

Bhalla, C.P., Gabriel, A.H., and Presnyakov, L.P. 1975, M.N.R.A.S., 172, 354.

Blumenthal, G.R., Drake, G.W.F. and Tucker, W.H. 1972, Ap.J., 172, 205.

Davis, J.M., Gerassimenko, M., Krieger, A.S., and Vaiana, G.S. 1975, Solar Phys. 45, 393.

Freeman, F.F., Gabriel, A.H., Jones, B.B., and Jordan, C. 1971, Phil. Trans. Roy. Soc. Lond. Series A, 270, 127.

Gabriel, A.H., 1972, M.N.R.A.S. 160, 99.

Gabriel, A.H. and Jordan, C. 1969, M.N.R.A.S. 145, 241.

Gabriel, A.H., and Jordan, C. 1972, "Case Studies in Atomic Collision Physics-II", eds. McDaniel and McDowell, North-Holland.

Gabriel. A.H., and Jordan, C. 1973, Ap.J. 186, 327.

Jacobs,

Jordan, C. 1969, M.N.R.A.S., 142, 4, 501.

Jordan, C. 1970 M.N.R.A.S., 148, 1, 17.

Malenousky, M., and Heroux, L. 1973, Ap.J., 181, 1009.

Mewe, R., and Schrijver, J. 1978a, Astr. Ap.

Mewe, R., and Schrijver, J. 1978b, Astr. Ap.

Neupert, W.M., Swartz, M., and Kastner, S.O. 1973, Solar Phys., 31, 171.

Parkinson, J.H. 1971, Thesis, University of Leicester.

Parkinson, J.H. 1975, Solar Phys., 42, 183.

Pottasch, S.R. 1964, Space Sci. Rev. 3, 816.

Pottasch, S.R. 1967, Bull. Astron. Soc. Neth. 19, 113.

Pye, J.P., Evans, K.D., Hutcheon, R.J., Gerussimenko, M., Davis, J.M., Krieger, A.S. and Vesecky, J.F., 1977, Astr. Ap.

Strong, K.T. 1978, Thesis, University of London.

Walker, A.B.C., Jr., Rugge, H.R., and Weiss, K. 1974, Ap.J. 192, 169.

Withbroe, G.L., 1971, NBS Special Pub., No. 353, 127.

Withbroe, G.L., 1975, Solar Phys. 45, 301.

Table I. Primary Characteristics of the Instruments.

Ion	O VII	O VII	O VIII	Fe XVII	Fe XVII	Ne IX
(1) Aerobee 26.002						
Wavelength range (A)	21.4-22.3	21.4-22.3	18.3-19.4	14.9-16.1	14.9-16.1	13.3-14.6
Field of view (FWHM)	149"	34"	34"	148"	33"	31"
Collimator Transmission (η)	0.32	0.19	0.20	0.31	0.19	0.18
Geometric constants (C_1)	17.4	17.2	15.8	16.1	14.8	14.7
(Eq. (7)) (C_2)	2.4	2.4	2.0	1.3	1.2	0.63
(C_3)	21.252	21.252	18.20	14.894	14.894	13.318
Crystal Integrated Reflectivity (R_c)	$5.3.10^{-5}$	$5.3.10^{-5}$	$5.0.10^{-5}$	$6.1.10^{-5}$	$6.1.10^{-5}$	$6.6.10^{-5}$
Counter efficiency (E)	0.18	0.17	0.26	0.37	0.38	0.40
(2) Aerobee 26.003	O VII	O VIII	Fe XVII	Ne IX	Ne X	Mg XI
Wavelength range (A)	21.4-22.3	18.3-19.4	14.9-16.1	13.3-14.6	11.4-12.8	9.09-9.39
Field of view (FWHM)	36"	32"	41"	40"	39"	35"
Collimator Transmission	0.12	0.09	0.14	0.15	0.14	0.11
Geometric Constant (C_1)	18.7	15.8	14.8	14.7	15.7	20.30
(C_2)	2.6	2.0	1.2	0.66	.73	-7.3
(C_3)	21.427	18.329	14.888	13.313	11.496	9.10
Crystal Integrated Reflectivity	$5.3.10^{-5}$	$5.0.10^{-5}$	$6.1.10^{-5}$	$6.6.10^{-5}$	$7.1.10^{-5}$	$8.9.10^{-5}$ (ADP)
Counter Efficiency	0.15	0.27	0.35	0.38	0.36	0.47

TABLE II. Observations

Flight	Launch	Observed Region	Central Position (arc secs N&E)		ATM Coordinates	
Aerobee 26.002	18:30 GMT, 11 June 1973 Altitude 220 km total Observation time = 300s.	Quiet Corona	95, 67	3 data sets obtained	S084A	WRL
		McMath 12379	260, 220	Quiescent Active Region - 9 data sets obtained	S084A S056 S056	NRL MSFC ASE
		McMath 12387	335, 880	Active region on E. White - 8 data sets obtained.	S084A S055 S054 S056	NRL HCO ASE MSFC
Aerobee 26.003	22.07 GMT, 19 Dec. 1973 Altitude 220 km 180 sec of observations.	McMath 12664	-230, 515	Post Flaring Active Region - 11 data sets obtained.	S054 S055	ASE HCO

TABLE III: Emission Line Identifications and Wavelengths

Line #	Possible Identification: Ion	Possible Identification: Transition	Measured Wavelength (A): λ_1	Measured Wavelength (A): λ_2	Measured Wavelength (A): $\bar{\lambda}$	Published λ(A)	Reference	Oscillator Strength (observed)
1	Mg XI	$1s^2\ ^1S_o$ - $1s2p\ ^1P_1$	-	9.173(3)	9.173	9.169,9.18	a,b	0.75*
2	Mg XI	$1s^2\ ^1S_o$ - $1s2p\ ^3P_1$	-	9.235(5)	9.235	9.232,9.22	a,b	0.24(0.06)
3	Mg XI	$1s^2\ ^1S_o$ - $1s2s\ ^3S_o$	-	9.318(3)	9.318	9.315,9.32	a,b	0.59(0.08)
4	Ne IX	$1s^2\ ^1S_o$ - $1s3p\ ^1P_1$	-	11.548(2)	11.548	11.549	a	0.16(0.03)
5	-		-	11.596(5)	11.596	11.600	a	
6	Fe XXII		-	11.760(16)	11.760	11.76	b	
7	Fe XXII	$1s^22s^22p^2\ ^2P_{3/2}$ - $2p3d\ ^2D_{3/2}$	-	11.908(11)	11.908	11.92	b	
8	Ne X	$1s^2\ S_{1/2}$ - $1s2p\ ^2P_{1/2,2/3}$	-	12.134(3)	12.134	12.137,12.13	a,b	
9	Fe XVII	$1s^22s^22p^6\ ^1S_o$ - $2p^54d\ ^3D_1$	-	12.260(3)	12.260	12.264,12.262	a,c	0.28(.03)
10	Fe XVII	$1s^22s^22p^6\ ^1S_o$ - $2p^54d\ ^3P_1$	-	12.319(5)	12.319	12.320	c	
11	Fe XVII	$1s^22s^22p^6\ ^1S_o$ - $2p^54d\ ^3P_1$	-	12.403(5)	12.403	12.411	a	0.09(.04)
12	Ni XIV	$1s^22s^22p^6\ ^1S_o$ - $2p^53d\ ^1P_1$	-	12.431(5)	12.431	12.437	a	
13	-		-	12.600(12)	12.600	12.598	a	
14	Fe XVII	$1s^22s^22p^6\ ^1S_o$ - $2p^54s\ ^3P_1$	-	12.683(7)	12.683	12.681,12.681	a,c	0.057(.016)
15	Ne IX	$1s^2\ ^1S_o$ - $1s2p\ ^1P_1$	13.449(6)	13.443(3)	13.445	13.446	a	0.72*
16	Blend Fe XIX, XXI, XVIII		13.501(13)	-	-	13.49	b	
17	Ne IX	$1s^2\ ^1S_o$ - $1s2p\ ^3P_1$	13.555(7)	13.547(3)	13.550	13.551	a	0.15(.03)
18	Ne VIII	$1s^22s\ ^2S_{1/2}$ - $1s2p(^1P)2s\ ^2P_{1/2,3/2}$	13.663(10)	13.664(4)	13.664	13.660	a	
19	Ne IX	$1s^2\ ^1S_o$ - $1s2s\ ^3S_1$	13.700(6)	13.698(3)	13.699	13.698	a	0.44(.07)
20	Ni XIX	$1s^22s^22p^6\ ^1S_o$ - $2p^53s\ ^1P_1$	13.780(6)	13.784(3)	13.783	13.774	a	
21	Fe XVII	$1s^22s^22p^6\ ^1S_o$ - $2p^53p\ ^1P_1$	13.830(3)	13.826(3)	13.828	13.824,13.820	a,c	0.128(.012)
22	Fe XVII	$1s^22s^22p^6\ ^1S_o$ - $2s2p^63p\ ^3P_1$	13.901(2)	13.890(6)	13.898	13.889,13.887	a,c	0.037(.009)
23	Ni XIX	$1s^22s^22p^6\ ^1S_o$ - $2p^53s\ ^3P_1$	-	14.031(5)	14.031	13.037	a	
24	Fe XVIII	$1s^22s^22p^5\ ^2P_{3/2}$ - $2p^4(^1D)3d\ ^2D_{3/2}$	14.141(6)	14.133(4)	14.137	14.14,14.150	b,c	
25	Fe XX		14.185(10)	14.195(3)	14.192	14.190,14.19	a,b	
26	-		14.226(4)	-	14.226	14.23	b	

TABLE III. (Continued)

Line #	Possible Identification Ion	Transition	Measured Wavelength (A) λ_1	λ_2	$\bar{\lambda}$	Published λ(A)	Reference	Oscillator Strength (observed)
27	Fe XVIII	$1s^2 2s^2 2p^5\ ^2P_{3/2} - 2p^4(^1D)3d\ ^2S$	14.255(10)	14.253(13)	14.254	14.255	c	
28	Fe XV		14.358(10)	14.352(10)	14.355	14.36	b	
29	Fe XVIII	$1s^2 2s^2 2p^5\ ^2P_{3/2} - 2p^4(^3D)3d\ ^2D_{5/2}$	-	14.368(8)	14.368	14.372,14.373	a,c	
30	Fe XVIII		14.409(6)	14.401(10)	14.405	14.40	b	
31	Fe XVIII	$1s^2 2s^2 2p^2\ ^2P_{3/2} - 2p^4(^3P)3d\ ^4P_{5/2}$	14.420(5)	14.426(6)	14.423	14.419	c	
32	Fe XVIII	$1s^2 2s^2 2p^5\ ^2P_{3/2} - 2p^4(^3P)3d\ ^2F$	14.537(2)	14.534(6)	14.536	14.533,14.536	a,c	
33	Fe XVIII	$1s^2 2s^2 2p^5\ ^2P_{3/2} - 2p^4(^1D)3d\ ^2S_{1/2}$	-	14.550(9)	14.550	14.553,14.531	a,c	
34	Fe XVII	$1s^2 2s^2 2p^6\ ^1S_o - 2p^5 3d\ ^1P_1$	15.004(3)	15.011(2)	15.009	15.013	a	2.22*
35	-		15.064(6)	15.069(2)	15.068	15.070	a	
36	-		15.098(8)	15.110(4)	15.106	15.105	a	
37	O VIII	$1s^2\ ^2S_{1/2} - 4p\ ^2P_{1/2,3/2}$	15.167(3)	15.175(2)	15.171	15.179	a	
38	-		15.200(2)	15.207(2)	15.204	15.210	a,b	
39	Fe XVII	$1s^2 2s^2 2p^6\ ^1S_o - 2p^5 3d\ ^3D_J$	15.254(1)	15.260(1)	15.256	15.259,15.261	a,c	0.98(.08)
40	-		15.311(10)	-	15.311			
41	-		15.352(4)	15.357(3)	15.355	15.348,15.35	a,b	
42	Fe XVII	$1s^2 2s^2 2p^6\ ^1S_o - 2p^5 3d\ ^3P_1$	15.460(3)	15.457(2)	15.455	15.449,15.453	a,c	0.18(.04)
43	Fe XVIII	$1s^2 2s^2 2p^5\ ^2P_{1/2} - 2p^4(^1S)3s\ ^2S_{1/2}$	15.486(5)	15.490(10)	15.487	15.488	a	
44	Fe XV		15.513(4)	15.510(5)	15.512	15.513,15.512	a,c	
45	-		15.563(5)	15.556(4)	15.559	15.557	a	
46	-		15.684(2)	15.681(2)	15.682	15.68	b	
47	Fe XVIII	$1s^2 2s^2 2p^5\ ^2P_{1/2} - 2p^4(^3P)3s\ ^2P$	15.773(7)	15.779(10)	15.775	15.78,15.774	b,c	
48	Fe XVIII	$1s^2 2s^2 2p^5\ ^2P_{1/2} - 2p^4(^3P)3s\ ^2P_{3/2}$	15.840(6)	15.832(7)	15.837	15.847	c	
49	O VIII	$1s\ ^2S_{1/2} - sp\ ^2P_{1/2,3/2}$	16.056(4)	16.001(2)	16.001	16.000,16.01	a,b	0.10(.02)
50	Fe XVIII	$1s^2 2s^2 2p^5\ ^2P_{3/2} -$	-	16.068(5)	16.068	16.055,16.073	a,c	
51	O VII	$1s^2\ ^1S_o - 1s4p\ ^1P_1$	-	18.490(10)	18.490			
52	O VII	$1s^2\ ^1S_o - 1s3p\ ^1P_J$	18.630(5)	18.628(2)	18.628	18.606,18.63	a,b	0.22(.05)

TABLE III. (Continued)

Line #	Possible Identification: Ion	Transition	Measured Wavelength (A): λ_1	λ_2	$\bar{\lambda}$	Published λ(A)	Reference	Oscillator Strength (observed)
53	O VIII	$1s\ ^2S_{1/2}$ - $2p\ ^2P_{1/2,3/2}$	18.970(5)	18.970(2)	18.970	18.950,18.96	a,b	0.42*
54	O VII	$1s^2\ ^1S_o$ - $1s2p\ ^1P_1$	21.602(1)	21.602(1)	21.602	21.58,21.60	a,b	0.69*
55	Blended O VII Satellites		21.650(6)	21.645(5)	-			
56	O VII	$1s^2\ ^1S_o$ - $1s2p\ ^3P_1$	21.805(2)	21.808(3)	21.806	21.78	a	0.17(.03)
57	O VII(33)	$1s^22s\ ^2S$ - $1s2p2s\ ^2P_o$	22.024(5)	22.038(3)	22.032			
58	O VII	$1s^2\ ^1S_o$ - $1s2p\ ^3S_1$	22.113(5)	22.120(4)	22.118	22.07	a	0.47(.10)

Where the references are:

a Parkinson, 1975

b Neupert et al., 1973

c Reader and Sugar, 1975

* Value adopted from Parkinson, 1975 to calculate other members of particular ion stage.

λ_1 is from McMath 12379 and 12387.

λ_2 is from McMath 12664

Uncertainty on measured wavelenghts are in units of 0.001Å.

TABLE IV. Emission Line Fluxes (photons/cm^2/sec)

Line #	Quiet Corona		McMath 12379		McMath 12387		McMath 12664
	3' FOV	35" FOV	3' FOV	35" FOV	3' FOV	35" FOV	35" FOV
1	NO DATA		NO DATA		NO DATA		48(9.5)
2							16(6.0)
3							40(8.3)
4							37(8.5)
5							< 5
6							< 5
7							< 5
8							176(23.5)
9							70(14.8)
10							< 5
11							19(13.7)
12							30(6.0)
13							20(4.6)
14							14(2.1)
15	NO DATA	< 4	NO DATA	56(24.4)	NO DATA	96(17.0)	254(26.4)
16		< 4		< 4		< 4	< 5
17		< 4		12(5.4)		19(7.2)	
18		< 4		< 4		< 4	< 5
19		< 4		44(7.9)		78(30.4)	161(23.3)
20		NO DATA		NO DATA		NO DATA	18(4.2)
21							53(31.5)
22							20(17.6)
23							21(8.1)

TABLE IV. (Continued)

Line #	Quiet Corona		McMath 12379		McMath 12387		McMath 12664
	3' FOV	35" FOV	3' FOV	35" FOV	3' FOV	35" FOV	35" FOV
24	NO DATA	NO DATA	NO DATA	NO DATA	NO DATA	NO DATA	161(23.3)
25							56(22.9)
26							< 5
27							21(15.4)
28							< 5
29							25(8.7)
30							< 5
31							< 5
32							26(8.0)
33							< 5
34	< 5	< 4	1799(1.8)	243(1.8)	2230(2.1)	375(25.3)	1216(23.5)
35	< 5	< 4	125(1.7)	-	175(2.1)	-	71(20.9)
36	< 5	< 4	62(2.9)	-	86(2.6)	-	33(28.1)
37	< 5	< 4	116(2.3)	-	169(2.3)	-	101(18.1)
38	< 5	< 4	331(1.6)	39(10.9)	409(2.6)	44(6.6)	153(17.9)
39	< 5	< 4	918(1.8)	96(14.2)	1233(1.8)	140(8.9)	519(29.1)
40	< 5	< 4	77(10.6)	-	106(2.0)	-	-
41	< 5	< 4	-	21(6.9)	-	22(3.8)	68(15.9)
42	< 5	< 4	172(1.9)	25(8.1)	265(1.9)	23(3.7)	91(28.5)
43	< 5	< 4	-	-	-	-	33(10.6)
44	< 5	< 4	88(2.0)	-	108(2.2)	-	46(15.7)
45	< 5	< 4	47(3.3)	-	52(2.7)	-	21(7.0)
46	< 5	< 4	64(1.8)	13(1.6)	96(1.9)	11(22.0)	37(10.9)
47	< 5	< 4	34(2.6)		28(4.2)	-	17(7.0)
48	< 5	< 4	-	-	-	-	25(15.3)

TABLE IV. (Continued)

	Quiet Corona		McMath 12379		McMath 12387		McMath 12664
Line #	3' FOV	35" FOV	3' FOV	35" FOV	3' FOV	35" FOV	35" FOV
49	< 5	< 4	18(3.4)	–	32(7.8)	–	18(17.8)
50	< 5	< 4	383(1.4)	42(4.9)	591(1.9)	88(6.2)	234(8.1)
51	< 5	< 4	–		–		
52	NO DATA	–	NO DATA	< 8	NO DATA	≤ 8	≤ 17
53		< 8		38(9.8)		82(6.2)	189(9.5)
54		< 8		352(8.8)		493(5.0)	2350(16.2)
55	477(1.1)	20	2122(1.3)	146(8.2)	3376(1.5)	205(5.1)	630(8.9)
56	14(1.1)	–	144(2.3)	–	215(1.7)	–	–
57	72(2.5)	44	713(1.3)	59(3.6)	1095(1.6)	64(4.3)	191(7.7)
58	9(1.3)	–	25(4.8)	–	26(2.3)	–	–
59	236(1.1)	20	2122(1.3)	146(8.2)	3376(1.5)	205(5.1)	630(8.9)

TABLE 7

Ions	λ_1/λ_2	f_1/f_2	Effective Temperature (T_6)		
			McMath 12379	McMath 12387	McMath 12664
O VII/O VIII	18.603/18.950	0.22/0.42	3.3(±0.4)	2.9(±0.5)	3.5(±0.5)
Fe XVII/Fe XVIII	15.001/16.06	2.2 /0.6	-	-	3.4(±.2)
Ne IX/Ne X	13.44/12.13	0.72/0.42	-	-	3.9(±.4)

TABLE VI: Line Ratios of the He-like Ions

Coronal Region (1) - 25.002 (2) - 26.003	Mean Observed Ratios							
	O VII (3' FWHM)		O VII (35" FWHM)		Ne IX (35" FWHM)		Mg XI (35" FWHM)	
	R	G	R	G	R	G	R	G
Quiet Region (1)	3.3(.3)	0.63(.07)	-	-	-	-	-	-
McMath 12379 (1)	3.05(.14)	0.84(.04)	2.5(1.3)	0.96(.15)	3.5(.8)	0.98(.16)	-	-
McMath 12387 (1)	3.12(.15)	1.06(.03)	3.1(0.7)	1.22(.20)	3.0(1.1)	0.96(.20)	-	-
McMath 12664 (2)	-	-	2.9(0.4)	0.94(.12)	3.0(0.4)	0.84(.09)	2.5(0.8)	1.14(.20)

Table VII

Ion #	O VII 1	O VIII 2	Fe XVII 4	Ne IX 3	Mg XI 5
λ(A)	21.60	18.95	15.01	13.44	9.17
f	0.69	0.42	2.2	0.72	0.75
A	$2.4.10^{-4}$	$2.4.10^{-4}$	$5.2.10^{-5}$	$4.0.10^{-5}$	$4.5.10^{-5}$
$T_{max}(10^6\ ^oK)$	2.0	3.2	4.4	3.6	6.3
ΔT(1/e)	1.3-3.3	2.0-5.7	2.5-6.8	2.1-5.9	3.5-10.0
Pointing Position			Data (phts/cm^2/sec)		
MM 12379-1	24300	38000	34000	5350	-
-2	45000	62700	52700	12200	-
-3	45500	65200	32200	10200	-
-4	38300	71000	35200	7050	-
-5	15900	8100	2800	-	-
-6	9500	11500	7800	500	-
-7	13600	14200	5300	2800	-
-8	23700	18500	-	1100	-
MM 12387 -9	36700	17700	4100	1650	-
-11	47500	36700	16000	2500	-
-12	46000	54300	38300	6300	-
-14	58600	88600	104000	9530	-
MM 12664-1	274000	-	352000	88300	9950
-2	177000	-	347000	61300	11100
-3	82000	-	157000	25000	6500
-4	34200	-	35200	7350	1000
-5	46500	-	29600	3350	1250
-6	120000	-	90100	12600	2500
-7	188000	-	142000	25100	5350
-8	133000	-	61800	15400	2100
-9	35900	-	15000	4450	1850
-10	67300	-	45600	11400	1500

TABLE VIII

Pointing Position	T_{max} (10^6 °K)	$\bar{T}$	$\Delta T(1/e)$ (10^6 °K)	Integrated E.M. for F.O.V. (units of 10^{46} cm^{-3})	V(%)	Fitting Ratio			
						O VII	O VIII	Fe XVII	Ne IX
MM 12379-1	3.3		.5	14.1	13	.89	1.16	.90	1.04
-2	3.4		.4	26.3	22	.89	1.03	.78	1.28
-3	2.9		.4	23.4	32	.92	1.21	.55	1.24
-4	2.9	2.9(±.5)	.5	21.4	33	.85	1.45	.66	.95
-5	2.2		.4	4.5	22	.89	1.23	.83	-
-6	2.5		.4	5.0	39	.82	1.49	1.01	.57
-7	3.0		.8	6.6	43	.95	1.06	.39	1.44
-8	2.5		.3	6.9	29	.93	1.20	.74	-
MM 12387-9	2.1		.4	14.0	28	.64	1.23	.86	1.20
-11	2.4	2.6(±.4)	.5	13.8	21	.92	1.30	.90	.84
-12	2.9		.7	20.0	15	.92	1.21	.86	.99
-14	2.9		.7	50.1	14	.92	1.20	.96	.88
						O VII	Fe XVII	Ne IX	Mg XI
MM 12664-1	2.9		.5	195.0	30	.93	.80	1.41	.77
-2	3.4		.6	129.0	22	.79	.96	1.30	.91
-3	3.5		.5	57.5	12	.91	.93	1.18	.97
-4	3.0	3.0(±.5)	.6	16.2	22	.95	.88	1.31	.82
-5	1.0, 2.5*		-	21.4	6	1.01	1.07	.93	.98
-6	2.8		.9	43.7	3	.99	1.04	1.00	.97
-7	3.0		1.6	74.1	9	.99	.88	1.11	1.01
-8	2.7		1.3	47.9	21	.94	.77	1.27	.98
-9	3.1		2.4	21.9	27	.96	.66	1.31	1.00
-10	2.9		1.1	27.5	25	.94	.77	1.34	.88

*Double Peaked

Fig. 1 - Sample Spectra

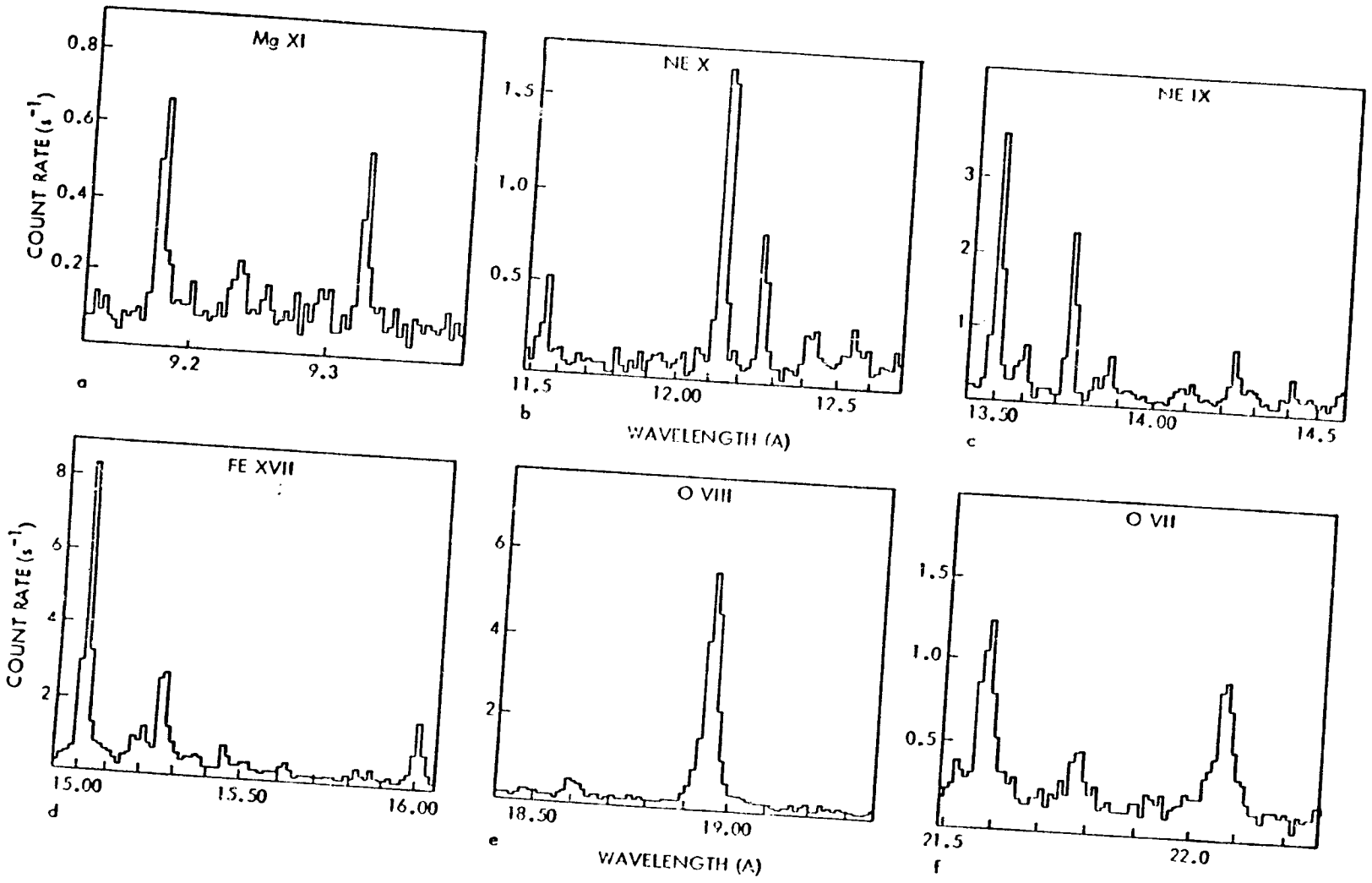

Figure 2

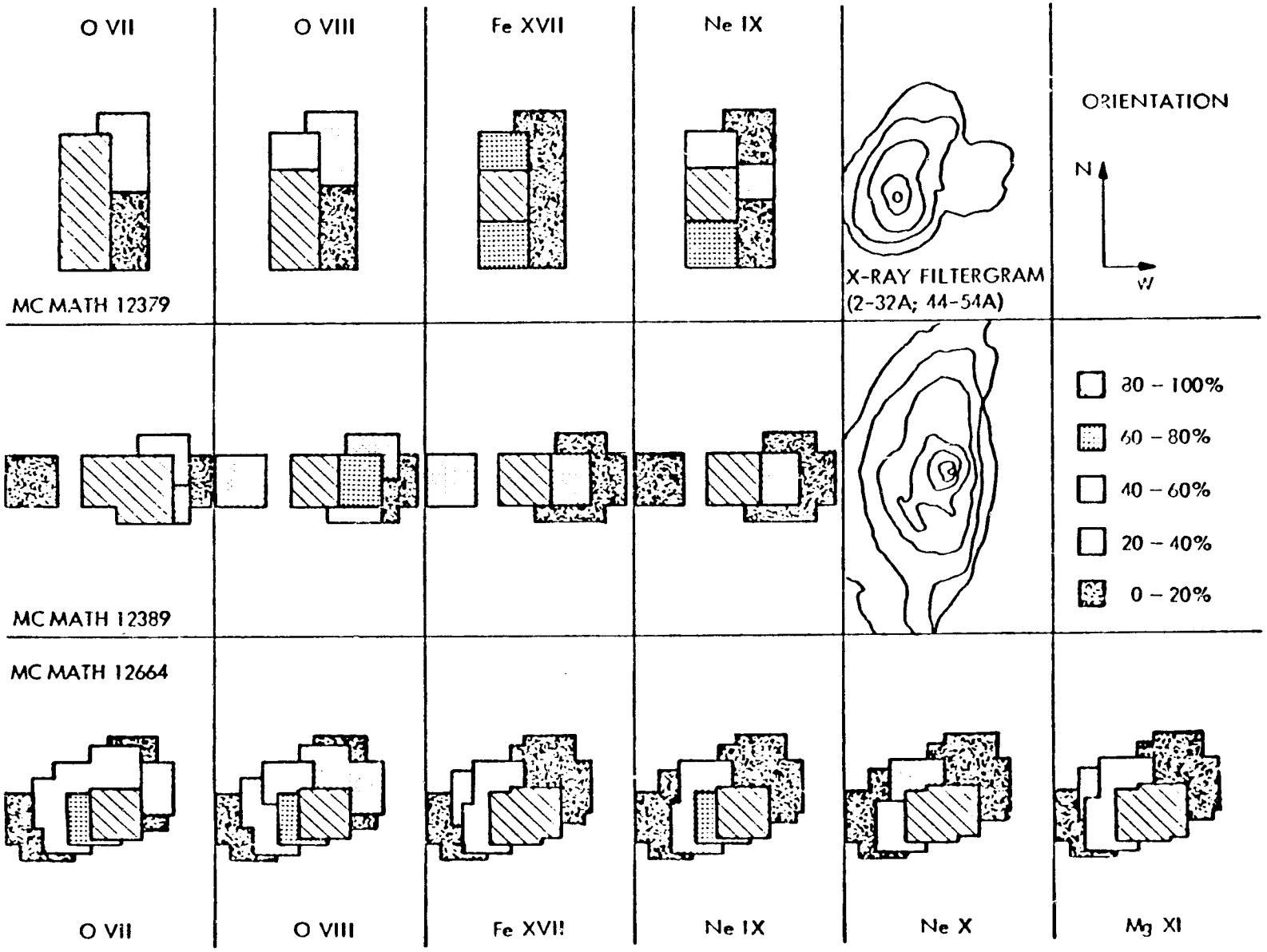
O VII
O VIII
Fe XVII
Ne IX
ORIENTATION
N
W
X-RAY FILTERGRAM
(2-32A; 44-54A)
MC MATH 12379
80 – 100%
60 – 80%
40 – 60%
20 – 40%
0 – 20%
MC MATH 12389
MC MATH 12664
O VII
O VIII
Fe XVII
Ne IX
Ne X
Mg XI

Figure 3

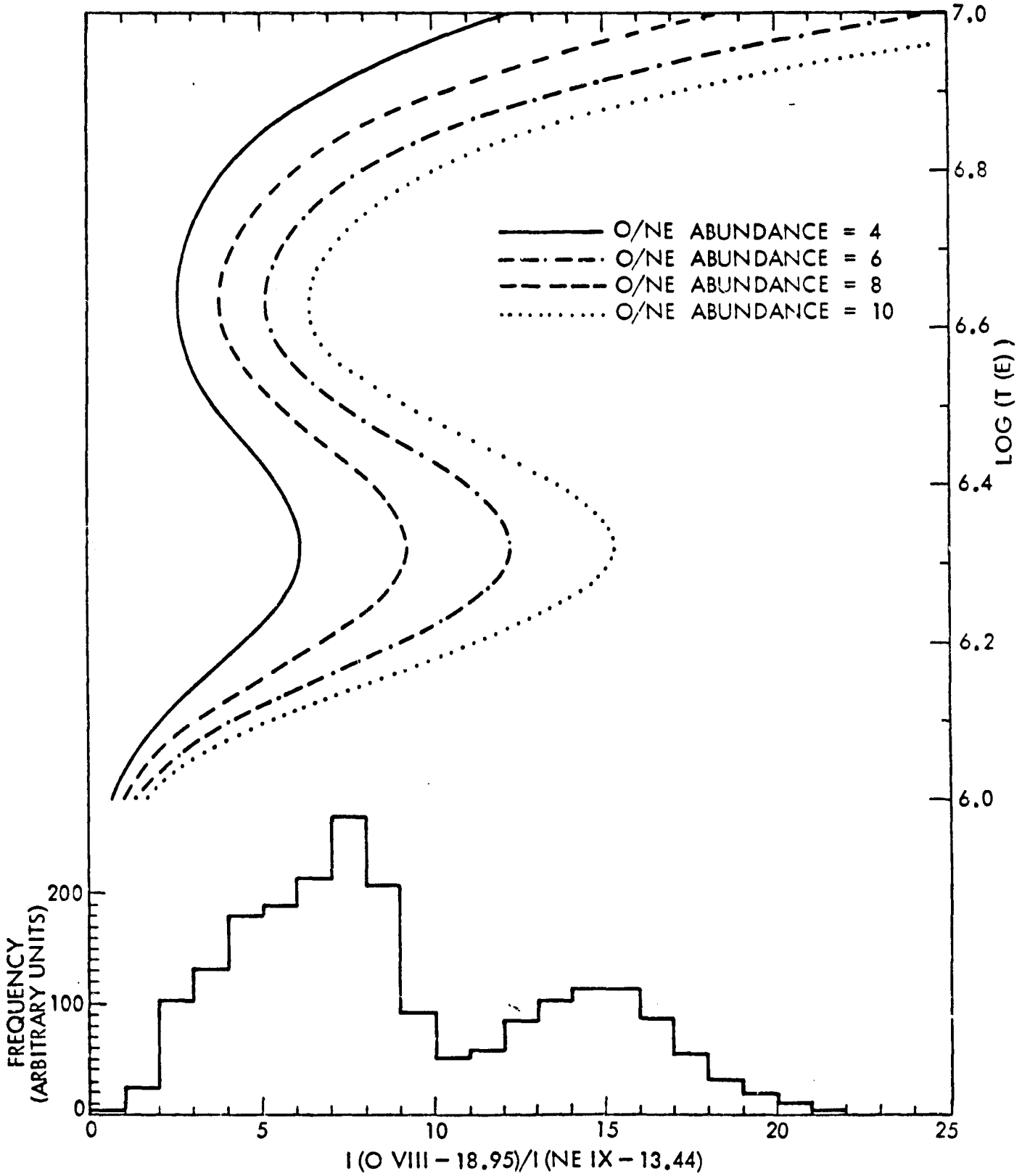
O/NE ABUNDANCE = 4
O/NE ABUNDANCE = 6
O/NE ABUNDANCE = 8
O/NE ABUNDANCE = 10
LOG (T (E))
7.0
6.8
6.6
6.4
6.2
6.0
FREQUENCY (ARBITRARY UNITS)
200
100
0
0
5
10
15
20
25
I (O VIII – 18.95)/I (NE IX – 13.44)

Figure 4

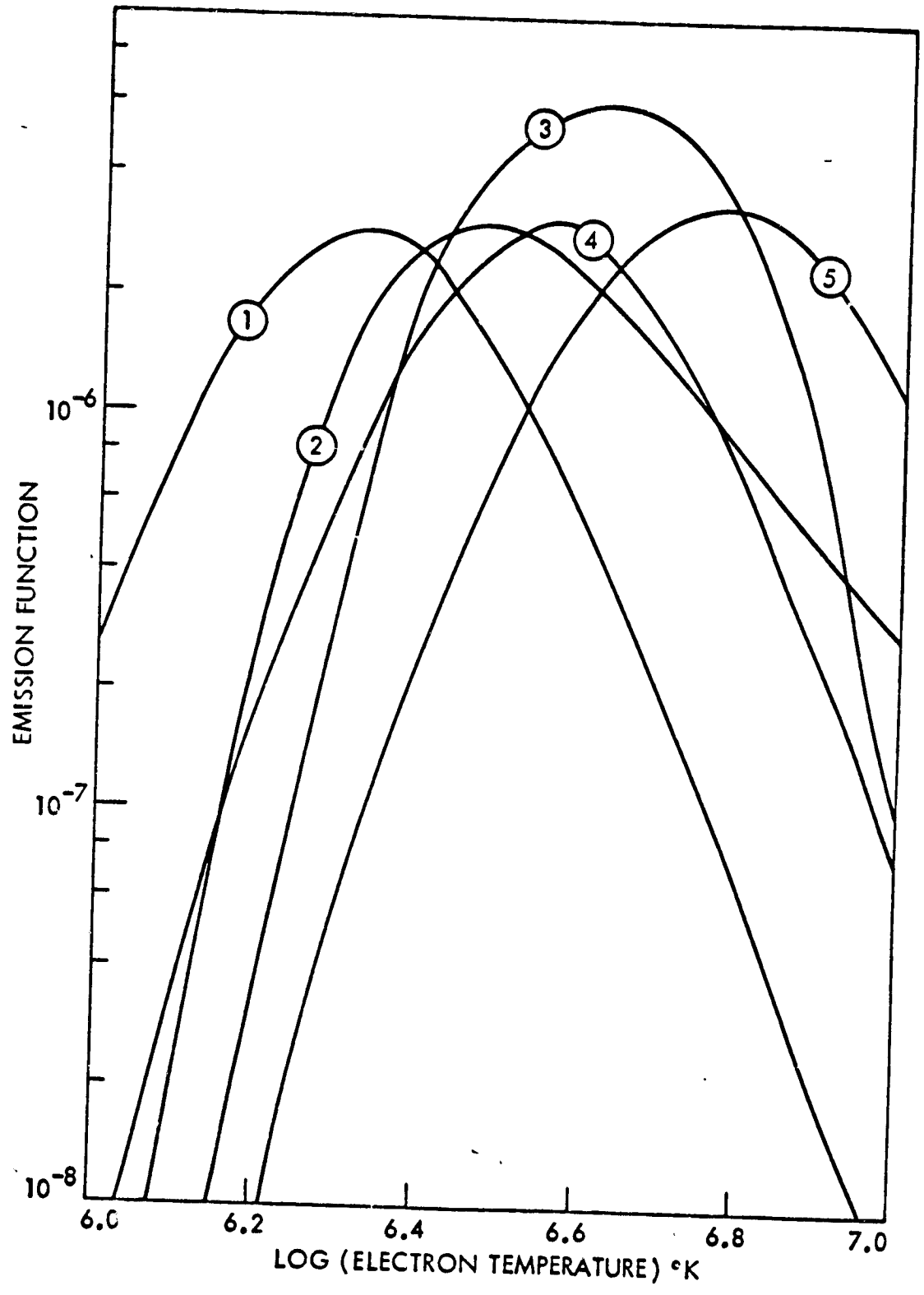
EMISSION FUNCTION
10^{-6}
10^{-7}
10^{-8}
1
2
3
4
5
6.0
6.2
6.4
6.6
6.8
7.0
LOG (ELECTRON TEMPERATURE) °K

Appendix 2

Contents

Table I. Primary Characteristics of the Instruments.

Ion	O VII	O VII	O VIII	Fe XVII	Fe XVII	Ne IX
(1) Aerobee 26.002						
Wavelength range (Å)	21.4-22.3	21.4-22.3	18.3-19.4	14.9-16.1	14.9-16.1	13.3-14.6
Field of view (FWHM)	149"	34"	34"	148"	33"	31"
Collimator Transmission (η)	0.32	0.19	0.20	0.31	0.19	0.18
Geometric constants (C_1)	17.4	17.2	15.8	16.1	14.8	14.7
(Eq. (7)) (C_2)	2.4	2.4	2.0	1.3	1.2	0.63
(C_3)	21.252	21.252	18.20	14.894	14.894	13.318
Crystal Integrated Reflectivity (R_c)	$5.3.10^{-5}$	$5.3.10^{-5}$	$5.0.10^{-5}$	$6.1.10^{-5}$	$6.1.10^{-5}$	$6.6.10^{-5}$
Counter efficiency (E)	0.18	0.17	0.26	0.37	0.38	0.40
(2) Aerobee 26.003	O VII	O VIII	Fe XVII	Ne IX	Ne X	Mg XI
Wavelength range (Å)	21.4-22.3	18.3-19.4	14.9-16.1	13.3-14.6	11.4-12.8	9.09-9.39
Field of view (FWHM)	36"	32"	41"	40"	39"	35"
Collimator Transmission	0.12	0.09	0.14	0.15	0.14	0.11
Geometric Constant (C_1)	18.7	15.8	14.8	14.7	15.7	20.30
(C_2)	2.6	2.0	1.2	0.66	.73	-7.3
(C_3)	21.427	18.329	14.888	13.313	11.496	9.10
Crystal Integrated Reflectivity	$5.3.10^{-5}$	$5.0.10^{-5}$	$6.1.10^{-5}$	$6.6.10^{-5}$	$7.1.10^{-5}$	$8.9.10^{-5}$ (ADP)
Counter Efficiency	0.15	0.27	0.35	0.38	0.36	0.47

TABLE II

Details of Aerobee 26.002 Pointing Positions

Launched on 11th June 1973 at 18 hrs. 30 mins 2.4s U.T.

Pointing Position Identification	Pointing Position		Start Time of Integration		Integration Time
	N	E			
	Arc Seconds		m	s	s
DSK CTR PRE-RL	95	67	31	44.7	22.8
DSK CTR RL	95	67	32	07.5	9.0
DSK CTR POST-RL	95	67	32	16.5	9.8
MOVE TO AR131	335	310	32	28.6	8.6
AR131-1	335	235	32	38.6	19.8
AR131-2	285	235	32	59.0	14.5
AR131-3	240	235	33	14.1	∿ 14.4
AR131-4	240	235	33	29.1	∿ 14.4
AR131-5	240	185	33	44.1	14.3
AR131-6	260	185	33	58.8	14.7
AR131-7	310	185	34	14.1	14.4
AR131-8	360	185	34	29.1	14.0
MOVE TO AR137	360	670	34	46.3	13.6
AR137-9	360	810	34	58.9	16.0
AR137-10	310	810	35	15.6	16.2
AR137-11	310	835	35	32.3	13.6
AR137-12	335	835	35	46.3	19.3
AR137-13	335	785	36	06.3	13.7
AR137-14	335	880	36	21.6	14.2
AR137-15	335	980	36	36.6	13.7

Table III

26.002 Oxygen VII (3' F.O.V.) Line Intensities (photons/cm^2/sec)

Pointing Position	Resonance Line (R) (21.602A) (F_1 = 446.70)	S_{1-2} (21.650A) (F_2 = 444.83)	Intersystem Line (I) (21.805A) (F_3 = 439.13)	S_3 (22.024A) (F_4 = 431.92)	Forbidden Line (F) (22.103A) (F_5 = 429.56)
CTR PRE RL	43200 (400)	2200 (900)	8200 (400)	950	22300 (2100)
CTR ROLL	47400	2000	9600 (300)	900	25300 (3000)
CTR PST RL	47400	-	3900 (1100)	730 (600)	23200 (900)
MOVE TO 131	302900 (20000)	14900	72500 (1600)	3200 (500)	170900 (8200)
AR 131-1	333200 (5800)	11100 (1200)	75100 (1300)	-	215200 (3000)
AR 131-2	375200 (25500)	17800 (5000)	76800 (400)	1400	242300 (500)
AR 131-3	350200 (1800)	10300 (400)	76000 (800)	6700	230200 (4700)
AR 131-4	335000 (4500)	21900 (4800)	75600 (800)	1700 (1300)	219900 (9000)
AR 131-5	318500 (1300)	9700 (800)	61000 (4000)	4400	188600 (6900)
AR 131-6	325600 (8900)	11800 (900)	72500 (2600)	300	222900 (7300)
AR 131-7	355100 (3100)	15600 (3500)	75100 (1800)	4400 (1200)	223800 (900)
AR 131-8	292100 (4900)	16100 (1400)	57100 (400)	-	195900 (8600)
MOVE TO 137	55800 (3600)	6600 (1600)	11200 (1200)	300	35200
AR 137-9	427000 (5400)	23800 (2400)	112000 (2200)	4600	352200 (7300)
AR 137-10	377000 (7600)	22700 (7800)	100600 (1800)	3300	321300 (3400)
AR 137-11	433300 (4900)	24000 (2200)	124300 (5700)	-	372400 (1700)
AR 137-12	464600 (1300)	26600 (3600)	126900 (2200)	2300	378900 (6000)
AR 137-13	310000 (2700)	16200 (2400)	81700 (400)	-	256400 (3900)
AR 137-14	430600 (7600)	15600 (1200)	112000 (5300)	5300 (21000)	344100 (5200)
AR 137-15*	234100 (5900)	12700 (7100)	71100 (7900)	4600	249600 (900)

* Probably affected by atmospheric absorption.

Table IV

26.002 Oxygen VII (35" F.O.V.) Line Intensities (photons/cm^2/sec)

Pointing Position	Resonance Line (R) (21.602 A) (F_1 = 795.38)	Intersystem Line (I) (21.805 A) (F_2 = 781.66)	Forbidden Line (F) (22.103 A) (F_3 = 764.32)
CTR PRE RL CTR ROLL CTR PST RL	7100 (1700)	4400 (1600)	2000 (1400)
MOVE TO 131	-	-	-
AR 131-1	28000 (2800)	2600 (1900)	15900 (2400)
AR 131-2	29500 (3600)	7500 (2700)	26700 (3400)
AR 131-3	32800 (3000)	9300 (2300)	25300 (2700)
AR 131-4	33700	7200	21900 (2100)
AR 131-5	7700 (2200)	4700 (2000)	7400 (2100)
AR 131-6	9200 (2200)	3400 (2000)	3800 (2800)
AR 131-7	12300 (2200)	7200 (2100)	3100 (3100)
AR 131-8	13900 (2500)	5000 (2100)	13000 (2400)
MOVE TO 137	2200	-	1600
AR 137-9	19600 (2700)	6900 (2200)	21000 (2700)
AR 137-10	9100 (2500)	3300 (2200)	5600 (2200)
AR 137-11	27200 (3100)	5900 (3200)	30200 (3100)
AR 137-12	34600 (3000)	7500 (2300)	27500 (2800)
AR 137-13	5300 (2200)	2800 (2000)	6300 (2100)
AR 137-14	33500 (3600)	12100 (2800)	32100 (3400)
AR 137-15*	5800 (2500)	5900 (3200)	13000 (2700)

* Probably affected by atmospheric absorption

Table V

26.002 Oxygen O VII & O VIII Line Intensity (Photons/cm^2/sec)

Pointing Position	O VIII (Lyman α) (18.97A) (F_1 = 601.01)	O VII (18.63A) (F_2 = 614.4)
CTR PRE RL		
CTR ROLL		
CTR PST RL		
MOVE TO 131	27900 (4900)	5000 (2600)
AR 131-1	38000 (5500)	4600 (2500)
AR 131-2	62700 (9400)	6000 (4100)
AR 131-3	65200 (8100)	6500 (3400)
AR 131-4	71000 (8800)	8800 (4200)
AR 131-5	8100 (2700)	900 (800)
AR 131-6	11500 (3500)	1100 (2500)
AR 131-7	14200 (3600)	1100 (2800)
AR 131-8	18400 (4300)	-
MOVE TO 137	-	-
AR 137-9	17700 (4500)	2900 (2100)
AR 137-10	-	-
AR 137-11	36700 (7100)	3800 (4400)
AR 137-12	54300 (7200)	8100 (2200)
AR 137-13	-	-
AR 137-14	88600 (11700)	18100 (8000)
AR 137-15	25300 (2600)	1600 (1800)

Table VI

26.002 Fe XVII (3' F.O.V.) Line Intensities (Photons/cm^2/sec)

Pointing Positions	1 (15.004A) (F_1=271.8)	3 (15.064A) (F_3=270.0)	4 (15.098A) (F_4=268.9)	6 (15.167A) (F_6=266.8)	7 (15.20A) (F_7=265.8)
CTR PRE RL CTR ROLL CTR PST RL	-	-	-	-	-
MOVE TO 131	147800 (2200)	9300 (1900)	3700 (500)	4900 (800)	36100 (3700)
AR 131-1	216100 (6000)	15900 (2700)	8500 (1900)	18200 (2700)	38200 (3700)
AR 131-2	245000 (7600)	13400 (3200)	7800 (2400)	18800 (3200)	39400 (4500)
AR 131-3	209100 (8400)	12500 (3800)	10700 (2700)	15000 (2900)	37300 (4000)
AR 131-4	192600 (6500)	16000 (2700)	5000 (2400)	8400 (2100)	35200 (3000)
AR 131-5	145200 (6000)	9200 (2700)	5600 (2200)	8900 (2100)	24500 (2900)
AR 131-6	164400 (5200)	12500 (2400)	5600 (2200)	8300 (1900)	27800 (2700)
AR 131-7	162100 (5700)	12500 (2400)	3700 (1900)	10600 (2100)	34300 (3200)
AR 131-8	136400 (5200)	10800 (3000)	4800 (1900)	11700 (2100)	25000 (2700)
MOVE TO 137	9100 (4100)	-	-	-	-
AR 137-91	198900 (6500)	12600 (3000)	8500 (2200)	15200 (2900)	37300 (3500)
AR 137-10	186700 (6500)	14000 (3000)	8200 (2200)	14500 (2700)	33300 (3200)
AR 137-11	237100 (8200)	18900 (3800)	11800 (3000)	17700 (3200)	42800 (4300)
AR 137-12	258000 (8200)	21700 (4000)	9400 (3000)	20800 (3200)	48900 (4300)
AR 137-13	149900 (6000)	12400 (3000)	4600 (1900)	10000 (2100)	23000 (2700)
AR 137-14	307300 (10900)	25700 (4900)	9100 (3500)	23400 (4300)	59900 (5300)
AR 137-15					

Table VI (Continued)

26.002 Fe XVII (3' F.O.V.) Line Intensities (Photons/cm^2/sec)

Pointing Position	18 (15.563A) (F_{18}=255.4)	20 (15.628A) (F_{20}=253.7)	21 (15.684A) (F_{21}=252.1)	24 (15.840A) (F_{24}=248.1)	27 (16.000A) (F_{27}=243.8)
CTR PRE RL CTR ROLL CTR PST PL	-	-	-	-	-
MOVE TO 131	3800 (500)	6800 (500)	3500 (500)	3400 (2)	38500 (8300)
AR 131-1	6200 (1500)	8000 (1500)	2300 (1300)	3200 (1200)	42100 (3000)
AR 131-2	9100 (2000)	8800 (2000)	4600 (2000)	-	44900 (3700)
AR 131-3	2800 (1800)	6700 (1800)	3800 (1800)	1700 (1200)	43600 (3700)
AR 131-4	3800 (1500)	6800 (1800)	2200 (1800)	-	40900 (3200)
AR 131-5	3400 (1300)	5000 (1500)	3100 (4300)	2500 (1000)	27300 (2400)
AR 131-6	5300 (1300)	4800 (1300)	4100 (4300)	2500	34900 (2700)
AR 131-7	4700 (1300)	5700 (1300)	5300 (1300)	1900 (1200)	41300 (2900)
AR 131-8	3200 (1300)	5000 (1300)	1800 (1300)	1000 (1000)	31600 (2400)
MOVE TO 137	-	-	-	-	-
AR 137-9	6600 (1800)	10700 (2000)	2800 (1500)	4400 (1700)	53100 (3900)
AR 137-10	4100 (1800)	6800 (2000)	2700 (1500)	3200 (1500)	49900 (3700)
AR 137-11	4700 (2000)	7400 (1800)	1700 (1800)	2700 (1500)	60600 (4100)
AR 137-12	4600 (2000)	12900 (2300)	4600 (1800)	3900 (2000)	73400 (4400)
AR 137-13	3100 (1800)	7200 (1800)	1100 (1200)	2400 (1200)	40700 (3600)
AR 137-14	8200 (2800)	12400 (2800)	3700 (2500)	2500 (2200)	76900 (4400)
AR 137-15					

Table VI (Cont.) 26.002 Fe XVII (3' FOV) Line Intensities (Photons/cm^2/sec)

Pointing Position	8 (15.254A) (F_8=264.2)	10 (15.311A) (F_{10}=262.0)	11 (15.352A) (F_{11}=261.4)	15 (15.460A) (F_{15}=258.6)	17 (15.513A) (F_{17}=256.8)
CTR PRE RL CTR ROLL CTR PST RL	-	-	-	-	-
MOVE TO 131	75200 (7200)	2800 (1100)	15200 (1800)	8700 (500)	7600 (1800)
AR 131-1	108400 (3200)	10900 (2400)	23400 (2400)	20900 (400)	12400 (1000)
AR 131-2	119400 (5800)	10400 (2900)	20300 (3900)	23100 (3100)	10300 (2000)
AR 131-3	104900 (5800)	13800 (3000)	22200 (3100)	24900 (3100)	8700 (2100)
AR 131-4	95900 (5000)	8500 (2400)	21300 (2600)	17200 (2600)	9900 (2100)
AR 131-5	76600 (4500)	6200 (2400)	13200 (2100)	13200 (2100)	7900 (1500)
AR 131-6	91600 (4200)	1300 (2100)	17100 (2100)	15100 (2100)	9100 (1500)
AR 131-7	86000 (4500)	8300 (2400)	17100 (2400)	15300 (2100)	6200 (1500)
AR 131-8	68000 (4000)	6900 (1800)	18200 (2400)	16600 (2300)	7400 (1500)
MOVE TO 137	-	-	-	-	-
AR 137-9	111600 (5500)	9600 (2600)	20900 (800)	23500 (2600)	12300 (2300)
AR 137-10	100100 (5000)	7000 (2400)	21400 (3600)	22100 (2600)	10000 (2100)
AR 137-11	132200 (8500)	11600 (3100)	22100 (3700)	25500 (3100)	10400 (2300)
AR 137-12	141800 (6600)	14200 (3100)	29900 (3900)	32100 (3400)	11100 (2300)
AR 137-13	90000 (4500)	7200 (2400)	14200 (2400)	19300 (2600)	6700 (1800)
AR 137-14	164200 (8200)	14100 (4200)	29800 (3900)	36800 (4100)	14400 (3100)
AR 137-15					

Table VII

26.002 Fe XVII (35"F.O.V.) Line Intensities (Photons/cm^2/sec)

Pointing Position	1 (15.011A) (F_1=473.3)	7 (15.207A) (F_7=462.9)	8 (15.260A) (F_8=460.1)	11 (15.352A) (F_{11}=455.2)	13 (15.404A) (F_{13}=452.4)
CTR PRE RL CTR ROLL CTR PST RL	-	-	-	-	-
MOVE TO 131	-	-	-	-	-
AR 131-1	34300 (3800)	7700 (1400)	16300 (1800)	2800 (900)	-
AR 131-2	52700 (2800)	8700 (1400)	19900 (1800)	4800 (1400)	-
AR 131-3	32200 (2800)	5000 (900)	12900 (1800)	2500 (900)	1200 (500)
AR 131-4	35200 (2800)	5300 (900)	11600 (1800)	2500 (900)	-
AR 131-5	2800 (500)	800 (500)	1400 (500)	-	-
AR 131-6	7800 (1500)	-	3400 (900)	1100 (500)	-
AR 131-7	5300 (1500)	-	1600 (500)	700 (500)	-
AR 131-8	-	-	-	-	-
MOVE TO 137	-	-	-	-	-
AR 137-9	4100 (1000)	1100 (500)	3400 (900)	-	-
AR 137-10	-	-	-	-	-
AR 137-11	16000 (1400)	2400 (900)	6100 (900)	3200 (900)	-
AR 137-12	38300 (2800)	6100 (1400)	18000 (1800)	1600 (500)	-
AR 137-13	-	-	-	-	-
AR 137-14	103800 (4700)	7300 (900)	30400 (2800)	4400 (900)	-
AR 137-15	25100 (2400)	5300 (900)	12100 (1800)	2000 (900)	-

Table VII (Continued)

26.002 Fe XVII (35" F.O.V.) Line Intensities (Photons/cm^2/sec)

Pointing Position	15 (15.460Å) (F_{15}=450.3)	16 (15.486Å) (F_{16}=448.6)	19 (15.596Å) (F_{19}=443.2)	24 (15.840Å) (F_{24}=432.0)	27 (16.00Å) (F_{27}=424.5)
CTR PRE RL CTR ROLL CTR PST RL	-	-	-	-	-
MOVE TO 131					
AR 131-1	2900 (900)	1500 (400)	2200 (900)	-	7400 (1300)
AR 131-2	6500 (1400)	3200 (1200)	2200 (900)	1700 (900)	6800 (1300)
AR 131-3	3800 (900)	-	1800 (400)	500 (300)	6200 (1300)
AR 131-4	2200 (900)	1100 (400)	1400 (400)	-	6200 (1300)
AR 131-5	-	-	-	-	-
AR 131-6	1000 (500)	-	-	-	1500 (400)
AR 131-7	800 (500)	-	1400 (900)	-	1500 (400)
AR 131-8	-	-	-	-	-
MOVE TO 137	-	-	-	-	-
AR 137-9	-	-	-	-	3100 (800)
AR 137-10	-	-	-	-	-
AR 137-11	1500 (500)	-	100 (400)	700 (400)	5100 (800)
AR 137-12	2300 (900)	-	1300 (400)	700 (800)	11100 (1300)
AR 137-13	-	-	-	-	-
AR 137-14	5500 (1400)	3300 (1300)	2200 (900)	-	19200 (2100)
AR 137-15	2100 (900)	700 (400)	1700 (400)	-	5300 (900)

TABLE VIII

26.002 Ne IX Line Intensities (photons/cm^2/sec)

Line Identification

Position	Resonance Line (R) (13.447A)	Intersystem Line (I) (13.551A)	Forbidden Line (F) (13.700A)
	(F_R=482.4)	(F_T=477.7)	(F_F=471.6)
AR131-1	5350 (550)	2000 (400)	3100 (500)
AR131-2	12200 (1100)	1600 (550)	7500 (950)
AR131-3	10200 (900)	1600 (400)	7500 (750)
AR131-4	7050 (750)	2700 (500)	8250 (800)
AR131-5	-	-	-
AR131-6	560	-	600
AR131-7	2850 (1000)	500 (300)	3250 (1200)
AR131-8	1100	-	1050
AR137	-	-	-
AR137-9	1650	800	800 (150)
AR137-10	-	-	-
AR137-11	2500 (400)	-	1700 (400)
AR137-12	6300 (850)	1000 (500)	4150 (750)
AR137-13	-	-	-
AR137-14	28050 (2350)	5750 (1050)	24350 (200)
AR137-15	5450 (550)	1450 (400)	4150 (500)

TABLE IX

Details of Aerobee 26.003 Pointing Positions

Launched on 19th December 1973 at 22 hrs. 05m 19 sec.

Pointing Position Identification	Pointing Position		Start Time of Integration		Integration Time (sec)
	N	E			
	Arc Seconds		m	s	s
A (sun center)	12	13	07	28.80	27.55
B (Roll)			07	58.90	6.90
C	14	481	08	08.38	8.82
D	22	607	08	18.95	30.77
E	220	737	08	53.30	4.60
F	-188	533	09	02.50	6.28
G	-162	542	09	09.30	5.18
1	-249	502	09	16.50	17.52
2	-258	531	09	35.27	13.53
3	-269	569	09	50.00	13.93
4	-272	590	10	05.12	13.83
5	-268	607	10	19.48	14.75
6	-241	578	10	34.70	14.40
7	-224	552	10	49.70	14.32
8	-204	502	11	04.70	14.36
9	-190	477	11	19.52	14.68
10	-220	459	11	34.90	14.25
11	-243	457	11	49.63	14.52
12	-274	513	12	04.79	15.03

Table X

26.003 O VII Line Intensities (Photons/cm^2/sec)

Pointing Position #	Resonance Line (R) (21.602 A) (F_1 = 1566.3)	Intersystem Line (I) (21.805 A) (F_2 = 1538.5)	Forbidden Line (F) (22.103 A) (F_3 = 1503.2)
1	211500 (12200)	59200 (7400)	154500 (10500)
2	151300 (8700)	33800 (4200)	103900 (7000)
3	91800 (5300)	17000 (2100)	47000 (3200)
4	41300	-	20900
5	30500 (4200)	7700 (2400)	28600 (3900)
6	102700 (5900)	23200 (2900)	70500 (4800)
7	124600 (7400)	37000 (4400)	109400 (8000)
8	84500 (8500)	24200 (4600)	79400 (7900)
9	37600 (2200)	8000 (1000)	20000 (1400)
10	50100	-	41100
11	35200	-	17200

Table XI

26.003 Oxygen O VII & O VIII Line Intensity (Photons/cm^2sec)

Pointing Position	O VIII (Lyman α) (18.97 A) (F_1 = 1325.0)	O VII (18.63 A) (F_2 = 1355.3)
1	694900 (29800)	60800 (11100)
2	505500 (23000)	33800 (7200)
3	180600 (10000)	10100 (2800)
4	43000 (3000)	6400 (2400)
5	52800 (4200)	-
6	177600 (12800)	20400 (4500)
7	322000 (19000)	28800 (7900)
8	233200 (15600)	19000 (6000)
9	75500 (5200)	19200 (10600)
10	176700 (10000)	9400 (2100)
11	124200	-

TABLE XII

26.003 Fe XVII Line Intensities (photons/cm^2/sec)

Line Identifications

Pointing Position	1 15.011A (F_1=677.0)	3 15.069A (F_3=672.6)	4 15.110A (F_4=669.5)	6 15.175A (F_6=664.6)	7 15.207A (F_7=661.9)	8 15.260A (F_8=660.81)	12 15.363A (F_{12}=658.7)
1	351900 (34000)	23000 (900)	10600 (1000)	30800 (3100)	38700 (4000)	171700 (11800)	15100 (2000)
2	346500 (9000)	18600 (2100)	11300 (4200)	28400 (5000)	43000 (5000)	158700 (5700)	17500 (3300)
3	156800 (14100)	8500 (1800)	4800 (2100)	9600 (2000)	20700 (2700)	70100 (3500)	9500 (1700)
4	35200 (1600)	-	400 (400)	3200 (400)	8100 (1200)	21000 (2300)	3600 (600)
5	29600 (1700)	1100 (400)	-	1700 (400)	5700 (1200)	16000 (2200)	1100 (400)
6	90100 (2400)	3800 (800)	-	7700 (5600)	14300 (900)	41800 (1500)	8400 (1300)
7	141600 (6400)	8400 (700)	4100 (1700)	15100 (2000)	18900 (3700)	18900 (3700)	6500 (1400)
8	61800 (2600)	3700 (800)	-	5200 (1300)	5900 (1300)	28600 (2600)	3300 (400)
9	15000 (1300)	2500 (600)	3000 (1306)	2300 (800)	2400 (1200)	5900 (800)	1500 (400)
10	45600 (7100)	4900 (1300)	1800 (800)	4000 (1200)	4300 (1500)	13700 (1200)	4700 (1200)
11	63700 (8500)	3100 (600)	-	2100 (400)	7200 (1200)	24500 (2500)	3200 (600)

TABLE XII (Continued)

Pointing Position	14 15.422A (F_{14}=646.5)	15 15.451A (F_{15}=644.5)	16 15.490A (F_{16}=641.7)	17 15.510A (F_{17}=640.3)	18 15.556A (F_{18}=636.7)	19 15.608A (F_{19}=633.6)	21 15.663A (F_{21}=622.9)
1	-	22400 (2800)	8200 (1500)	9400 (2000)	4200 (1400)	9800 (900)	-
2	-	31400 (4900)	7600 (2900)	6400 (2800)	3400 (2000)	8800 (2000)	4200 (1900)
3	-	12100 (2000)	8500 (2000)	6100 (2000)	3200 (1100)	4000 (1100)	1500 (1100)
4	-	1900 (400)	1400 (800)	1200 (800)	2000 (800)	2400 (1200)	2000 (800)
5	800 (400)	1600 (1600)	1200 (400)	1200 (400)	600 (600)	1700 (1200)	1400 (400)
6	-	6100 (1800)	900 (400)	6800 (2000)	2200 (600)	2700 (400)	1500 (400)
7	-	11700 (1900)	18300 (3600)	6100 (1600)	4000 (600)	2900 (2400)	3600 (2000)
8	-	6200 (1200)	800 (400)	4200 (1200)	700 (400)	2000 (400)	700 (400)
9	-	1100 (400)	-	2700 (400)	-	4400 (1100)	600 (400)
10	400 (400)	-	2200 (800)	600 (400)	-	900 (400)	-
11	-	5300 (2000)	3700 (800)	5400 (1600)	2300 (400)	900 (400)	3000 (400)

TABLE XII (Continued)

Pointing Position	24 15.855A (F_{24}=617.3)	27 16.001A (F_{27}=608.2)	28 16.068A (F_{28}=604.1)	29 15.934 (F_{29}=612.8)
1	4700 (600)	71300 (1800)	18800 (2300)	600 (400)
2	4700 (1900)	53300 (4600)	18400 (2200)	-
3	3300 (2300)	28200 (2400)	5500 (1600)	-
4	400	9200 (2300)	1600 (800)	-
5	2800 (1900)	8800 (3300)	1200 (400)	-
6	-	18100 (1800)	2000 (400)	-
7	700 (400)	26500 (3000)	2300 (400)	-
8	-	14300 (1100)	2600 (1500)	-
9	500 (400)	9400 (4400)	3900 (1900)	300 (400)
10	-	9600 (1400)	-	-
11	2200 (1200)	9300 (3800)	5700 (1900)	-

TABLE XIII

26.003 Ne IX Line Intensities (photons/cm^2/sec)

Line Identification

Pointing Position	1(R)	3(I)	5(F)	6	7	8	12
	(13.448Å)	(13.547Å)	(13.698)	(13.784Å)	(13.826Å)	(13.890Å)	(14.031Å)
	(F_1=569.6)	(F_2=564.1)	(F_3=556.4)	(F_6=552.1)	(F_7=550.0)	(F_8=546.9)	(F_{12}=540.1)
1	88300 (5300)	18150 (2400)	53600 (3800)	4250 (1550)	15750 (2350)	4750 (1450)	5450 (1450)
2	61300 (3800)	12900 (1900)	37900 (2950)	3750 (1350)	14600 (1700)	5450 (1400)	6900 (1300)
3	25000 (1600)	5250 (950)	19700 (1850)	2050 (800)	6050 (900)	2200 (750)	1800 (700)
4	7350 (1200)	4700 (900)	4550 (600)	2650 (600)	1700 (300)	1150 (600)	1250 (750)
5	3350 (1050)	1000 (250)	2300 (250)	600	500 (250)	1100 (500)	850
6	12550 (1200)	3450 (550)	7850 (850)	1550 (500)	2400 (550)	900 (550)	1250 (400)
7	25050 (1650)	2700 (700)?	15150 (1250)	1100 (700)	7450 (1000)	1250 (850)	–
8	15350 (1300)	3200 (700)	8500 (950)	1000	2700 (1000)	2800 (1550)	2250
9	4450 (550)	1350 (750)	3650 (500)	700	–	–	–
10	11350 (600)	2050 (300)	7850 (1300)	–	2300	400	850
11	–	–	–	–	–	–	–
Σ	254000	54750	163350				

TABLE XIII (Cont.)

26.003 Ne IX Line Intensities (photons/cm^2/sec)

Line Identification

Pointing Positions	13	16	18	22	23	26
	(14.039Å) (F_{13}=538.3)	(14.195Å) (F_{16}=532.5)	(14.256Å) (F_{18}=529.8)	(14.370Å) (F_{22}=524.7)	(14.401Å) (F_{23}=523.3)	(14.532Å) (F_{26}=577.7)
1	5500 (2750)	21550 (2400)	4850 (1400)	6200 (2450)	5850 (3250)	4900 (1300)
2	4850 (1300)	15100 (1900)	6350 (1400)	6550 (1550)	5700 (1850)	5200 (1400)
3	3150 (750)	7700 (950)	3450 (750)	2600 (650)	950 (300)	3100 (1300)
4	-	1100 (250)	-	750	-	650 (350)
5	1300	1050 (250)	-	-	950	1250
6	1200 (450)	1750 (550)	900 (400)	2100 (750)	550 (350)	1350 (500)
7	-	2800 (700)	2300 (750)	4050 (1900)	-	2650 (600)
8	2550 (1050)	2350 (550)	1450 (600)	1950 (650)	-	2400 (750)
9	-	500	400	-	-	1800
10	500	2000	1200	950	-	2750 (1000)
11	-	-	-	-	-	-

TABLE XIV

26.003 Ne X Scan Line Intensities (photons/cm^2/sec)

Line Identification

Pointing Position	1	Ne X	6	8	9	10	11
	11.548Å	12.132Å	12.261Å	12.403Å	12.430Å	12.599Å	12.682
	F_1 = 431.8	F_5 = 405.1	F_6 = 399.6	F_8 = 397.1	F_9 = 392.7	F_{10} = 386.0	F_{11} = 382
1	10000(1800)	49400(3000)	17300(1300)	2900(1200)	7800(1000)	3350(950)	2900(900)
2	10200(1700)	47500(3100)	19200(2100)	4800(1400)	6500(1500)	3700(1100)	3000(1000
3	4200(1000)	23800(8000)	8800(1700)	4000(700)	4000(700)	1800(000)	2300(1600
4	1700*	7600(800)	4300(500)	900(300)	2000*	800(200)	1500*
5	1200(300)	2900(300)	1500(300)	–	2300(1800)	1100(300)	–
6	1700(600)	8700(2200)	4900(500)	2100(1000)	1300(400)	1000(300)	1400*
7	2400(500)	12900(5100)	6100(3000)	1900(800)	2700(800)	1450(400)	1900(300)
8	–	–	–	–	–	–	–
9	–	–	–	–	–	–	–
10	–	2100(400)	–	–	–	–	–
11	2100*	3300(300)	1500*	350(300)	–	4600*	

* Single value determination

TABLE XV

26.003 Mg XI Line Intensities (photons/cm^2/sec)

Pointing Position	Resonance Line (R) (9.169A)	Intersystem Line (I) (9.232A)	Forbidden Line (F) (9.315A)
	(F_1 = 308.66)	(F_2 = 320.28)	(F_3 = 336.99)
1	9950 (1100)	3550 (800)	10000 (1150)
2	11900 (1150)	3580 (750)	8700 (1100)
3	6500 (600)	2000 (500)	4700 (700)
4	-	-	-
5	1250 (600)	-	1500 (800)
6	2500 (450)	1450 (350)	1950 (500)
7	5350 (600)	1150 (400)	5300 (650)
8	2100 (400)	600 (350)	1500 (350)
9	-	-	-
10	1500 (?)	1150 (?)	2550
11	2100 (300)	850 (300)	1200 (300)
	41900 (5600)	14350 (3800)	35900 (5000)

Table XVI

26.002 Oxygen VII Line Ratios (3' F.O.V.)

Pointing Position	$G = \frac{F + I}{R}$	G	$R = \frac{F}{I}$	R	$\frac{S_3}{R}$	Mean
CTR PRE RL	0.63 (.05)		2.72 (.26)		0.02	
CTR ROLL	0.74 (.07)	0.65(.09)	2.64 (.31)	3.77(1.9)	0.02	0,02 (-)
CTR PST RL	0.57 (.04)		5.95 (.23)		0.02	
MOVE TO 131	0.80 (.03)	-	2.36 (.11)	-	0.01	-
AR 131-1	0.87 (.01)		2.87 (.10)		-	
AR 131-2	0.85 (.01)		3.16 (.10)		0.004	
AR 131-3	0.87 (.02)		3.03 (.06)		0.019	
AR 131-4	0.88 (.03)	0.86(.04)	2.91 (.12)	3.07(.18)	0.005	0.009 (.007)
AR 131-5	0.78 (.05)		3.09 (.11)		0.014	
AR 131-6	0.91 (.03)		3.07 (.10)		0.001	
AR 131-7	0.84 (.01)		2.98 (.08)		0.013	
AR 131-8	0.87 (.03)		3.43 (.15)		-	
MOVE TO 137	0.83 (.05)	-	3.14 (.27)	-	0.005	
AR 137-9	1.09 (.02)		3.14 (.07)		0.011	
AR 137-10	1.12 (.01)		3.19 (.03)		0.009	
AR 137-11	1.15 (.02)	1.10(.03)	3.00 (.02)	3.09(.05)	-	0.009 (.003)
AR 137-12	1.09 (.02)		2.99 (.05)		.005	
AR 137-13	1.09 (.01)		3.14 (.05)		-	
AR 137-14	1.06 (.02)		3.07 (.05)		.012	
AR 137-15*	1.37 (.04)		3.51 (.05)		.020	

* Probably affected by atmospheric absorption.

Table XVII

26.002 Oxygen VII Line Ratios (35" F.O.V.)

Pointing Position	$G = \frac{F + I}{R}$	$\bar{G}$	$R = \frac{F}{I}$	$\bar{R}$
CTR PRE RL CTR ROLL CTR PST RL	0.90 (.42)	-	0.45 (.3)	-
MOVE TO 131	-	-	-	-
AR 131-1	0.66 (.15)		6.11 (.4)	
AR 131-2	1.16 (.21)		3.56 (.5)	
AR 131-3	1.06 (.15)		2.72 (.2)	
AR 131-4	0.86 (.12)	1.03 (.3)	3.04 (.3)	2.64 (1.7)
AR 131-5	1.57 (.53)		1.57 (.4)	
AR 131-6	0.78 (.52)	1.03 (.1)+	1.12 (.8)	3.11 (.4)+
AR 131-7	0.84 (.42)		0.43 (.4)	
AR 131-8	1.29 (.32)		2.60 (.5)	
MOVE TO 137	> .73	-	-	-
AR 137-9	1.42 (.25)		3.04 (.4)	
AR 137-10	0.98 (.49)		1.70 (.7)	
AR 137-11	1.33 (.23)	1.29 (.3)	5.12 (.5)	3.08 (1.2)
AR 137-12	1.01 (.15)		3.67 (.4)	
AR 137-13	1.71 (.77)	1.22 (.2)+	2.25 (.7)	3.81 (1.2)+
AR 137-14	1.32 (.18)		2.65 (.3)	
AR 137-15*	3.25 (.47)		2.20 (.5)	

* Probably affected by atmospheric absorption

\+ 3 Brightest F.O.V.

Table XVIII

26.003 O VII Line Ratios

Pointing Position #	$G = \frac{F + I}{R}$	$\overline{G} = \frac{\Sigma F + \Sigma I}{\Sigma R}$	$R = \frac{F}{I}$	$\overline{R} = \frac{\Sigma F}{\Sigma I}$
1	1.01 (.08)		2.61 (.18)	
2	0.91 (.07)		3.07 (.21)	
3	0.70 (.06)		2.77 (.19)	
4	> .51		-	
5	1.19 (.21)	0.99 (.12)	3.71 (.51)	2.92 (.4)
6	0.91 (.08)		3.04 (.21)	
7	1.18 (.21)		2.96 (.21)	
8	1.23 (.15)		3.28 (.33)	
9	0.75 (.06)		2.50 (.18)	
10	> 0.82		-	
11	> 0.50		-	

TABLE B - XIX

26.002 Ne IX Line Ratios

Position	$G = \frac{F + I}{R}$	$\bar{G}$	$R = \frac{F}{I}$	$\bar{R}$
AR131-1	0.95 (.17)		1.55 (1.6)	
AR131-3	0.75 (.12)		4.69 (1.6)	
AR131-3	0.89 (.11)		4.69 (1.5)	
AR131-4	1.55 (.58)		3.06 (1.0)	
AR131-5	-		-	
AR131-6	-		-	
AR131-7	1.32 (.63)		6.50 (2.4)	
AR131-8	>0.95		-	
AR137	-	1.02 (.16)	-	3.55 (.47)
AR137-9	0.97 (.18)		1.00	
AR137-10	-		-	
AR137-11	>0.68		-	
AR137-12	0.82 (.20)		4.15 (2.0)	
AR137-13	-		-	
AR137-14	1.06 (.13)		4.23 (0.4)	
AR137-15	1.03 (.17)		2.86 (1.3)	

TABLE B - XX

23.003 Ne IX Line Ratios

Pointing Position	$G = \frac{F + I}{R}$	$\overline{G}^{*}$	$R = \frac{F}{I}$	$\overline{R}^{*}$
1	0.81 (.07)		2.95 (.21)	
2	0.83 (.08)		2.94 (.22)	
3	1.00 (.11)		3.75 (.35)	
4	1.26 (.20)		0.97 (?)	
5	0.99 (.15)		2.30 (.25)	
6	0.90 (.11)	0.86 (.09)	2.28 (.25)	2.93 (.25)
7	0.71 (.06)		5.61 (?)	
8	0.76 (.11)		2.66 (.30)	
9	1.12 (.28)		2.70 (.37)	
10	0.87 (.14)		3.83 (.63)	
11	-		-	

* Summing results.

TABLE XXI

26.003 Mg XI Line Ratios

Pointing Position	$G = \frac{F+I}{R}$	$\bar{G}$	$R = \frac{F}{I}$	$\bar{R}$
1	1.37 (.20)		2.80 (0.32)	
2	1.03 (.16)		2.43 (0.31)	
3	1.03 (.19)		2.37 (0.35)	
4	-		-	
5	>1.17		-	
6	1.36 (.34)	1.20 (.21)	1.32 (.34)	2.50 (.35)
7	1.21 (.20)		4.53 (.55)	
8	1.00 (.33)		2.44 (.56)	
9	-		-	
10 (?)	2.43 (.8)		2.23 (.60)	
11	1.00 (.29)		1.40 (.36)	

TABLE XXII

Emission Line Identifications and Wavelengths

Line #	Possible Identification				Measured Wavelength (A)			Published λ(A)	Reference	Oscillator Strength (observed)
	Ion	Transition			λ_1	λ_2	$\bar{\lambda}$			
1	Mg XI	$1s^2\ {}^1S_o$	-	$1s2p\ {}^1P_1$	-	9.173(3)	9.173	9.169,9.18	a,b	0.75*
2	Mg XI	$1s^2\ {}^1S_o$	-	$1s2p\ {}^3P_1$	-	9.235(5)	9.235	9.232,9.22	a,b	0.24(0.06)
3	Mg XI	$1s^2\ {}^1S_o$	-	$1s2s\ {}^3S_o$	-	9.318(3)	9.318	9.315,9.32	a,b	0.59(0.08)
4	Ne IX	$1s^2\ {}^1S_o$	-	$1s3p\ {}^1P_1$	-	11.548(2)	11.548	11.549	a	0.16(0.03)
5	-				-	11.596(5)	11.596	11.600	a	
6	Fe XXII				-	11.760(16)	11.760	11.76	b	
7	Fe XXII	$1s^22s^22p^2\ {}^2P_{3/2}$	-	$2p3d\ {}^2D_{3/2}$	-	11.908(11)	11.908	11.92	b	
8	Ne X	$1s^2\ S_{1/2}$	-	$1s2p\ {}^2P_{1/2,2/3}$	-	12.134(3)	12.134	12.137,12.13	a,b	
9	Fe XVII	$1s^22s^22p^6\ {}^1S_o$	-	$2p^54d\ {}^3D_1$	-	12.260(3)	12.260	12.264,12.262	a,c	0.28(.03)
10	Fe XVII	$1s^22s^22p^6\ {}^1S_o$	-	$2p^54d\ {}^3P_1$	-	12.319(5)	12.319	12.320	c	
11	Fe XVII	$1s^22s^22p^6\ {}^1S_o$	-	$2p^54d\ {}^3P_1$	-	12.403(5)	12.403	12.411	a	0.09(.04)
12	Ni XIV	$1s^22s^22p^6\ {}^1S_o$	-	$2p^53d\ {}^1P_1$	-	12.431(5)	12.431	12.437	a	
13	-				-	12.600(12)	12.600	12.598	a	
14	Fe XVII	$1s^22s^22p^6\ {}^1S_o$	-	$2p^54s\ {}^3P_1$	-	12.683(7)	12.683	12.681,12.681	a,c	0.057(.016)
15	Ne IX	$1s^2\ {}^1S_o$	-	$1s2p\ {}^1P_1$	13.449(6)	13.443(3)	13.445	13.446	a	0.72*
16	Blend Fe XIX, XXI, XVIII				13.501(13)	-	-	13.49	b	
17	Ne IX	$1s^2\ {}^1S_o$	-	$1s2p\ {}^3P_1$	13.555(7)	13.547(3)	13.550	13.551	a	0.15(.03)
18	Ne VIII	$1s^22s\ {}^2S_{1/2}$	-	$1s2p({}^1P)2s\ {}^2P_{1/2,3/2}$	13.663(10)	13.664(4)	13.664	13.660	a	
19	Ne IX	$1s^2\ {}^1S_o$	-	$1s2s\ {}^3S_1$	13.700(6)	13.698(3)	13.699	13.698	a	0.44(.07)
20	Ni XIX	$1s^22s^22p^6\ {}^1S_o$	-	$2p^53s\ {}^1P_1$	13.780(6)	13.784(3)	13.783	13.774	a	
21	Fe XVII	$1s^22s^22p^6\ {}^1S_o$	-	$2p^53p\ {}^1P_1$	13.830(3)	13.826(3)	13.828	13.824,13.820	a,c	0.128(.012)
22	Fe XVII	$1s^22s^22p^6\ {}^1S_o$	-	$2s2p^63p\ {}^3P_1$	13.901(2)	13.890(6)	13.898	13.889,13.887	a,c	0.037(.009)
23	Ni XIX	$1s^22s^22p^6\ {}^1S_o$	-	$2p^53s\ {}^3P_1$	-	14.031(5)	14.031	13.037	a	
24	Fe XVIII	$1s^22s^22p^5\ {}^2P_{3/2}$	-	$2p^4({}^1D)3d\ {}^2D_{3/2}$	14.141(6)	14.133(4)	14.137	14.14,14.150	b,c	
25	Fe XX				14.185(10)	14.195(3)	14.192	14.190,14.19	a,b	
26	-				14.226(4)	-	14.226	14.23	b	

TABLE XXII (Continued)

Line #	Possible Identification: Ion	Possible Identification: Transition	Measured Wavelength (Å): λ_1	Measured Wavelength (Å): λ_2	Measured Wavelength (Å): $\bar{\lambda}$	Published λ(Å)	Reference	Oscillator Strength (observed)
27	Fe XVIII	$1s^2 2s^2 2p^5\ {}^2P_{3/2} - 2p^4({}^1D)3d\ {}^2S$	14.255(10)	14.253(13)	14.254	14.255	c	
28	Fe XV		14.358(10)	14.352(10)	14.355	14.36	b	
29	Fe XVIII	$1s^2 2s^2 2p^5\ {}^2P_{3/2} - 2p^4({}^3D)3d\ {}^2D_{5/2}$	-	14.368(8)	14.368	14.372,14.373	a,c	
30	Fe XVIII		14.409(6)	14.401(10)	14.405	14.40	b	
31	Fe XVIII	$1s^2 2s^2 2p^2\ {}^2P_{3/2} - 2p^4({}^3P)3d\ {}^4P_{5/2}$	14.420(5)	14.426(6)	14.423	14.419	c	
32	Fe XVIII	$1s^2 2s^2 2p^5\ {}^2P_{3/2} - 2p^4({}^3P)3d\ {}^2F$	14.537(2)	14.534(6)	14.536	14.533,14.536	a,c	
33	Fe XVIII	$1s^2 2s^2 2p^5\ {}^2P_{3/2} - 2p^4({}^1D)3d\ {}^2S_{1/2}$	-	14.550(9)	14.550	14.553,14.531	a,c	
34	Fe XVII	$1s^2 2s^2 2p^6\ {}^1S_o - 2p^5 3d\ {}^1P_1$	15.004(3)	15.011(2)	15.009	15.013	a	2.22*
35	-		15.064(6)	15.069(2)	15.068	15.070	a	
36	-		15.098(8)	15.110(4)	15.106	15.105	a	
37	O VIII	$1s^2\ {}^2S_{1/2} - 4p\ {}^2P_{1/2,3/2}$	15.167(3)	15.175(2)	15.171	15.179	a	
38	-		15.200(2)	15.207(2)	15.204	15.210	a,b	
39	Fe XVII	$1s^2 2s^2 2p^6\ {}^1S_o - 2p^5 3d\ {}^3D_1$	15.254(1)	15.260(1)	15.256	15.259,15.261	a,c	0.98(.08)
40	-		15.311(10)	-	15.311			
41	-		15.352(4)	15.357(3)	15.355	15.348,15.35	a,b	
42	Fe XVII	$1s^2 2s^2 2p^6\ {}^1S_o - 2p^5 3d\ {}^3P_1$	15.460(3)	15.457(2)	15.455	15.449,15.453	a,c	0.18(.04)
43	Fe XVIII	$1s^2 2s^2 2p^5\ {}^2P_{1/2} - 2p^4({}^1S)3s\ {}^2S_{1/2}$	15.486(5)	15.490(10)	15.487	15.488	a	
44	Fe XVI		15.513(4)	15.510(5)	15.512	15.513,15.512	a,c	
45	-		15.563(5)	15.556(4)	15.559	15.557	a	
46	-		15.684(2)	15.681(2)	15.682	15.68	b	
47	Fe XVIII	$1s^2 2s^2 2p^5\ {}^2P_{1/2} - 2p^4({}^3P)3s\ {}^2P$	15.773(7)	15.779(10)	15.775	15.78,15.774	b,c	
48	Fe XVIII	$1s^2 2s^2 2p^5\ {}^2P_{1/2} - 2p^4({}^3P)3s\ {}^2P_{3/2}$	15.840(6)	15.832(7)	15.837	15.847	c	
49	O VIII	$1s\ {}^2S_{1/2} - sp\ {}^2P_{1/2,3/2}$	16.056(4)	16.001(2)	16.001	16.000,16.01	a,b	0.10(.02)
50	Fe XVIII	$1s^2 2s^2 2p^5\ {}^2P_{3/2} -$	-	16.068(5)	16.068	16.055,16.073	a,c	
51	O VII	$1s^2\ {}^1S_o - 1s4p\ {}^1P_1$	-	18.490(10)	18.490			
52	O VII	$1s^2\ {}^1S_o - 1s3p\ {}^1P_1$	18.630(5)	18.628(2)	18.628	18.606,18.63	a,b	0.22(.05)

TABLE XXII (Continued)

Line #	Possible Identification Ion	Transition	Measured Wavelength (A) λ_1	λ_2	$\bar{\lambda}$	Published λ(A)	Reference	Oscillator Strength (observed)
53	O VIII	$1s\ ^2S_{1/2}$ - $2p\ ^2P_{1/2,3/2}$	18.970(5)	18.970(2)	18.970	18.950,18.96	a,b	0.42*
54	O VII	$1s^2\ ^1S_o$ - $1s2p\ ^1P_1$	21.602(1)	21.602(1)	21.602	21.58,21.60	a,b	0.69*
55	Blended O VII Satellites		21.650(6)	21.645(5)	-			
56	O VII	$1s^2\ ^1S_o$ - $1s2p\ ^3P_1$	21.805(2)	21.808(3)	21.806	21.78	a	0.17(.03)
57	O VII(33)	$1s^22s\ ^2S$ - $1s2p2s\ ^2P_o$	22.024(5)	22.038(3)	22.032			
58	O VII	$1s^2\ ^1S_o$ - $1s2p\ ^3S_1$	22.113(5)	22.120(4)	22.118	22.07	a	0.47(.10)

Where the references are:

a Parkinson, 1975

b Neupert et al., 1973

c Reader and Sugar, 1975

* Value adopted from Parkinson, 1975 to calculate other members of particular ion stage.

λ_1 is from McMath 12379 and 12387.

λ_2 is from McMath 12664

Uncertainty on measured wavelenghts are in units of 0.001Å.

Appendix 3

Contents

Preprint of a paper on:-

"A Comparison of an X-Ray Scattering Model of the Corona with Observational Results".

By

Keith T. Strong

&

John L. Kulander

June 1979

Submitted to Astrophysical Journal.

Appendix 3

A Comparison of an X-Ray Scattering Model of the Corona with Observational Results

Keith T. Strong
John L. Kulander

Lockheed Palo Alto Research Laboratory
3251 Hanover Street
Palo Alto, California 94304

June 1979

Abstract

We demonstrate that the line intensity ratios of certain He-like ions can exhibit significant variations from the predicted values, and that these observed variations are most probably caused by the scattering of X-radiation in the corona. We develop the equations of radiative transfer for a simple coronal model, and investigate the significance of scattering effects as a function of the basic model parameters such as density, temperature, incident radiation field and orientation of the region to the observer's line of sight. The model is applied to several of the observed situations using the O VII ion as an example, and the results are compared with the data. The agreement is good for the case of the quiet corona where the model is directly applicable to the observations. A discrepency of 27% in the resonance flux is adequately accounted for using the model. The agreement between the model and the active region data is not so convincing. We discuss the reasons for this.

1. Introduction

The highly ionized coronal plasma emits a spectrum that is dominated by soft X-ray emission lines. The most prominent lines originate from transitions of the H-like, He-like and Ne-like isoelectronic sequences of the heavier elements. The physics of the production of these X-ray lines is generally well established as the ions have a simple electronic structure, and the lines have been widely studied both observationally and theoretically (Gabriel and Jordan (1969); Mewe and Shrijver (1978a, b); Bhalla et al (1975); Gabriel and Jordan (1973); Evens and Pounds (1968); Parkinson (1971); Parkinson (1975)). The intensity of such lines and their ratios have been used to derive the fundamental characteristics of the coronal plasma, however implicit in these analyses is the assumption that the X-rays, once emitted, escape from the corona without further interaction with the plasma. That is, the optical depth of the coronal material is negligibly small for any given soft X-ray line. The work presented here challenges this assumption by showing that results derived from observational data indicate variations in certain He-like ion ratios that are attributable to resonance scattering effects in the ambient corona.

Acton et al (1976) have presented observational evidence that the assumption of an optically thin corona is not valid. A subsequent theoretical study (Acton, 1978) has shown, for some lines, that column densities exist in the corona capable of producing observable changes in some X-ray line intensities due to absorption and scattering along the line of sight.

He-like ions are particularly useful for investigating resonance scattering as the resonance line ($1s^2\ ^1S$ - $1s2p\ ^1P$) intensity can be compared directly to the sum of the forbidden ($1s^2\ ^1S$ - $1s2s\ ^3S$) and the intersystem ($1s^2\ ^1S$ - $1s2p\ ^3P$) lines. The triplet lines are forbidden transitions, hence are less susceptible to scattering effects by several orders of magnitude. The resonance

and triplet lines are grouped closely together in wavelength and consequently, can be observed with minimal time or wavelength dependent effects. Because the relative intensities of the forbidden transitions are density sensitive, we have adopted the triplet to singlet intensity ratio (defined by Gabriel and Jordan (1969) as the G ratio) as an indicator of resonance scattering effects,

$$G = \frac{I_I(1s^2\ ^1S - 1s2p\ ^3P) + I_F(1s^2\ ^1S - 1s2s\ ^3S)}{I_R(1s^2\ ^1S - 1s2p\ ^1P)} \qquad (1)$$

As the sum of I_I and I_F is constant with electron density for an equilibrium plasma, any variation in G will indicate a relative weakening or enhancement of the resonance line with respect to the intersystem and forbidden lines. For example, if G were observed to be larger than the expected value then this would be an indication of a relative weakening of the resonance line.

The G ratio shows only a weak dependence on electron temperature. This has been studied by Mewe & Schijever (1978 a,b) and more recently, by Acton and Brown (1978). Acton & Brown take into account in their calculations the contribution from unresolved satellite lines and all excitations to the n=4 levels. Using this theoretical value of the ratio (G_T) and comparing it to an observed value (G_O) provides a measure of the total change in the resonance line intensity, ΔR, required to produce this effect. If the unscattered resonance line intensity is R_T then the observed intensity (R_O) is given by:-

$$R_O = R_T + \Delta R \qquad (2)$$

It follows that if the forbidden and intersystem lines remain unaffected by the scattering process then ΔR is given by:-

$$\Delta R = R_o \frac{(G_T - G_o)}{G_T} \qquad (3)$$

A positive value of ΔR would indicate a net increase in the resonance line intensity, where as a negative value would indicate an overall loss of radiation due to scattering out of the line of sight. It is not possible to directly express the optical depth of the region in terms of ΔR as it is a result of several counteracting factors. There will be a loss term due to absorption along the line of sight. However, this can be counteracted by contributions to the radiation field from any sources of emission, including the ambient corona plasma and nearby active region emission not included in the field of view.

In the work presented here, we furnish conclusive evidence for significant variations in the G ratios of He like ions. In the next section this data is interpreted in terms of resonance scattering following the work of Acton & Brown (1978). In the subsequent section a simple coronal model is developed taking into account the geometry dictated by the angular redistribution function introduced by resonance scattering. This model is applied to the data for comparison. In the last section, we discuss some possibilities of using this technique as a diagnostic tool in the interpretation of coronal plasmas.

2. The Data

In 1973 the Lockheed Palo Alto Research Laboratory flew two sounding rocket experiments that carried an array of six collimated Bragg Crystal Spectrometers. Several of these spectrometer systems monitored the emission from helium-like ions in the soft X-ray part of the solar spectrum. The payloads had the capability to change their pointing positions under direct experimenter control. Hence, a series of raster type scans were executed over areas of active regions and quiet corona.

The first flight, Aerobee 26.002, was on 11th June, 1973, at 18:30 UT. It took data at a total of 20 pointing positions over the disk. The three primary regions observed were: a region of quiet corona near the disk center, McMath 12379 and McMath 12387. McMath 12379 was a fairly quiescent active region near the disk center at the time of launch. A total of nine observations were made in and around this region. McMath 12387 had just appeared over the eastern limb and seemed to be a more complex region. A total of eight observations were made of this region. Three spectrometers on this flight were dedicated to monitoring He-like ions. The first was an instrument with a wide field of view (150" FWHM), which observed the O VII system at 21.6Å, 21.8Å and 22.1Å. A second instrument monitored this system with higher spatial resolution (35" FWHM). The other detector observed the Ne IX system at 13.44Å, 13.55Å, and 13.70Å at the higher spatial resolution (35" FWHM).

The second flight, Aerobee 26.003 took place on 19th December, 1973, at 22:07 UT. It took data from eleven stable pointing positions in and around McMath 12664. This was a very active region prior to the flight, producing a series of flares and subflares. Again three instruments observed He-like ions, but all at a spatial resolution of 35" (FWHM). As for 26.002, the O VII and Ne IX ions

were monitored, the additional ion on this flight was Mg XI at 9.17Å, 9.24Å and 9.32Å. A more detailed description of the payloads is given by Strong and Acton (1979) and a detailed description of the data reduction techniques is given by Strong (Thesis, 1978). Four sample spectra are shown in Figure 1.

Using line intensities derived from these data, the G ratios were calculated and are listed in Table 1. The uncertainties, shown in parenthesis, are derived from the uncertainties in the individual line intensities obtained in the data reduction processes. They probably tend to be pessimistic. This is especially true in the case of the G ratios where we are calculating the ratios of lines observed by the same detection system and at similar wavelengths. Hence, a ratio of such lines will eliminate absolute calibration errors and reduce to a minimum any wavelength dependent effects. The mean values, which are mainly used in the subsequent calculations, are derived from the sum of the individual line intensities over a given region.

The O VII results show significant variations from one region to another. The wide field of view data demonstrate the consistency of the ratios within a region due to the integrating effect of a large field of view. The 35" field of view O VII observations show larger fluctuations, which are probably caused by a combination of reduced statistical reliability of the line intensities and genuine variations due to changes in the coronal structures within the various fields of view. The quiet corona has a lower value of G than any of the active regions. There is an overall indication of an increase in the G ratio with a decrease in the size of the field of view. This effect is only just within the resolution of the data so caution must be exercised in assigning much significance to it but a possible explanation is discussed later. The Ne IX results do not show any significant variations outside the experimental uncertainties.

Table 2 summarizes the average properties for each region for the O VII results. The effective temperatures were calculated from the relative intensities of the brightest lines observed. The calculations assumed a state of dynamic equilibrium existed in the emitting plasma. Although these can only be considered to be approximate values (± 0.3 10^6 ^oK) the insensitivity of the G ratio to temperature renders this uncertainty in temperature to be unimportant. The electron temperature of the quiet corona was found to to be 1.9 10^6 ^oK. The active region temperatures are typical of those calculated for similar regions from other X-ray data. Using these effective temperatures the expected G ratios were calculated from Acton and Brown (1978). The agreement is very poor for all the results, none of them falling within the uncertainty of observation.

Alternatively, if we assume that the observed G ratios were caused purely by temperature effects, it is possible to use the ratio to give an indication of the temperatures of the regions. The results of this approach are also listed in Table 2. This gives the unrealistic result that the quiet corona is at a temperature of 6.10^6 ^oK, and is considerably hotter than active regions.

Both Mewe and Schrijver (1978a,b) and Acton and Brown (1978) discuss non-equalibrium plasmas. These can cause changes in the G ratio. However, it would seem unlikely that all three active regions were in a state of recombination (especially McMath 12379 and 12387). The quiet corona would have to be in an ionizing state to account for the observations. The O VIII to O VII line ratios are consistent with equilibrium values for electron tempratures of 3.5 (± 0.5) 10^6 ^oK for each active region observation. If we were to use the sum of the triplet lines to derive the temperature instead of the observed resonance intensity then this temperature would be lower. There is, consequently, no observational justification for assuming non-equilibrium conditions.

We suggest, in the absence of a viable alternative, that the observed variations are due to perturbations of the observed resonance line intensity due to scattering of X-rays in the corona. We will subsequently investigate this contention, and see if it is viable for a set of reasonable coronal conditions. Using (3) it is possible to calculate the change in the resonance line intensity required to produce the observed effects. In order to increase the G ratio to the levels measured in the active regions, the resonance line intensity has to have been reduced by between 10-42%. Perhaps even more surprising is that the resonance line has to undergo an enhancement of 37% from its theoretical value to reproduce the observations for the quiet corona. This is, potentially, a difficult result to reproduce from a model, as the region is supposedly of low density, and consequently less subject to scattering effects.

In order to investigate resonance scattering as a viable explanation of these effects, we choose to model the quiet corona case for several reasons. Firstly, as mentioned above, it is the most difficult region in which to get a measurable effect. Secondly, it is a fairly simple problem geometrically, at least in comparison with the complex loop structures associated with active regions. Also, it is a region which is likely to be in equilibrium, stable, and could provide the simplest tests of the effect for future observations.

Results from other spectrometers flown in recent years also indicate variations in the G ratio, these are listed in Table 3. These show variations in the O VII G ratio similar to those of 26.002 and 26.003. The Ne IX G ratios seem to show some significant variation when compared to the quoted errors. A quite interesting result is that for Mg XI which shows a very large change for McMath 12624. This region was associated with a flare at the time of observation, hence the low G value is possibly associated with an ionizing plasma rather than a significant scattering effect.

3. The Model

We shall assume the corona to be represented by a spherical shell of inner radius R_1 and outer radius R_2 with uniform temperature and density throughout. Our coordinate system, which is shown in Figure 2(a), places the center of the sun at (0,0,0) and the observer at the Earth on the +Z axis. An X-ray point source, S, is located at arbitrary position (x_s, y_s, z_s) within the shell. The emission from the surface in the direction Z from a column C with coordinates (x_c, y_c) as seen by the observer will be calculated. The coronal plane (X,Y) at Z=0 as seen by the observer is shown in Figure 2(b). Since there is rotational symmetry in this plane, we arbitrarily place the point source on the +Y axis. There is also symmetry about the Y axis so that we need only consider positive values of x_c.

The radiative intensity from column C consists of three contributions: (1) thermal emission from the quiet corona within the column, (2) radiation from the source, S, that is absorbed within C and is scattered in the z direction and (3) radiation emitte from the surrounding quiet corona, absorbed within C, and scattered in the z direction. As the optical depth of the column approaches zero so will the scattered contributions.

The formulation of the radiative transfer equation for X-rays in the solar corona has been considered by Acton (1978) and we shall make use of his results. We shall consider the line absorption profile ϕ_ν to be Gaussian, i.e.:

$$\phi_\nu = e^{-\nu^2}/\sqrt{\pi}\,\Delta\nu_D \tag{4}$$

where $\nu = (\nu-\nu_o)/\Delta\nu_D$, $\Delta\nu_D = \frac{1}{\lambda_o}\sqrt{\frac{2kT}{M}}$ (5)

ν_o and λ_o are the line frequency and wavelength, $\Delta\nu_D$ is the Doppler half width, T is the temperature and M is the ion mass.

ϕ_ν is normalized such that

$$\int_0^\infty \phi_\nu \, d\nu = 1 \tag{6}$$

The line center absorption coefficient for resonance lines is given by:-

$$\kappa_o = \frac{\sqrt{\pi} e^2 f n_o}{mc \cdot \Delta\nu_D} \tag{7}$$

where e and m are the electron charge and mass, c is the speed of light, f the absorption oscillator strength and n_o is the ion ground state number density. The line center optical depth, τ_o is $\tau_o = \kappa_o \ell$ where ℓ is the path length. It is also convenient to define a mean absorption coefficient $\bar{\kappa}$ by:-

$$\kappa_\nu = \bar{\kappa} \phi_\nu \tag{8}$$

The general solution of the transport equation for the specific intensity I_ν is:-

$$I_\nu (z) = \int_o^z S_\nu(z') \, e^{-\tau_\nu(z,z')} \, \kappa_\nu (z') \, dz' \tag{9}$$

where z is the depth coordinate, κ_ν the absorption coefficient, S_ν the source function and the optical depth τ_ν is defined

$$\tau_\nu(z,z') = \int_{z'}^{z} \kappa_\nu (z') \, dz' . \tag{10}$$

The source function can be divided into thermal and scattered emission parts

$$S_\nu = \frac{\varepsilon_\nu + \varepsilon_\nu^s}{4\pi\kappa_\nu} \tag{11}$$

where ε_ν and ε_ν^S are the thermal and scattering emission coefficients, respectively. Assuming complete frequency redistribution for the scattered photons the solution to the transport equation along the Z axis becomes (Acton, 1978).*

$$I_\nu = \frac{1}{4\pi} \int_{-\infty}^{+\infty} \left\{ \left[\frac{\varepsilon_\nu}{\kappa_\nu} + \int_0^\infty \int_0^\pi \int_0^{2\pi} \psi(\theta) \sin\theta \mathcal{I}_\nu^Q, (\eta,\theta) d\eta d\theta d\nu' \right. \right.$$

$$\left. \left. + \int_0^\infty \psi(\theta) \mathcal{I}_\nu^S, (\eta, \theta) \; d\nu' \right] \right\} e^{-\tau_\nu(z)} \kappa_\nu \, dz \qquad (12)$$

where $\psi(\theta)$ is the angular redistribution function upon scattering and $\mathcal{I}_\nu^Q$, and $\mathcal{I}_\nu^S$, are the incident intensities at the scattering volume in column C from the quiet corona and point source. θ is the polar angle between photons incident upon column C and the Z axis, while η is the azimuthal angle between the incident photon and X-axis. These three terms represent the components discussed above. For the type of atomic transitions considered here ($j=0$, $\Delta j=1$) the redistribution phase function is identical to that for Rayleigh scattering, i.e.,

$$\psi(\theta) = 3/4 \; (1 + \cos^2 \theta). \qquad (13)$$

The function $\mathcal{I}_\nu^C$, due to emission from the quiet corona surrounding C is given by:-

$$\mathcal{I}_\nu^Q, (\eta,\theta) = \frac{1}{4\pi} \int_0^{d_C} \varepsilon'_\nu, (\eta,\theta,t) \; \phi'_\nu, (\eta,\theta,t) \exp\left[-\int_0^t \kappa_\nu', (t) dt\right] dt \qquad (14)$$

where t is distance measured along the incident photon direction from 0 at the volume element of C under consideration to the edge of the corona, d_C. With uniform conditions in the corona $\mathcal{I}$ for a volume element at distance z

*(Acton's Eq. 30 is in error by a factor of $1/4\pi^2$ in the second term. Also all his preceding equations for ε_ν^S should be multiplied by 4π).

along the z axis reduces to:

$$\mathcal{J}^{Q}_{\nu'}(\theta,z) = \frac{\varepsilon_{\nu'}}{4\pi\bar{\kappa}} \left(1 - e^{-\kappa_{\nu'} d_c}\right). \tag{15}$$

Due to the symmetry of the problem, $\mathcal{J}$ is not a function of η. Since we anticipate the optical thicknesses to be encountered in the corona at resonance line centers generally to be less than 1 it is convenient to expand $e^{-\tau}$ in a power series to be able to integrate Eq. 12 in closed form. The functions f_o, f_1, and f_2, which will appear in the subsequent equations, represent the series expansion in combination with ϕ_ν and ϕ_ν^2. Performing the η and ν' integrations now gives for the quiet corona scattering term in Eq. 12.

$$\frac{\varepsilon}{2} \int_{R_1}^{R_2} \left[\int_{\theta=0}^{\pi} \psi(\theta) \sin\theta \, d_c(\theta) \, f_o(\theta) \, d\theta \right] \phi_\nu \, e^{-\kappa_\nu (R_2 - z)} \, dz \tag{16}$$

where ϕ_ν, $\varepsilon = \varepsilon_{\nu'}$.

For comparison with the observations we require the frequency integrated emitted intensity $\bar{I} = \int_{-\infty}^{+\infty} I_\nu \, d\nu$. Expanding $e^{-\kappa_\nu (R_2 - z)}$ in a power series for $\kappa_\nu (R_2 - z) < 1$ and integrating over ν we find we can replace $\phi_\nu \, e^{-\kappa_\nu (R_2 - z)}$ in Eq. 16 integrated over ν by $f_2(z)$.

The total amount of energy absorbed by any particular coronal volume element from the rest of the quiet corona is identical for coronal elements at the same radius from the center. Hence, for purposes of calculation of scattering from the quiet corona emission, we place the column C at the X = 0, Y = 0 position. When the incident photon direction is tangent to the sphere R_1, the angle θ, which we call θ_m, is given by:

$$\theta_m = \arcsin (R_1/z). \tag{17}$$

For $\theta < \theta_m$ the distance d_c is the distance to the sphere R_2 while for $\theta > \theta_m$, d_c is the distance to the sphere R_1. The amount of quiet corona radiation scattered by a volume element at radius r into an angle θ_s from the outward radius vector is:

$$\frac{\varepsilon}{2} - \left\{ \int_0^{\theta_m} \psi_s \sin\theta \, d_2 \, f_o \, d\theta + \theta \int_m^{\pi} \psi_s \sin\theta \, d_1 \, f_o \, d\theta \right\} \phi_\nu \tag{18}$$

where

$$d_1 = z \cos\theta + \sqrt{R_1^2 - z^2 \sin^2\theta} \tag{19}$$

$$d_2 = -z \cos\theta + \sqrt{R_2^2 - z^2 \sin^2\theta} \tag{20}$$

In order to obtain the quiet corona scattered intensity we integrate the contribution function from (18) along C with the appropriate r, θ_s and θ_m for each volume element.

For a point source of intensity I_s' located at x_s, y_s, z_s the function $\mathcal{I}^s$ can be written

$$\mathcal{I}^s = I_s' \, \phi_\nu, \exp [- \kappa_\nu, d_s] \tag{21}$$

where d_s is the distance between a point on column C and the point source. Letting $I_s' = I_s \, \phi_\nu$, and integrating over ν' we find

$$\int_0^{\infty} J_s \, d\nu' = I_s \frac{f_1}{\kappa} \tag{22}$$

After integrating over outgoing frequency, the point source scattering term in the transport equation now becomes,

$$\frac{3I_{so}}{4(4\pi)} \int_{z_B}^{z_A} \left[d_s^2 + \frac{(z_s - z)^2}{d_s^4} \right] f_1(z) \, f_2(z) \, dz. \tag{23}$$

where $I_s = I_{so}/4\pi d_s^2$, and I_{so} is the total source strength.

The upper limit of integration z_A is the intersection of the column with the outer shell and the lower limit z_B is the intersection with the inner shell. z_A and z_B are given by:

$$z_A^2 = R_2^2 - r_c^2 \tag{24}$$

$$z_B^2 = R_1^2 - r_c^2 \tag{25}$$

where $r_c^2 = x_c^2 + y_c^2$

For many configurations the entire length of the column C is not illuminated by the point source as the source is cutoff by the shadowing of the inner shell. In this case, as illustrated in Figure 2(a) the lower limit of integration becomes z_T defined by the intersection of the line tangent to the shell R_1 from the source with the column C. Appropriate expressions for z_T have been derived and applied in the calculation.

A complete solution can be obtained by moving the point source along the positive Y axis and calculating the emitted intensity for all $x > 0$.

The expression for the integrated emitted intensity now becomes:

$$4\pi\,\bar{I}\,(x_c,y_c) = \varepsilon \int_{z_B}^{z_A} f_2\,dz + \frac{\varepsilon}{2} \int_{z_B}^{z_A} \left\{ \int_{\theta}^{\theta_m} \psi_s \sin\theta\, d_2\, f_o\, d\theta \right.$$

$$\left. + \int_{\theta_m}^{\pi} \psi_s \sin\theta\, d_1\, f_o\, d\theta \right\} f_2\,dz + \frac{3I_{so}}{4(4\pi)} \int_{z_T}^{z_A} \frac{[d_s^2 + (z_s - z)^2]}{d_s^4}\, f_1\, f_2\,dz \qquad (26)$$

$$= 4\pi \left\{ (\bar{I} - \delta\bar{I}) - \delta\bar{I}_S - \delta\bar{I}_B \right\}$$

where the first term is the thermal emission emitted directly from $C(x_c,y_c)$, the second term is quiet corona radiation scattered by C and the third term is radiation from the point source scattered by C. See Figure 2(a).

IV. Numerical Results for O VII

As discussed above the observed X-ray signal from our model corona consists of three components: (1) direct thermal emission from the point source and the column of corona under observation; (2) scattered radiation from the point source and (3) scattered radiation from the quiet corona. The major physical dependencies are as follows: Component (1) is a function of ε; component (2) is a function of κ_o; and component (3) is a function of ε and κ_o. The X-ray signal from a one cm^2 column of corona is shown in Figure 3 as a function of radius from the disc center. For the quiet corona we assume $T_e = 1.9 \quad 10^6\ ^oK$ and $n_e = 2.4 \quad 10^8$. The increase in components (1) and (3) from center to limb basically results from the increase in length of the column C. Component (3) has a relatively larger increase between center and limb as the average scattering angle becomes more favorable along with the increased column length. At the limb, $r = R_1$, the values essentially double as we "see" through a double length of corona. Component (2) is illustrated by point sources located on the R_1 surface at various distances r_s from disc center (z-axis) with $I_{so} = 10^{34}$. The intensity falls off as $1/r^2$ from the source.

Figure 4 illustrates the scattered radiation from elements at different heights, R, in the quiet corona as a function of the angle, θ, between the radius vector to the element and the line of sight. These variations are equivalent to a change in the observed scattered signal (in arbitrary units) as the element moves with respect to the central meridian (θ=0). When the scattering element is located at the base of the corona ($R=R_1$) only a relatively small proportion of the atmospheric shell is above the local horizon and able to contribute to the radiation field at the element, 4(a). As R increases, the volume of corona visible from the scattering element increases and therefore so does the signal in general. The maximum "visible" volume in close proximity to the scattering element occures for $R \sim (R_1 + R_2)/2$ which is where the maximum signal occurs, 4(b). The maximum angular scatter for each R occurs in the direction in which the largest

fraction of photons are incident. For $R = R_1$ this angle is slightly less than $\pi/2$, while for $R = R_2$ the angle is slightly greater than $\pi/2$. As we would expect in light of the phase function, the corresponding intensity minima are found $\pi/2$ away from the maxima.

Fig. 5 illustrates the disc center signal variations with electron density for electron densities between $8 \quad 10^7$ and $8 \quad 10^8$. The temperature is held fixed at $1.9 \quad 10^6$ ^oK with $R_2 - R_1 = 10^{10}$ cm. The scattering column is located at a point one arc minute from the disk center source region. The point source scattering is dependent only upon the line absorption coefficient which varies linearly with n_e. The thermal emission varies as n_e^2 in direct proportion to the volume emission coefficient. The quiet corona scattered signal is proportional to both the thermal emission coefficient and the line absorption coefficient and hence varies as n_e^3. In all cases the curves are not linear due to optical depth effects. The observed source G ratio is also shown in Fig. 5.

The line absorption coefficient varies as $T^{-\frac{1}{2}}$. Since the scatter of a particular point source depends only on the absorption coefficient, this scattered signal decreases as the temperature increases. This effect is shown in Fig. 6 where we also show the variation of the other components and the G ratio. The volume emission coefficient increases with T and hence so does the thermal emission. The quiet corona scattered component is the product of the above two dependences.

We combine the above effects to produce the contour plots shown in Figure 7. In order to illustrate the relative importance of the scattered components in the observed O VII resonance line signal we define a quantity, Δ, such that,

$$\Delta = \left(\frac{R_O}{R_T} - 1 \right) \tag{27}$$

where R_o and R_T are the total predicted and thermal fluxes in the resonance line respectively. This particular form of Δ is chosen as it readily demonstrates the variation of the scattered signal as a function of ambient thermal signal, and its sign indicates whether scattering into or out of the line of sight is dominent at any given location. We show four distinct cases for different source positions, from the disk center (7a) to the limb (7d). The value of delta obtained by observing the source directly is denoted by Δs, and is primarily determined by the column length of overlying quiet coronal material. Δs is negative which indicates a net loss of resonance line radiation. The contours are plotted at suitably spaced values of Δ in the X-Y plane, on a scale of a unitary solar radius. The limit of the irradiated volume of corona by the source is indicated by a broken contour. The choice of appropriate model parameters is discussed at length in the next section.

Figure 7a shows the source at the disk center (0,0). This case has complete symmetry in X and Y directions. For a source at the base of the corona Δs is -0.14. Otherwise on the solar disk Δ is positive indicating a net addition of scattered radiation along any given line of sight. Immediately above the limb, where an extended column of plasma is present along the line of sight, Δ becomes negative, but as we look higher in the atmosphere Δ tends to zero as the column becomes shorter. As the distance of the source from the disk center increases so does the depth of the overlying ambient corona, hence Δs becomes more negative until it reaches a limiting value of -0.43 at the limb. The symmetry is maintained along the X direction but not along the Y direction as the columns available to scatter equidistant from the source in the ordinate are different. They are longer being further from the disk center due to the curvature of the sun, hence will give rise to a greater scattered signal. As the so

approaches the limb the negative contours above the limb become distorted (7c), until finally when the source is at the limb (7d) the effect of the opaque inner shell becomes apparent producing a sharp horizon effect. Below the source horizon the optical depth effects keep Δ negative as in the first case 7a) where as within the sphere of influence of the source Δ is primarily positive due to radiation being scattered into the line of sight from the source. In reality one would not expect such a distinct boundary for the source horizon especially if the source region, assuming it to be an active region, is extended and not at the base of the corona. However, these models may be used to determine the gross characteristics of scattering in the corona.

Section V. Comparison of the Scattering Model to Observations

The problem that arises in applying this model to the observations cited in section II lies in the physical parameters to be adopted to represent the active region and quiet corona without predisposing the result. The quiet coronal temperatures can be derived from the relative intensity of the X-ray emission lines observed by the 26.002 spectrometers. It is 1.9 (±.2) 10^6 ^oK (Strong, 1978). From the predicted intensity of the O VII resonance line, calculated from the triplet lines and the expected G for that temperature, the emission measure required to give the observed flux can be estimated. Knowing the size of the field of view, it is possible to derive a quantity that is the emission measure along the line of sight for a column of 1 cm^2 cross-section. This has a value of 5.8 10^{26} cm^{-5}. A family of heights and densities can be adopted that would reproduce this value. It should be noted that this quantity is particularly sensitive to density; halving the density would require a four-fold increase in the extent of the atmospheric shell. Hence, the choice of a representative height for the shell would restrict the density to a relatively narrow range of values. On the basis of the extent of limb brightening on soft X-ray photographs, and the variation of coronal density and temperature with height (Allen, 1973), we adopted a value of 1.10^{10} cm. This determines the electron density to be 2.4 10^8 cm^{-3}. This also determined both the emission and line center absorption coefficients to be 72 photon/cm^3/sec and 1 59.10^{-10} cm^{-1} respectively. This model corresponds to an emission measure of 4.10^{49} for the general corona and compares favorably with other determinations which lie between 3.4 - 4.4 10^{49} (Allen 1973; Acton et al., 1972).

Aerobee 26.002 took observations of both active regions and the quiet corona. The quiet coronal G ratio for O VII (0.63) is low compared to the theoretical value derived from the observed temperature (G = 0.86-.88). The observations also give the position, temperature and emission measure of the major region near this field of view, from these data it is possible to reconstruct an equivalent point source intensity for McMath 12379 of 6.0 10^{32} photons/cm^2/sec/st. The coordinates of the active region, along with those of the pointing position for the quiet corona observations, were known from the aspect solutions of the rocket, and confirmed from Hα photographs. The source was put at a height of 5 10^9 cm in the atmospheric shell based on the size of the loops structures derived from ATM photographs taken in the X-ray and EUV spectral regions of McMath 12379.

We have defined a quantity, Δ, which reflects the importance of scatter at any position in X and Y. The case under consideration above is closely represented by Figure 7b. To explain the observations of the quiet corona made by Aerobee 26.002, Δ would have to have a value of 0.27 (±0.11). This model predicts a value at the required position of Δ = 0.25 using the above model parameters. This demonstrates that scattering can be a significant phenomenon in the ambient corona and that its magnitude is sufficient to explain observed changes in line ratios such as the G ratio. The ability of this simplified model to predict the observed change in the resonance line flux and consequently the anomalous G ratio for the quiet corona observation is very encouraging, especially without any adjustment of the model parameters from their independent values. Although the scattered signal is density sensitive, any change in density would have to be accompanied by a corresponding change in the extent of the atmospheric shell to maintain the emission measure constant. These

opposing effects will tend to compensate for one another making the model less sensitive to changes in density. Figure 8 shows the variation in the predicted Δ with a change in the extent of the corona while maintaining the total emission measure (hence the observed flux) at a constant value. It can be seen that the model is relatively insensitive to such changes in comparison to the uncertainty on the observed value of Δ.

The question remains as to whether scattering effects from the quiet corona are responsible for the deviations in the observed active region G ratios. Figure 9 shows the results of the calculation of the source region G ratio as a function of the radial position of the source. The source is assumed to be at the base of the atmosphere. The G ratio rises rapidly as the source nears the limb and then falls as the source is moved higher in the atmosphere above the limb. These effects are due to the change in the length of the column of quiet coronal material along the line of sight to the source. We assume the source G ratio to be 0.75 without scattering. Plotted on this graph are the G ratios derived from the large field of view data (150" FWHM) from 26.002 for both active regions. While neither groups of points lie exactly on the curve the general trend is in good agreement. Adjusting the curve to fit either data set more closely by changing the quiet corona density, for example, will result in a poorer fit to the other data. The small field of view ratios do not show such a good correlation but the uncertainties and fluctuations are too large to draw any firm conclusions in this respect. However, the mean values over each region show a similar trend to that of the large fields. The fact that these observations do not fit is probably caused by the assumption of a point source and that it is assumed to be optically transparent to the O VII radiation. This will not be the case, and the emergent radiation from the dense active region loops might give a different G ratio for O VII that the value of 0.75 assumed above due to scattering within the loop structure.

As noted in Section II, the larger fields of view tended to show a lower value for G. This could be due to either the inclusion of an increasing amount of quiet corona emission (with a different G ratio characteristic of its temperature) or including a proportionally larger amount of scattered signal. We investigate these effects in Figure 10, where they are contrasted. The source is placed at the disk center and the field of view observes the source directly. As the full width at half maximum (FWHM) of the instrument is increased, the resulting G ratio is calculated with and without scattering effects included. The model parameters are as above for the quiet corona. The source intensity is a variable, and the source is at the base of the corona.

For the no scattering case the G ratio is seen to increase as a function of the field FWHM at a rate that is related to the source intensity (solid curves). This is due to the increase in the proportion of the signal from the low temperature quiet corona which has a higher G ratio. With scattering effects also included, the G ratio drops as the FWHM increases as is shown by the broken curve, again the rate is in proportion to the source brightness. The starting value of G is determined by the column of overlying quiet corona, for this case ($R_s = 0$) it would give a value of 0.88 for G. If the source were at the limb starting value of G would be 1.35. The source brightness is assumed to be 10^{34} phts/cm^2/sec. The reuslts are compared to the data from McMath regions 12379 and 12387 where we have two spatial resolutions available. The overall trend of the observations confirm the scattering model over the non scattering model. However, this effect is marginal in these data and caution should be exercised in interpreting these results.

VI. Concluding Discussion

We have presented the observed G ratios of several helium like ions originating from a large number of discrete pointing locations over the solar corona. We have noted that the ratios have a large spread of values, and that the anomalous variations are too large to be explained in terms of the statistical fluctuations in the data or from physical differences in the emitting plasma, such as in temperature or equilibrium balance. We conclude that scattering of X-radiation in the corona is responsible for the observed variations. We, then, investigate this supposition by developing a simple coronal model and applying it to the observed situations for the O VII results. The major variations are observed in O VII, which would be expected as this ion is the most susceptible to radiative transfer effects at coronal temperatures.

The radiative transfer code developed during this work takes account of the Rayleigh angular redistribution function and the geometrical factors associated with the model. The atmosphere is assumed to be an isothermal homogeneous shell. The thickness, density and temperature of this shell may be changed independently. A point source of arbitrary brightness can be placed at any coordinate and height within the shell. The relative contributions from the thermal emission from the source and quiet corona are calculated as seen by the observer over a matrix of points. These represent the signal that would be expected from each element if there were no scattering. The scattered signal from the source and surrounding ambient corona is also computed. This can be a positive or negative quantity depending whether there is a net loss or gain of resonance line radiation. If there is a net gain of resonance flux, for example, then the G ratio would be depressed compared to its theoretical value.

We use the model to determine the sensitivity of the scattering mechanism, and consequently the G ratio, to physical parameters of the plasma. We apply the model to the problem of a volume of ambient corona illuminated by a nearby active region. The temperature, density and extent of the observed region, as well as the source brightness, were derived independently of the model. In this case, the predicted scattered signal from the model agreed well with the requirement from the observations. The result was insensitive to the detailed form of the model. However, an attempt to interpret the active region observations using this model were not as convincing as the previous case. However, the basic trends in the observed G ratios are reproduced by the model. We believe the discrepency to be due to the inadequacy of the assumption of the source region being a point source and that it emits radiation characteristic souly of its temperature, i.e. a G ratio of 0.75. This assumption is equivalent to presuming that there is no scattering within the active region itself, which will probably not be correct. A study is underway to investigate the problem of scattering within active region loops. In this case, the geometry will be the dominant factor, but it will help us to understand the observations from the higher spatially resolved data, where individual structures become important.

The phenomenon of resonance scattering with its sensitivity to density, may be a useful diagnostic tool in the future. Conclusive evidence for its presence in the corona could be furnished by the detection of a polarized component in the observed X-ray line intensities. Where-ever there is an anisotropy in the radiation field, as would be provided by a nearby source region, then the emergent radiation would be partially polarized. As the crystals used in Bragg crystal spectrometers produce a polarizing effect a change in the aspect of the instrument with respect to the sun will modulate the observed signal. This would be observable given a sufficiently sensitive instrument.

In conclusion, we believe that resonance scattering is an important mechanism in the solar corona, at least for some X-ray emission lines. This should sound a note of caution when using X-ray line intensities to derive models of the coronal plasma. These results show that substantial errors can be introduced in some situtations if the optical depth of the medium and its geometry are not taken into account.

Acknowledgements

We would like to thank Drs. L.W. Acton, C.J. Wolfson and J. Pye for some useful discussions during the course of this work. Our appreciation also goes to D.T. Roethig for his assistance with the computer programming. This work was supported by the National Aeronautics and Space Administration under contract NAS8-33195 and by the Lockheed Independent Research Program. The authors have benefitted from the exchange of views made possible at the meetings of the Skylab Solar Workshop Series on Active Regions. The workshops were sponsored by NASA and NSF, and managed by the High Altitude Observatory, Boulder, Colorado.

References

Acton, L.W., Catura, R.C., Meyerott, A.J., Wolfson, C.J., and Culhane, J.L., 1972, Solar Phys., 26, 183.

Acton, L.W., and Catura, R.C., 1976, Phil. Trans. Roy. Soc. London, A, 281, 383.

Acton, L.W., and Brown, W.A., 1978, Ap. J., 225, 1065.

Acton, L.W. 1978, Ap. J., 225, 1069.

Allen, C.W., "Astrophysical Quantitites", Third Edition, 1973.

Gabriel, A.H., and Jordan, C., 1969, M.N.R.A.S., 145, 241.

Jordan, C. 1966, M.N.R.A.S., 132, 4, 463.

Jordan, C. 1969, M.N.R.A.S., 142, 4, 501.

Jordan, C. 1970, M.N.R.A.S., 148, 1, 17.

Mewe, R., and Schrijver, J. 1978a, Astr. Ap.

_____ 1978b, Astr. Ap.

Parkinson, J.H. 1971, Thesis, University of Leicester

Parkinson, J.H. 1973, Astron. Astrophys., 24, 215.

Parkinson, J.H. 1975, Solar Physics, 42, 183.

Strong, K.T., 1978, Thesis, University of London.

Strong, K.T. and Acton, L.W., 1979, in preparation.

TABLE 1. Observed G Ratios of He-like Lines in Coronal Spectra.

Pointing Position Label	O VII 150" FWHM	O VII (35" FWHM)	Ne IX (35" FWHM)	Mg XI (35" FWHM)
Aerobee 26.002				
CTR PRE RL	0.62(.05)	-	-	-
CTR RL	0.72(.07)	-	-	-
CTR PST RL	0.56(.04)	-	-	-
Mean Quiet Corona	0.63(.07)	0.89(.40)	-	-
Move to McMath 12379	0.79(.03)	-	-	-
AR131-1	0.85(.01)	0.65(.15)	0.95(.17)	-
AR131-2	0.83(.01)	1.13(.20)	0.75(.12)	-
AR131-3	0.86(.02)	1.03(.14)	0.89(.11)	-
AR131-4	0.86(.03)	0.84(.12)	1.55(.58)	-
AR131-5	0.77(.05)	1.54(.51)	-	-
AR131-6	0.89(.03)	0.77(.49)	-	-
AR131-7	0.82(.01)	0.83(.40)	1.32(.63)	-
AR131-8	0.85(.03)	1.27(.31)	> 0.95(.40)	-
Mean McMath 12379	0.84(.04)	0.96(.15)	0.98(.16)	-
Move to McMath 12387	0.81(.05)	-	-	-
AR137-9	1.06(.02)	1.39(.24)	0.97(.18)	-
AR137-10	1.09(.01)	0.96(.46)	-	-
AR137-11	1.12(.02)	1.30(.21)	0.85(.24)	-
AR137-12	1.06(.02)	0.99(.14)	0.82(.20)	-
AR137-13	1.07(.01)	1.68(.75)	-	-
AR137-14	1.04(.02)	1.29(.18)	1.06(.13)	-
Mean McMath 12387	1.06(.03)	1.22(.20)	0.96(.20)	-
Aerobee 26.003				
1	-	0.99(.08)	0.80(.07)	1.34(.20)
2	-	0.89(.07)	0.82(.08)	1.02(.16)
3	-	0.68(.06)	0.98(.11)	1.02(.19)
4	-	0.66(.30)	1.24(.20)	-
5	-	1.16(.21)	0.97(.15)	-
6	-	0.89(.08)	0.89(.11)	1.34(.34)
7	-	1.14(.21)	0.70(.06)	1.19(.20)
8	-	1.19(.15)	0.75(.11)	0.99(.33)
9	-	0.73(.06)	1.11(.28)	-
10	-	1.06(.24)	0.86(.14)	-
11	-	0.64(.30)	-	0.96(.29)
Mean McMath 12664	-	0.94(.12)	0.84(.09)	1.14(.20)

TABLE 2

Physical Characteristics Associated with the G Ratio

Region	Effective Temperature	$G_{(eff)}$	Observed G ratios, calculated temperatures and changes in resonance line.					
			150" (FWHM) Field of View			35" (FWHM) Field of View		
			G	T(^{O}K)	ΔR(%)	G	T(^{O}K)	ΔR(%)
Quiet Corona	$1.9\ 10^{6}\ ^{O}K$	0.86	0.63(.07)	6.10^{6}	+37(14)	-	-	-
McMath 12379	$2.\cdot\ 10^{6}\ ^{O}K$	0.76	0.84(.04)	$1.8\ 10^{6}$	-10(4)	0.96(.15)	$<2\ 10^{6}$	-21(11)
McMath 12387	$3.3\ 10^{6}\ ^{O}K$	0.75	1.06(.08)	$< 6\ 10^{5}$	-29(7)	1.22(.20)	$<6\ 10^{5}$	-42(5)
McMath 12664	$3.5\ 10^{6}\ ^{O}K$	0.75	-	-	-	0.94(.12)	$<2\ 10^{6}$	-20(9)

Table 3

Results from Other Measurements of the G Ratio for Various He-Like Ions

Active Region	FOV ("FWHM)	Ion			
		O VII	Ne IX	Mg XI	Source
McMath 11060	240	1.27	0.89	0.93	(b)
McMath 11619	180	0.87(.13)	0.75(.04)	0.77(.16)	(b)
McMath 11621	180	1.13(.05)	0.88(.03)	1.04(.05)	(a)
McMath 12624	180	1.25(.14)	0.95(.01)	0.69(.03)	(a)
McMath 12628	180	0.92(.09)	0.91(.03)	0.83(.04)	(a)
Quiet Corona	169*	1.16	-	-	(c)
McMath 12336	45	1.21(.3)	0.93	-	(d)

* 1-D collimation.

(a) J.Pye, Private Communication.

(b) J. Parkinson; 1972, 1975, Thesis.

(c) McKenzie, et al.: 1977.

(d) Davis et al., 1978.

FIGURE CAPTIONS

Figure 1: Sample O VII Spectra from each of the observed regions. The sum of the forbidden and intersystem lines have been used as a scaling factor in plotting the histograms, hence the resonance lines can be compared directly.

Figure 2a: The coronal model (in the y-z plane) adopted in the calculations. The corona is represented by a isothermal homogeneous tenuous shell of plasma overlaying an opaque sphere of radius, R_1. The source can be placed at an arbitrary position within the shell.

2b: The grid (in the x-y plane) represents the matrix of points at which the emergent flux is computed in any given X-ray emission line.

Figure 3: A comparison of the various components that contribute to emergent flux observed from any position on the sun. The source scatter is calculated as a function of its radial position on the disk. This quantity may be scaled according to the source intensity. The thermal emission from the ambient corona and its corresponding scattered component are also shown without scattering effects.

Figure 4: The combined result of the angular redistribution of the photons with the horizon effects, as a function of altitude in the atmosphere for an elemental volume. The abissa is the angle between the radius vector to the element and the observers line of sight (z axis). The ordinate is the relative scattered intensity weighted by the relative brightness of the radiation field at the element.

Figure 5: The variation of the source scatter, coronal thermal emission, and coronal scatter as a function of the electron density at a point 1 arc minute away from the source. The source is at the apparent disk center, at the base of the corona, and has an intensity of 6.10^{32} phts/cm^2 /sec/st. The resulting change in the G ratio is also shown.

Figure 6: The variation of the source scatter, coronal thermal emission and coronal scatter as a function of the ambient electron temperature of the corona, at a position 1 arc minute away from a source at the apparent disk center. The resulting G ratio is also calculated.

Figure 7: Contour plots of Δ for four different source positions. (a) Source at the apparent disk center. (b) Source region 400 arc seconds from the disk center. (c) Source region 800 arc seconds from disk center (d) Source at the limb. The source is at the base of the corona and at an intensity of $6.0.10^{32}$ phots/cm^2/sec/st. Note the variation of the source Δ as the line of sight column density increases.

Figure 8: By maintaining a constant emission measure, a series of density and height model fit the observed fluxes. The resulting variation of Δ is calculated for a series of models around the adopted value (+).

Figure 9: A comparison of the observed and calculated G ratios for the large field of view (150" FWHM) data as a function of its radial displacement. The unscattered G ratio is assumed to be 0.75.

Figure 10: A comparison of the observed variation in the G ratio with the size of the field of view (FWHM) with (a) the G ratio for different source brightnesses (phts/cm^2/sec) without any scattering, and (b) the G ratio variation for a source brightness of 10^{34} phts/cm^2/sec with scattering effects included.

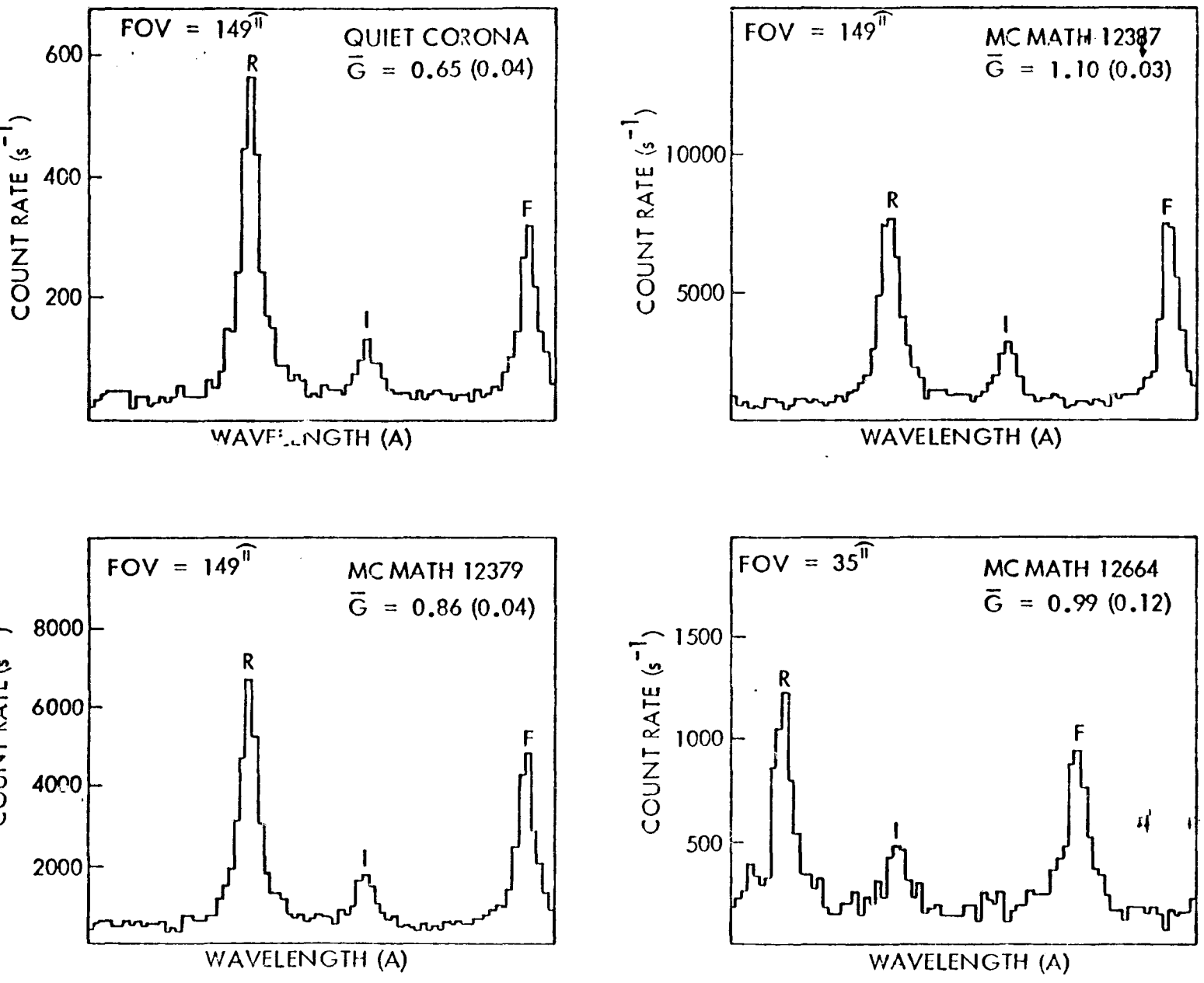
FOV = 149"
QUIET CORONA
$\bar{G}$ = 0.65 (0.04)
R
I
F
600
400
200
COUNT RATE (s^{-1})
WAVELENGTH (A)
FOV = 149"
MC MATH 12387
$\bar{G}$ = 1.10 (0.03)
10000
5000
COUNT RATE (s^{-1})
WAVELENGTH (A)
FOV = 149"
MC MATH 12379
$\bar{G}$ = 0.86 (0.04)
8000
6000
4000
2000
COUNT RATE (s^{-1})
WAVELENGTH (A)
FOV = 35"
MC MATH 12664
$\bar{G}$ = 0.99 (0.12)
1500
1000
500
COUNT RATE (s^{-1})
WAVELENGTH (A)

Figure 1

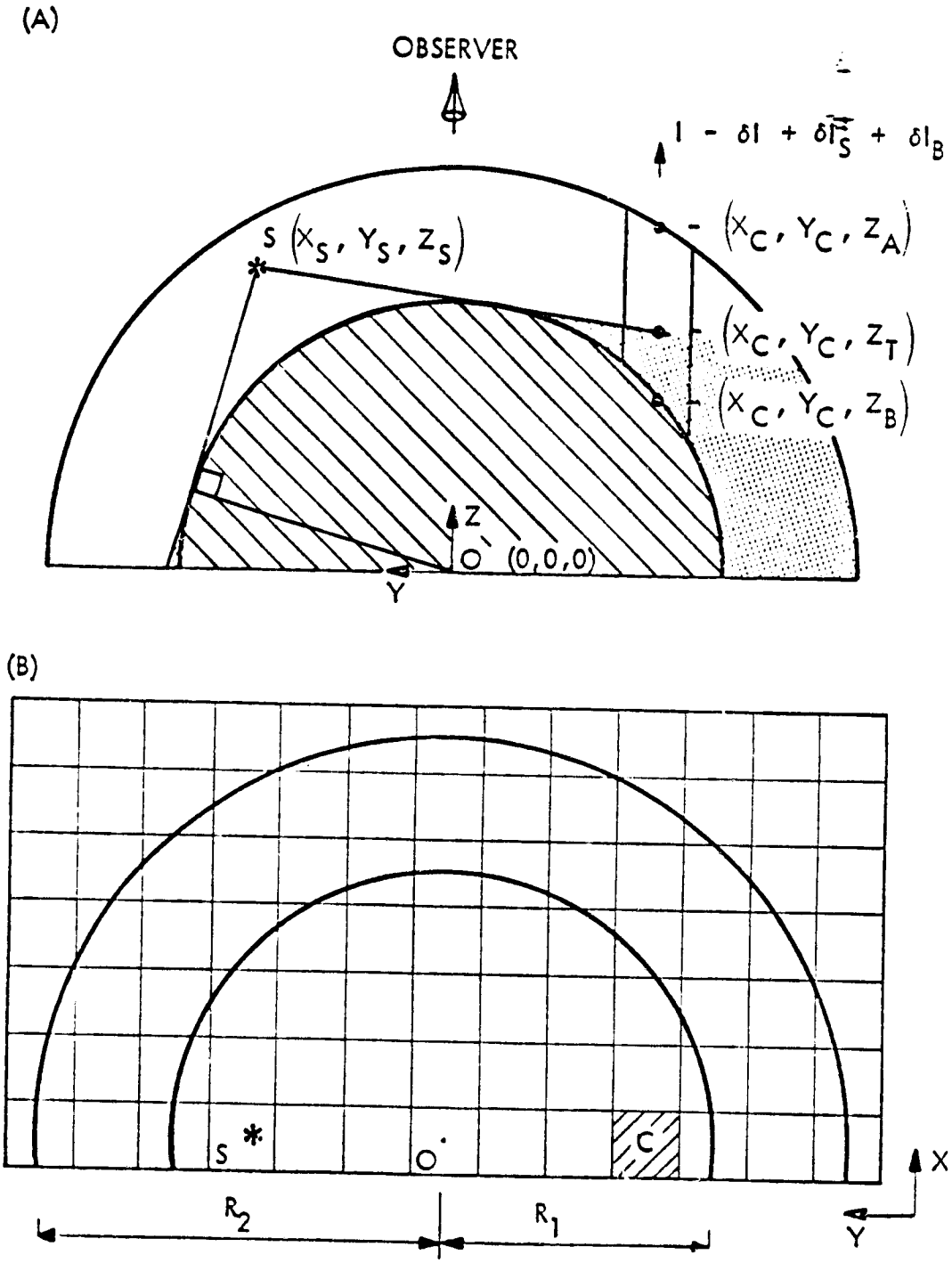
(A)
OBSERVER
$l - \delta l + \delta l_S + \delta l_B$
S (X_S, Y_S, Z_S)
(X_C, Y_C, Z_A)
(X_C, Y_C, Z_T)
(X_C, Y_C, Z_B)
Z
O (0,0,0)
Y
(B)
S
O
C
X
Y
R_2
R_1

Figure 2

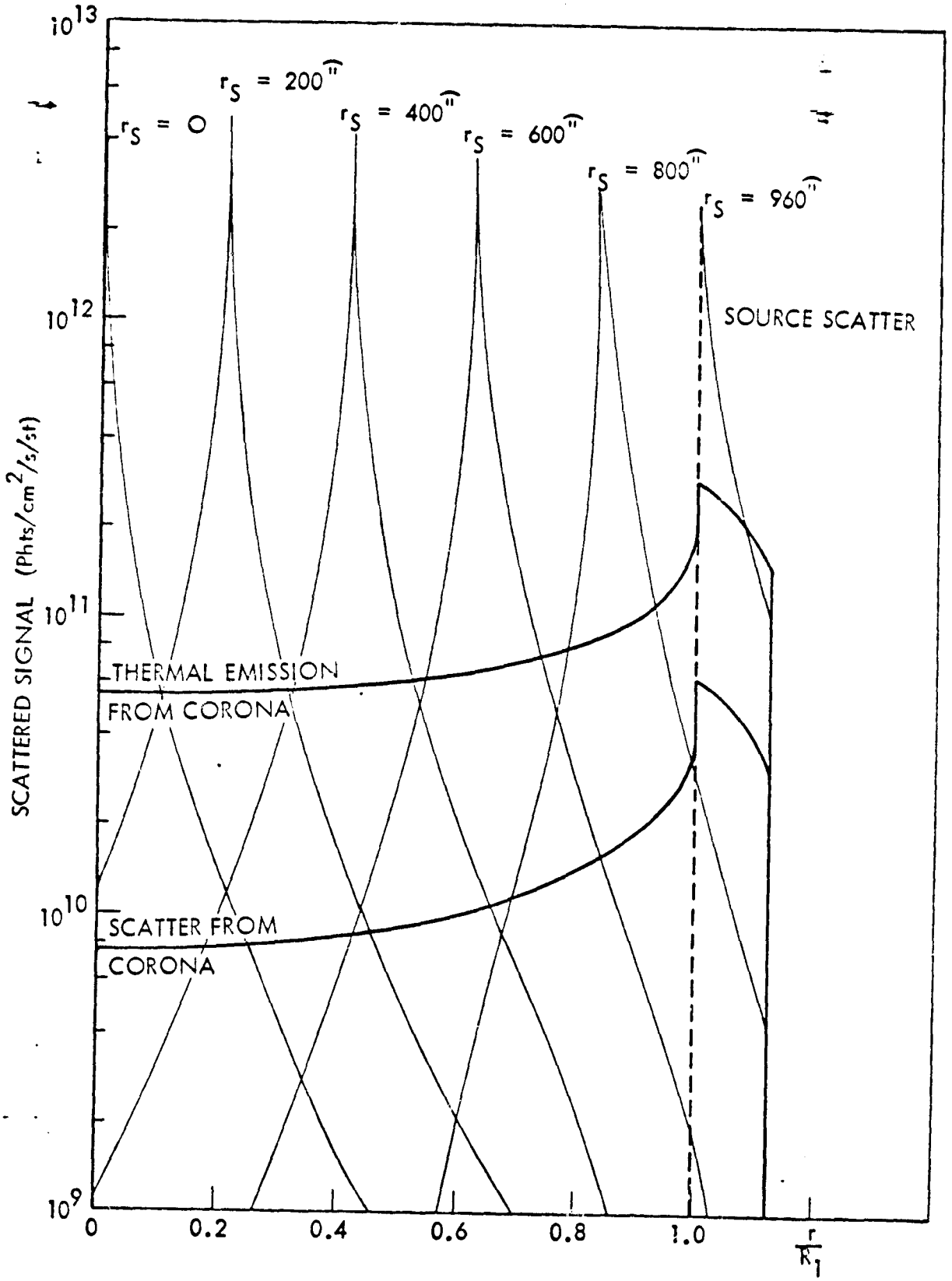
10^{13}
10^{12}
10^{11}
10^{10}
10^{9}
r_S = 0
r_S = 200"
r_S = 400"
r_S = 600"
r_S = 800"
r_S = 960"
SOURCE SCATTER
THERMAL EMISSION
FROM CORONA
SCATTER FROM
CORONA
SCATTERED SIGNAL (Phts/cm^2/s/st)
0
0.2
0.4
0.6
0.8
1.0
$\frac{r}{R_1}$

Figure 3

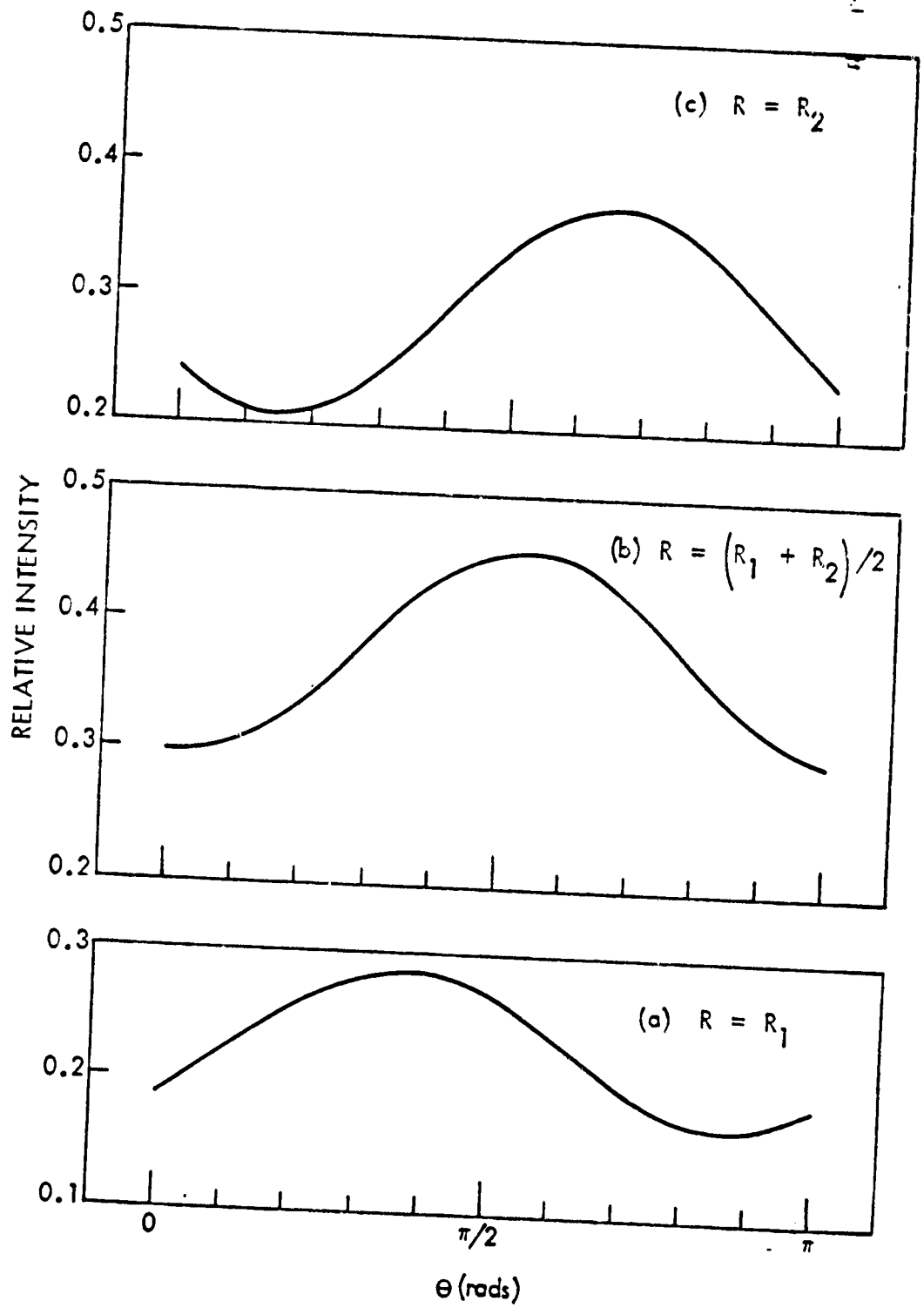
0.5
0.4
0.3
0.2
(c) R = R2
0.5
0.4
0.3
0.2
(b) R = (R1 + R2)/2
RELATIVE INTENSITY
0.3
0.2
0.1
(a) R = R1
0
π/2
π
θ (rads)

Figure 4

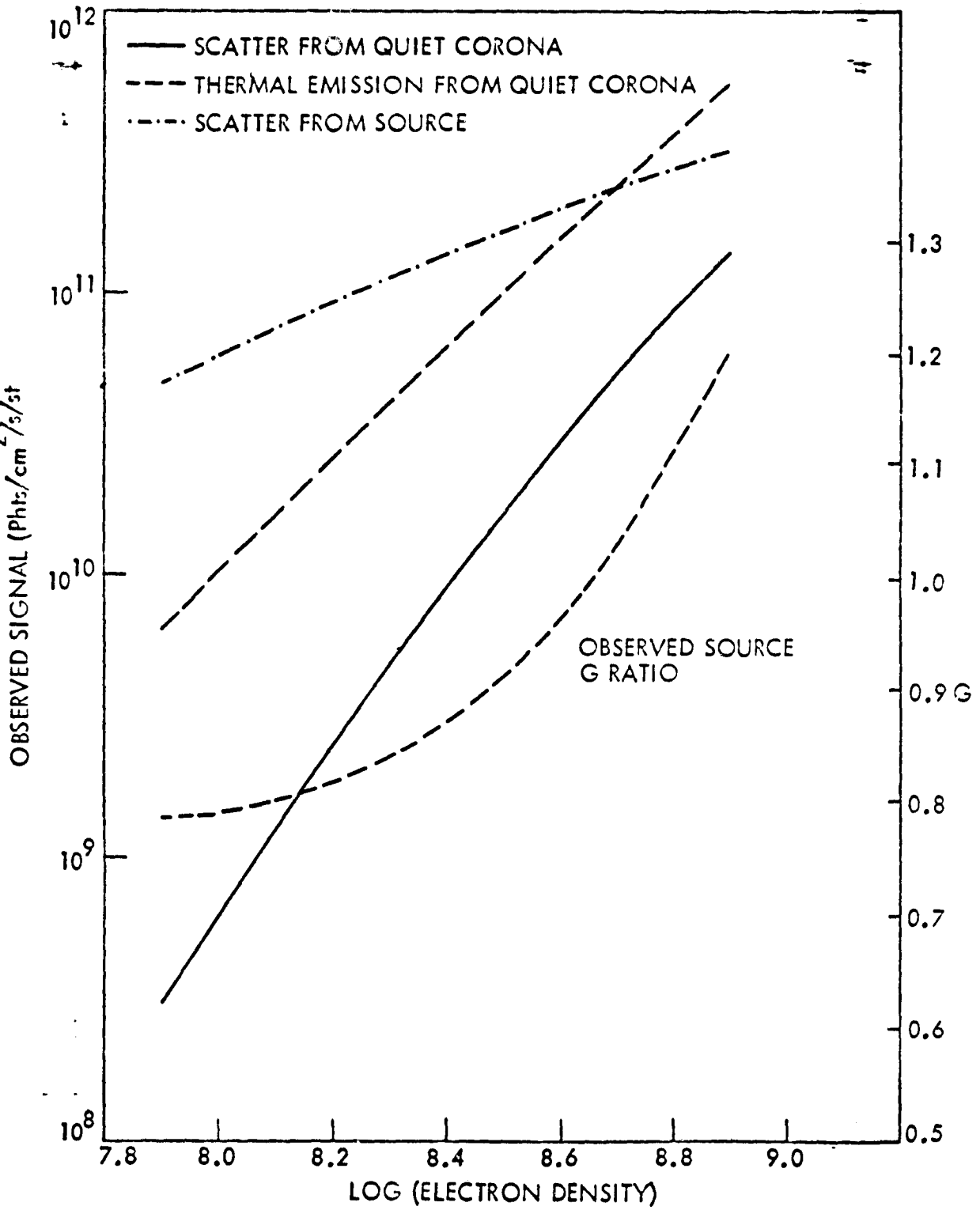
SCATTER FROM QUIET CORONA
THERMAL EMISSION FROM QUIET CORONA
SCATTER FROM SOURCE
OBSERVED SOURCE
G RATIO
OBSERVED SIGNAL (Phts/cm²/s/st)
LOG (ELECTRON DENSITY)
10¹²
10¹¹
10¹⁰
10⁹
10⁸
7.8
8.0
8.2
8.4
8.6
8.8
9.0
1.3
1.2
1.1
1.0
0.9 G
0.8
0.7
0.6
0.5

Figure 5

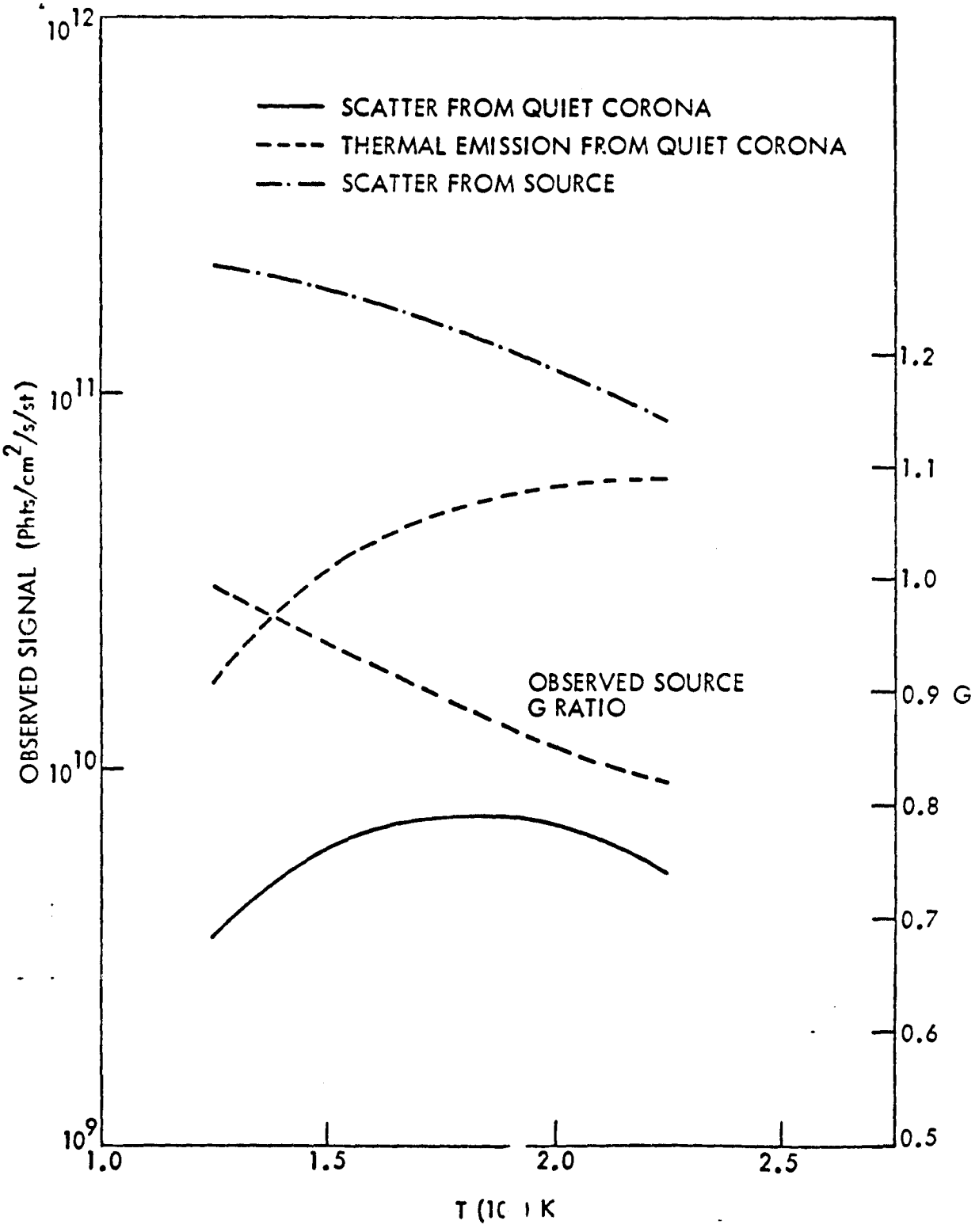
SCATTER FROM QUIET CORONA
THERMAL EMISSION FROM QUIET CORONA
SCATTER FROM SOURCE
OBSERVED SOURCE
G RATIO
OBSERVED SIGNAL (Phts/cm²/s/st)
10¹²
10¹¹
10¹⁰
10⁹
1.2
1.1
1.0
0.9 G
0.8
0.7
0.6
0.5
1.0
1.5
2.0
2.5
T (10⁶ K

Figure 6

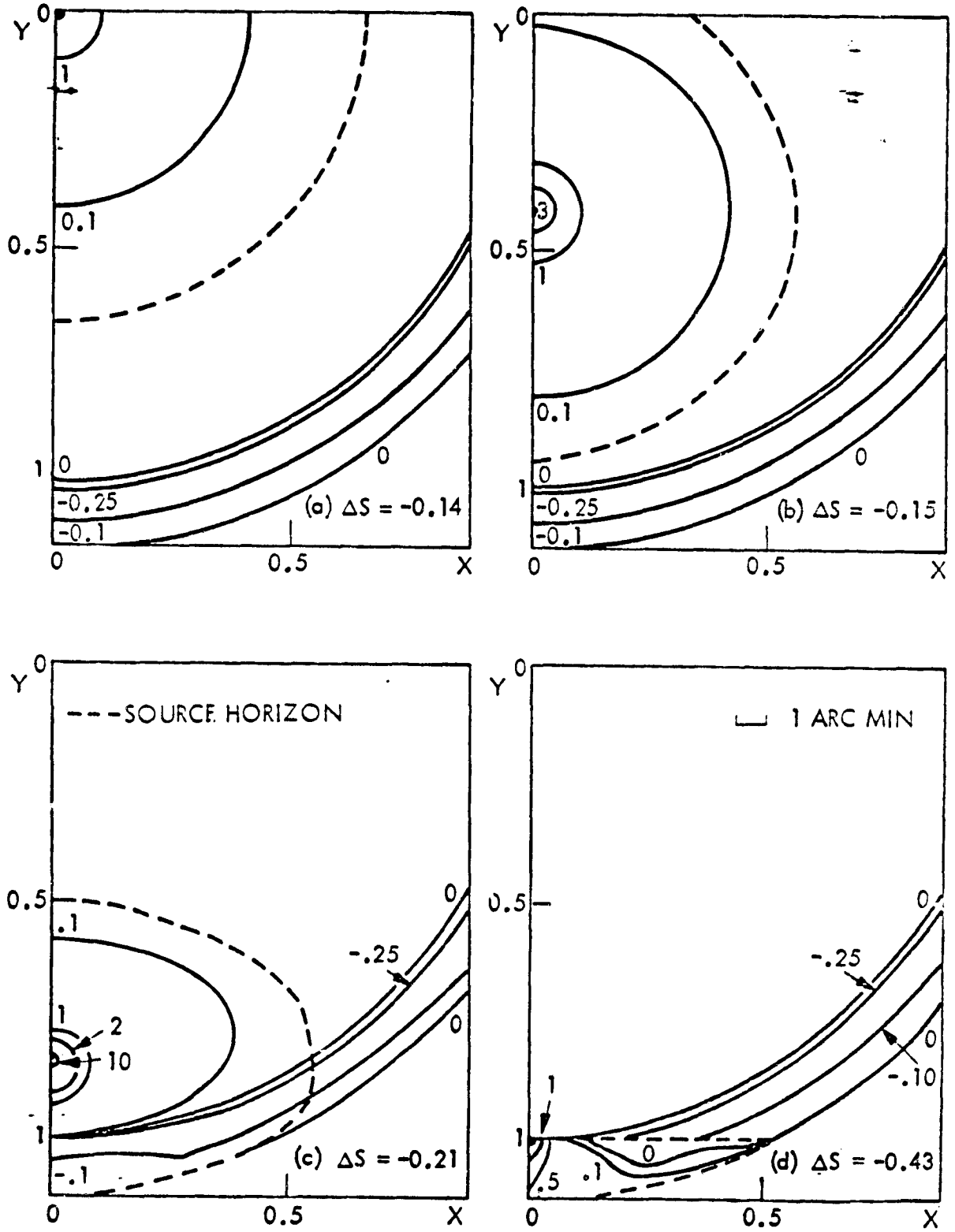
Y
0
1
0.1
0.5
1
0
-0.25
-0.1
0
0.5
X
(a) ΔS = -0.14
3
(b) ΔS = -0.15
SOURCE HORIZON
1 ARC MIN
.1
-.25
2
10
(c) ΔS = -0.21
-.1
.5
-.10
(d) ΔS = -0.43

Figure 7

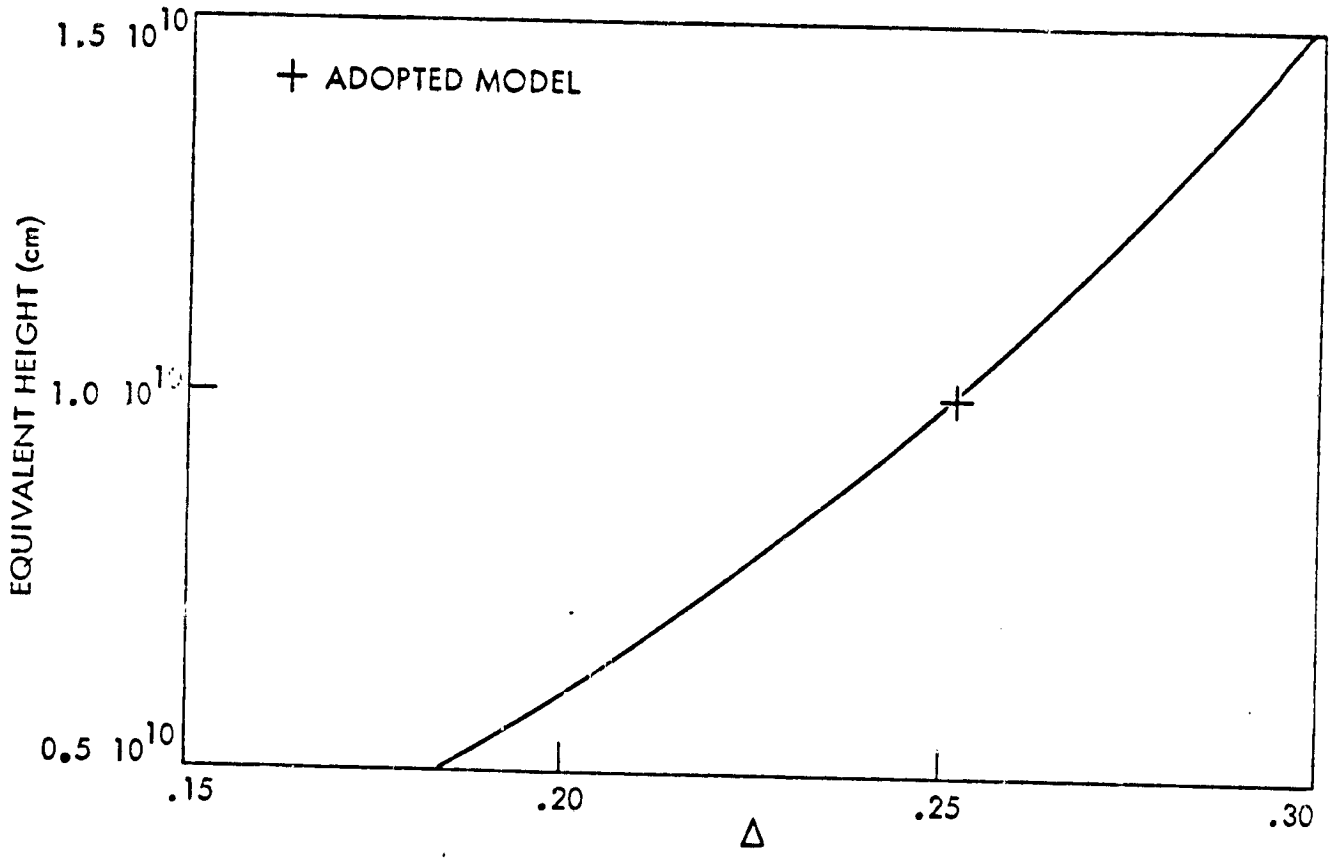
1.5 10^10
+ ADOPTED MODEL
EQUIVALENT HEIGHT (cm)
1.0 10^10
0.5 10^10
.15
.20
.25
.30
Δ

Figure 8

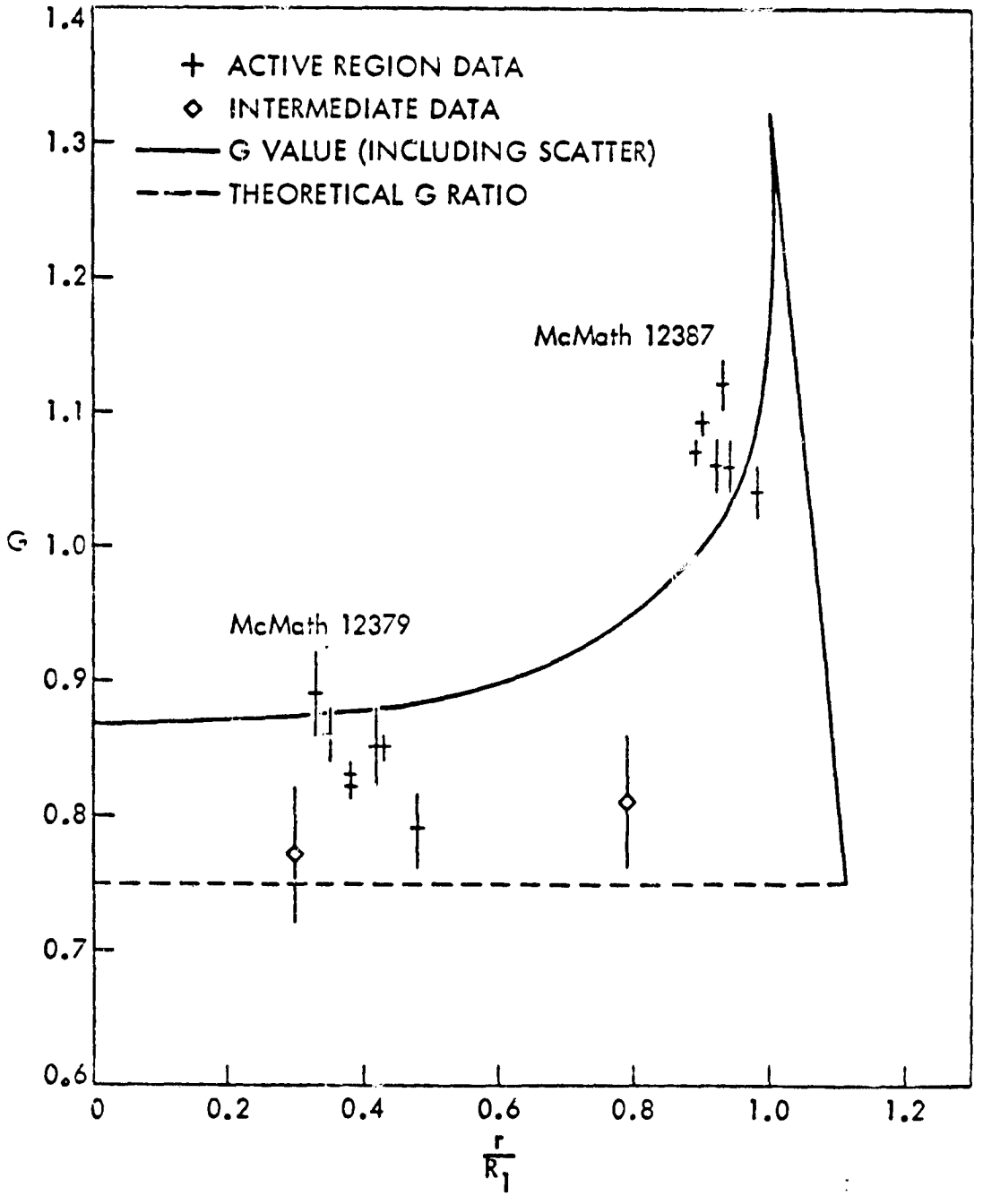
ACTIVE REGION DATA
INTERMEDIATE DATA
G VALUE (INCLUDING SCATTER)
THEORETICAL G RATIO
McMath 12387
McMath 12379
G
1.4
1.3
1.2
1.1
1.0
0.9
0.8
0.7
0.6
0
0.2
0.4
0.6
0.8
1.0
1.2
r/R1

Figure 9

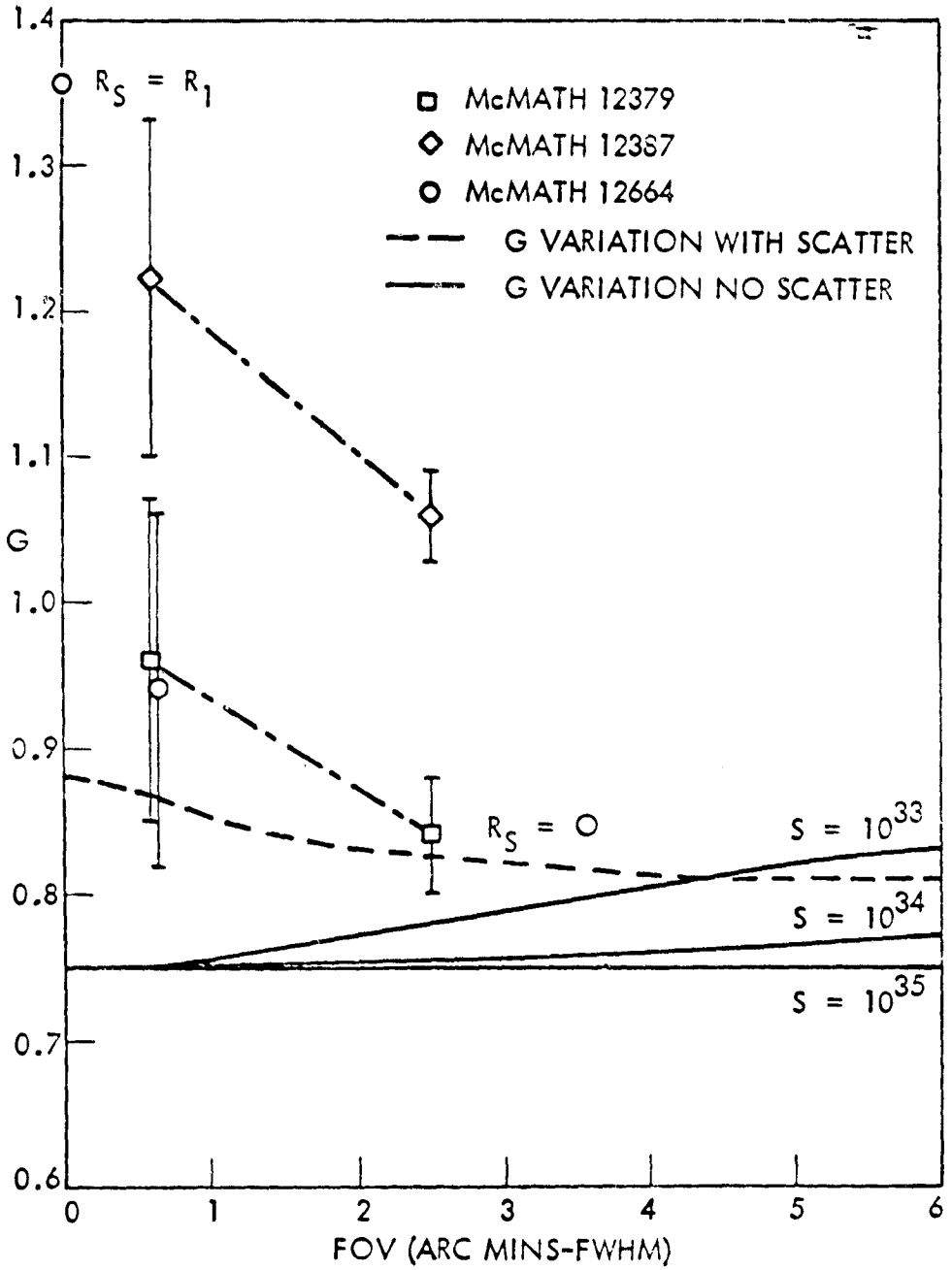
1.4
1.3
1.2
1.1
1.0
0.9
0.8
0.7
0.6
G
0
1
2
3
4
5
6
FOV (ARC MINS-FWHM)
$R_S = R_1$
McMATH 12379
McMATH 12387
McMATH 12664
G VARIATION WITH SCATTER
G VARIATION NO SCATTER
$R_S = O$
$S = 10^{33}$
$S = 10^{34}$
$S = 10^{35}$

Figure 10

Appendix 4

Contents

Summary of computer programs developed during course of this investigation.

by: Keith T. Strong
John L. Kulander

Key: to Program ID code

P : Prediction

D : Data Manipulation

A : Analysis

T : Theoretical Studies

M : Mathematics

1. EMITS - P KTS

Processes any given transition to calculate its temperature and emission functions It also plots the resulting emission function. It can process any number of lines from a line list file between given wavelength limits at one time.

2. CJBAL - D KTS

Ionization Balance data file. Elements:- C, N, O, Ne, Mg, Si, S, Fe (IX - XXVII), Ni (X - XXIX), Ca (IX - XXI).

3. GLEEM - P KTS

Faster version of EMITS (1). Options to plot multiple curves of either the emission or temperature functions. Utilizes Spline routines to smooth plots rather than straight line interpretation of EMITS.

4. CLONE - A + P KTS

Statistical analysis of O VIII : Ne IX line ratios to determine the relative elemental abundance.

5. POINn and POINT - T JK (KTS)

Program to study the radiative transfer of X-rays in the solar corona for various geometries. It calculates the thermal and scattered signal from an elemental column situated in an emitting spherical shell of the dimensions of the corona.

6. SPLYN - M KTS

Interpolation and integration routine utilizing spline techniques.

7. DEMON - P KTS

Predicts line intensities given the transition and wavelength by searching a data file. However, will accomodate differential emission measure models in the range of Log(T) = 5.5 - 7.0.

8. MODEL - A KTS

Takes any set of line intensities and attempts to produce a differential emission measure model using a method described by Withbroe (1975). It also plots the resulting model. The program is interactive so the analysis may be interogated at any point to investigate any problems.

9. LOP1 - P JK

Predicts emission observed from a 3-D loop structure of constant cross-section as seen from any orientation. Development routine for studying resonance scattering of X-ray in a coronal loop.

10. NRLTP - A KTS

Takes NRL digitized images and convolves them with the collimator response of the spectrometers deriving an equivalent intensity in the chosen EUV lines. It takes the film densities on the tape and applies the instrument calibration at any given position in the image.

11. IMAGE - M KTS

Takes any function plotted in 2-D and represent it as 3-D image using Euler angles. Develope routine for X-ray resonance scattering.